# Enabling Tools for Disease Diagnosis, Imaging and Intervention

Junwei Li

A dissertation

submitted in partial fulfillment of the

requirements for the degree of

Doctor of Philosophy

University of Washington

2017

Reading committee:

Xiaohu Gao, Chair

Larry Zweifel

Minqin Zhang

Program Authorized to Offer Degree:

Material science and engineering

University of Washington

**Abstract**

Enabling Tools for Disease Diagnosis, Imaging and Intervention

Junwei Li

Chair of the Supervisory Committee:

Associate Professor Xiaohu Gao

Department of Bioengineering

The ability to create and use tools differentiates humans from all the other living beings. As a result, tools have been playing an important role in human history. Millions of years ago, our ancestors created the very first piece of tools with stone. Since then, many other tools have been created to change our life. In the field of biomedicine, the creation and use of molecular tools, such as molecular probes, nanoscale agents, and drugs, have significantly benefited the modern society. Specifically, these tools have been applied for both the scientific discoveries and clinical advancements. This dissertation elaborates on three molecular tools' applications - disease diagnosis, imaging and intervention - towards the healthcare revolution.

First of all, in terms of disease diagnosis, the ability to detect biomarkers with ultrahigh sensitivity has radically transformed biology and disease diagnosis. However, owing to incompatibilities with infrastructure in current biological and medical laboratories, recent innovations in analytical technology have not received a broad adoption. Here, we have developed a simple yet universal 'add-on' technology (dubbed EASE) that can be directly plugged into the routine practices of current research and clinical laboratories and convert the ordinary sensitivities of common bioassays to the extraordinary level. The

assay relies on the bioconjugation capabilities and ultrafast, localized deposition of polydopamine at the target site, which permits a large number of reporter molecules to be captured and lead to detection-sensitivity enhancements exceeding 3 orders of magnitude. The application of EASE in the enzyme-linked-immunosorbent-assay-based detection of the HIV antigen in blood from patients leads to a sensitivity lower than 3 fg $ml^{-1}$. It is illustrated through experiments that EASE enables the direct visualization of the Zika virus in tissues and of low-abundance biomarkers related to neurological diseases and cancer immunotherapy.

Besides the diagnosis sensitivity, molecular probes allow advanced on-surface assay formats to implement, but impose often underappreciated size-associated constraints, especially on assay kinetics and sensitivity. We evaluated and presented substantially slower diffusion limited assay kinetics due to the rapid development of a nanoprobe depletion layer next to the surface, which static incubation and mixing of bulk solution employed in conventional assay setups often fail to disrupt. In contrast, cyclic solution draining and replenishing yields reaction-limited assay kinetics irrespective of the probe size. Using common surface bioassays, enzyme-linked immunosorbent assays and immunofluorescence, we demonstrate that this conceptually distinct approach effectively “erases” size-dependent diffusion constraints, providing a straightforward route to rapid on-surface bioassays employing bulky probes and procedures involving multiple labeling cycles, such as multicycle single-cell molecular profiling. For proof of-concept, this study demonstrates that the assay time can be shortened from hours to minutes with the same probe concentration and, at a typical incubation time, comparable target labeling can be achieved with around eight times lower nanoprobe concentration. The findings are expected to stimulate realization of novel assay formats and development of rapid on-surface bioassays with nanoparticle probes.

Secondly, in terms of molecular imaging, directly visualizing cellular functions and molecular processes have the potential to transform disease diagnosis, stratify therapy, and aid in drug discovery and validation. Photoacoustic imaging has emerged as a highly promising tool to visualize molecular events with deep tissue penetration. Like many other modalities, however, image contrast under *in vivo* conditions is far from optimal due to background signals from the tissue. Using iron oxide-gold core-shell nanoparticles, we have previously demonstrated the concept of magnetomotive photoacoustic (mmPA) imaging, which is capable of dramatically reducing the influence of background signals and producing

high-contrast molecular images. We achieve two significant advancements on the clinical translation of this technology. On one hand, we introduce a new class of compact, uniform, magneto-optically coupled coreshell nanoparticles that are prepared through localized copolymerization of polypyrrole (PPy) on an iron oxide nanoparticle surface. The resulting iron oxide-PPy nanoparticles feature high colloidal stability and solve the photo-instability and small-scale synthesis problems previously encountered by the gold coating approach. On the other hand, we have developed a new generation of mmPA featuring cyclic magnetic motion and ultrasound speckle tracking (USST), whose imaging capture frame rate is several hundred times faster than the photoacoustic speckle tracking (PAST) method we demonstrated before. These improvements further the robust artifact elimination caused by physiologic motions and validate the application of the mmPA technology for *in vivo* sensitive tumor imaging.

Along with the new nanoprobe design, we also solved the long-standing problem of conducting polymers, the poor resistance to de-doping that directly affects their signature electrical and optical properties. This problem is particularly noteworthy for biomedical uses because of the fast leaching of dopant ions in physiological environments. We develop a new approach to engineer multimodal core−shell nanoparticles with a stably doped conductive polymer shell in biological environments. The stable doping was achieved by making a densely packed polymer brush rather than changing its molecular structure. Polyaniline (PANI) was used as a model compound due to its concentrated near-infrared (NIR) absorption. It was grafted onto a magnetic nanoparticle via a polydopamine intermediate layer. Remarkably, at pH 7 its conductivity is ca. 2000× higher than conventional PANI nanoshells. Similarly, its NIR absorption is enhanced by 2 orders of magnitude, ideal for photothermal imaging and therapy. We also found out its outstanding non-fouling property, surprisingly outperforming polyethylene glycol. This platform technology is also expected to create exciting opportunities in engineering stable conductive materials for electronics, imaging, and sensing.

Also, In contrast to prior efforts to overcome PANI's doping instability issue, we convert its drawback in pH sensitivity to a unique strength to address an important clinical problem. The structural, spectral, and chemical properties of the core–shell nanoparticles were systematically characterized, and a gastric acid secretory testing protocol simulating current clinical practice was developed for live mouse imaging. These nanometer-sized particles are sufficiently large to avoid passive diffusion through the

gastrointestinal mucosa membranes, yet the PANI nanoshell is thin for fast proton diffusion and penetration. Complete nanoparticle elimination after imaging and no systematic toxicity may potentially enable this technology in humans, particularly for elderly and infants, to help reduce the suffering caused by gastrointestinal intubation. We expect this strategy to be readily extended to other pH sensitive polymers and dye molecules (converting a disadvantage into an advantage) for functional stomach imaging.

Last but certainly not least, in terms of disease intervention, over the course of evolution, nature has developed sophisticated biological systems built of networks of cells that form electrical, mechanical, and communication infrastructure with functionality and efficiency often greatly surpassing the most advanced engineered systems. The main objective of this research is to develop a novel physical interface for hijacking the primary actuators of the infrastructure - individual live cells - to enable non-invasive *in vivo* modulation of cellular signaling at currently unattainable levels of spatial and temporal resolution. Fully-developed and -evaluated nanoacoustic technology promises to yield better therapies for diseases, such as cancers, Parkinson's, Alzheimer's and drug resistant hypertension.

## Table of Contents

## List of Figures

## List of Table

## Acknowledgements

I would like to take the opportunity to recognize the excellent education, nearly five-year rigorous research experience, and all my past publications at University of Washington. Because of all the resources I have had, I was able to combine the contents from my published works in a newly-organized format, start my writing in a brand-new perspective and bring this complete work to you.

At the same time, no words can describe how much I appreciate for the following people in my life. My family, specifically my parents and wife, have always been the backbone for me and never stopped supporting me unconditionally since day one. My friends and colleagues who have accompanied me for many years were always there to help me whenever I needed them. All the distinguished scientists whom I have worked with, my supervisors back in undergrad, and lecturers that taught and inspired me have provided me the academic guidance and training that prepared me for this thesis.

A special thank goes to the Gao Lab, specifically my longtime research advisor and mentor, Dr. Xiaohu Gao. When I thought that there was no place for me, a phd student, to achieve my academic goal, Dr. Gao sent me his invitation. Whenever I experienced personal and career difficulties, Dr. Gao always stood out for me. The guidance and support provided by Dr. Gao helped me to not only acquire expertise in the exciting field of biomedical engineering, but also build a solid professional foundation for my academic career in the near future. Many members of the Gao Lab, as a matter of fact, have brought together diverse cultural and research backgrounds to create a friendly collaborative atmosphere that nurtures creativity, collegiality, and perseverance. I would like to extend sincerest gratitude to my lab-mates Pavel, Wanyi, Jing, Weibin, Hongyan, Yueming, and Emily, who relentlessly challenged my opinions, engaged in heated discussions, and offered insightful ideas.

It would not be possible without the prominent cross-disciplinary work, between UW College of Engineering, School of Medicine, Seattle Children Research Institute, and Fred Hutchinson Cancer

Research Center that fosters translational research. Our collaborators, especially Prof. Matt O'Donnel and Prof. Larry Zweifel who are the pioneers in the fields of molecular imaging and neuroscience, have dedicated themselves to maintain clinical utility as a top priority of our technological development efforts. Open exchange of ideas between scientists from diverse research backgrounds provided countless innovative ideas. I am extremely grateful for the University of Washington and affiliated institutions creating such a uniquely inspiring environment for cross-disciplinary research. What's more, my students and mentees have learned the true meaning behind sharing my knowledge and allowed me to think outside the box.

As a scientist, I would not complete my training without engaging in professional development and social service activities. I am truly thankful for my home Department of Material Science & Engineering and Department of Bioengineering providing many outreaching and networking opportunities, facilitating active interaction with the general public, and supporting student organizations.

Last but not least, I would like to acknowledge the sources of funding that supported my training and research. I am grateful for the Howard Hughes Medical Institute (HHMI) for the international student Fellowship. This work was also supported in part by NIH (R21CA192985, R01AI100989, AI083019, AI104002, and AI060389) and the UW Department of Bioengineering.

# CHAPTER 1: INTRODUCTION

## 1.1 *IN VITRO* DISEASE DIAGNOSIS

### 1.1.1 Sensitive biomarker diagnosis as a key driver for biomedical advances

As recent advances in medicine rapidly unravel the genomic and proteomic signatures of disease development, progression, and response to therapy, sensitive and quantitative analysis of disease biomarkers (e.g., DNA, RNA, and proteins) has become increasingly important in the era of precision medicine where diagnostic and therapeutic decisions are tailored towards individual patients. In parallel, to address the challenge in sensitive and multiplexed biomarker analysis, a large variety of exquisitely designed imaging and detection technologies have also been developed in the past decade[1-11]. These enabling technologies often leveraging on the unique properties of colloidal nanostructures (e.g., quantum dots, magnetic nanoparticles, and plasmonic nanoparticles) and precisely engineered sensor devices (e.g., nanowire sensors, cantilevers, and microfluidic channels) are so sensitive that their detection limits are commonly seen in the single-molecule level where low-abundance targets such as circulating oligonucleotides, proteins, viruses, and cells can be enumerated with polymerase chain reaction (PCR)-like sensitivity[12-18]. Despite these remarkable achievements in biotechnology laboratories, broad adoption of these technological innovations by biology and clinical laboratories has been limited, and consequently the impact[19]. The resistance is a result of multiple factors including complex protocols, specialized reagents and equipment, and most importantly the requirement of different infrastructures, a disconnect that not only elevates the upfront cost but also reduces persistent output and cross-laboratory cross-platform consistency.

### 1.1.2 Limitation of diffusion constrains for *in vitro* on surface bioassays

Among all techniques for the biomarker analysis, on-surface bioassays have proven essential for biomedical research, drug discovery, and clinical diagnostics, with a number of enzyme-linked immunosorbent assays (ELISAs), Western blots, DNA microarrays, and cell and tissue staining

procedures (such as immunofluorescence, IF, and immunohistochemistry, IHC) performed on a daily basis. Exciting technological advances have been made toward improving the throughput and multiplexing capacity of these methods[20]. In particular, novel nanoparticle-based probes are being developed for exploiting previously unattainable functionalities to address continuously expanding demands of new research and clinical applications[1]. For example, surface-enhanced Raman scattering nanoparticle probes now offer a highly sensitive tool for biomolecular detection and imaging[21-23], fluorescent nanoparticles enable multiplexed molecular imaging via conventional fluorescence microscopy,[24-29] and recently introduced polymeric rare earth metal-containing bioconjugates promise an unprecedented level of multiplexing via mass-spectrometry imaging techniques[29, 30]. However, majority of on-surface assays face the same fundamental limitation in assay kinetics and sensitivity due to slow probe diffusion from the bulk solution to surface-immobilized targets. Remaining largely underappreciated, size-associated diffusion constraints might substantially diminish or completely obliterate the added functionality expected from the incorporation of nanoparticle probes in bioassays.

## 1.2 *IN VIVO* MOLECULAR IMAGING

### 1.2.1 Limitation of *in vivo* bio-imaging

Besides of *in vitro* biomarker analysis, *in vivo* bio-imaging is also one of the most important elements of disease detection and staging. Deadly diseases such as metastatic cancer are difficult to cure. For many types of cancer, however, the chances of treating them effectively are actually very good if precancerous lesions or the primary tumors, before they metastasize, can be detected early[31]. Along with biomarker screening, advanced molecular imaging techniques can potentially allow direct visualization of cellular functions and molecular processes in small lesions, thus guiding the accurate disease diagnosis. Unfortunately, current imaging modalities suffer both poor sensitivity and specificity under *in vivo* conditions. On the biology side, biomarkers with high specificity to diseased cells are urgently needed, whereas on the imaging side, approaches to improve contrast remain a major challenge. Regardless of the modality, a common problem for non-invasive imaging is the strong background signals from tissue. For example, in optical imaging, photon absorption, scattering, and auto-fluorescence obscure specific signals from targeted contrast agents.

Typically, optics-based molecular imaging conjugates a targeting ligand (e.g., antibodies, peptides, aptamers, and small-molecule antagonists) with fluorescent dye molecules to interrogate a particular disease biomarker or pathway in lab animals and potentially human beings. However, conventional organic dye molecules are neither bright nor photo-stable particularly in the near infrared (NIR) spectrum, considered to be a 'clear window' for *in vivo* imaging due to improved light penetration depth and reduced tissue autofluorescence background[32].

To go beyond the intrinsic limitations of small-molecule dyes, a variety of new exogenous imaging probes have been developed recently. The most prominent includes semiconductor quantum dots (QDs) and conjugated polymers (CPs)[33-36]. Compared to small-molecule organic dyes, QDs are superior in many spectrum aspects, such as brightness, photostability, emission color tunability, Stokes shift, and absorption and emission profiles. At this time, however, high-quality quantum dots are mainly made with toxic chemical elements and thus their long-*term in vivo* toxicity is a major concern[37, 38]. Their potential

toxicity prevents them from clinical translation especially as a screening tool where periodic injections are expected. In this regard, CPs with high brightness, resistance against photobleaching, and benign biochemical properties have become a highly promising alternative for high-sensitivity and high-specificity imaging with translational potential. Also, virtually all current uses of CPs in fluorescence *in vivo* imaging are for superficial targets (subcutaneous lymph nodes and tumors). This is understandable because even in the NIR spectral region, light penetration is largely limited to the millimeter range. One approach to mitigate this problem is to engineer CPs with strong NIR absorption and emission because fluorescence uses light that must travel both in and out of tissues. However, the limited light penetration depth due to strong photon absorption and scattering by biological tissues is an inherent issue for optical imaging and cannot be completely eliminated.

An alternative method to improve imaging depth is photoacoustics (PA), utilizing heat (non-irradiative) dissipated by PA contrast agents, because even for a fluorophore with high fluorescence quantum yield, a substantial percentage of energy from the absorbed excitation photon is released in the form of heat. In addition, materials design and chemistry provides additional opportunities to fine tune both radiative and non-radiative decay within a molecule[39]. PA imaging combines optical interrogation of a target by pulsed laser irradiation with ultrasound detection of the resulting thermally-induced acoustic waves (light travels one way and sound travels one way). The integration of high optical contrast enhanced by the specific optical absorption of contrast agents with the spatial resolution of ultrasound detection deep within tissue has made PA imaging a promising tool for molecular imaging. Currently, most exogenous contrast agents for PA imaging are based on inorganic nanoparticles and small-molecule NIR dyes. We believe some CPs can offer unique advantages for this relatively new imaging mode because of their large absorptivity and outstanding photostability, unusual features for organic materials that have been repeatedly reported but largely underutilized so far. These properties are critically important for PA imaging, and can become a highly active research direction.

Even though PA imaging has emerged as a highly promising tool to visualize molecular events with deep tissue penetration. Like most other modalities, however, image contrast under *in vivo* conditions is far from optimal due to background signals from tissue. Using iron oxide-gold core-shell nanoparticles, we

have previously demonstrated the concept of magnetomotive photoacoustic (mmPA) imaging, which is capable of dramatically reducing the influence of background signals and producing high-contrast molecular images[40]. However, in terms of clinical translation, this nanoparticle synthesis is hard to scale up. Also, the gold shell nanoparticles can not stand long time laser irradiation during the imaging process. In this regard, conjugated/ conducting polymers (CPs) with high brightness, resistance against photobleaching, and benign biochemical properties have become a highly promising alternative for high-sensitivity and high-specificity imaging with translational potential. CPs are macromolecules with π-conjugated backbones. Due to their unique electric conductivity and photoluminescence, they have proven useful in a number of research fields, such as sensors, light emitting devices, imaging probes, as well as drug delivery vehicles[41-51]. Common CPs include polyfluorene (PF), poly(fluorenyldivinylene) (PFV), poly(phenylene ethynylene) (PPE), poly(p-phenylenevinylene) (PPV) and derivatives. These CPs, however, cannot be directly used for biomedical applications due to their poor solubility in water. A natural solution is to add pendant groups onto the polymer backbone, thus converting CPs into conjugated polyelectrolytes (CPEs)[52, 53]. Alternatively, CPs can be made into nanoparticles stabilized with amphiphilic surfactants or block copolymers[54, 55]. Indeed, a majority of the *in vivo* applications of CPs reported so far are designed around CP nanoparticles, due to the flexibility in CP selection, simple synthetic protocols, excellent size range for tissue penetration and plasma circulation, high photostability, inert biochemical behaviors, and easiness of doping or mixing CPs.

### 1.2.2 Limitation of conducting polymers for molecular imaging

Conducting polymers such as polyaniline and polypyrrole (PPY) have captivated scientists for decades due to low cost, lightweight, dispersibility, and more importantly their fascinating electrical, mechanical, and optical properties[56-58]. These properties have enabled a broad spectrum of applications such as optoelectronics, flexible circuits, catalysis, and smart fabrics[59-64]. Most recently, conducting polymers have emerged as an attractive material for biosensing and a better alternative to metal nanoparticles for photothermal imaging and therapy due to their improved photostability over metallic nanoparticles[65, 66]. Regardless of the applications, however, a long-standing intrinsic problem of conducting polymers is their

poor resistance to dedoping. Current conducting polymers must be doped (often by oxidation, adding dopants to remove some delocalized electrons) to maintain their signature electrical and optical properties, but these dopants are not permanently "integrated" into the polymer backbone, thus susceptible to dissociation.

Using polyaniline (PANI) as an example, it is one of the first conducting polymers discovered and arguably the most popular one for bioapplications (e.g., photothermal therapy and photoacoustic imaging due to its concentrated near-infrared (NIR) absorption[67-69]. The imaging contrast and heating efficiency, however, are far below expectation due to the dedoping issue in physiologic environment. PANI has two protonation states, emeraldine salt and emeraldine base, that are reversible through protonation (oxidization) and deprotonation (reduction). The two protonation states show very different electro-optical properties. In acidic environment, protonated emeraldine salt is highly conductive and has a strong NIR absorption peak (visually appears green due to strong absorption in the blue and red), whereas in neutral or basic environment, the deprotonated emeraldine base is nonconductive and has extremely low NIR absorption (appears blue). Prior attempts to solve the problem have been focused on chemical modification of aniline's molecular structure (e.g., by covalently integrating negatively charged functional groups) to make its derivatives self-doped. These derivatives indeed show electroactivity in extended pH range, but at the cost of significantly reduced conductivity and absorption (orders of magnitude lower)[70-72].

### 1.2.3 Functional molecular imaging

Gastrointestinal disorders affect approximately 70 million individuals and cause more than 236 000 deaths annually in the United States alone[73]. Gastric acid secretion is a critical function in digestion and assimilation, and gastric acid secretory disability is involved in many gastrointestinal diseases, such as Zollinger–Ellison Syndrome, pernicious anemia, chronic gastritis, atrophic gastritis, and gastric carcinoma [74]. Therefore, real-time monitoring of pH in the stomach can offer major benefits in both diagnosis and treatment of these diseases. Unfortunately, functional imaging of the stomach and measuring real-time gastric acid secretory ability are difficult due to the lack of a simple, accurate, and noninvasive approach[75]. Currently, a number of direct and indirect pH measurement strategies exist, with

gastrointestinal intubation (insert a plastic tube through the nose or mouth down into the stomach) and radio telemetry capsule (patients swallow a pH-sensing capsule) being the most popular for continuous direct assessment of gastric pH conditions[76]. However, these tests suffer from complications, poor patient tolerance, and in particular inappropriateness for infant patients (e.g., hyperacidity, achlorhydria, and gastroesophageal refluxdisease (GERD)). Therefore, innovations in safe and noninvasive imaging technologies enabling functional imaging of the stomach are urgently needed for accurate diagnosis and effective treatment of gastrointestinal diseases. Photoacoustic imaging has the potential to address this problem because it is a nonionizing, noninvasive, and low-cost imaging modality, combining the rich chemistry and spectral tunability of optical contrast agents, and the spatial resolution of ultrasound detection deep within tissue[77]. Indeed, PA-based imaging and detection have been demonstrated in various disease models, including intestinal diseases[78]. During PA imaging, light-absorbing dye molecules, polymers, or nanoparticles (mostly absorbing in the near-infrared (NIR) region to maximize light penetration depth and heat generation) are often used to provide image contrast. For example, based on PA imaging, small-molecule organic dyes such as indocyanine green have been utilized for tumor imaging and diagnosis, whereas inorganic nanoparticles such as Au nanorods and nanoshells are commonly used in tumor and vasculature imaging. Similarly, conductive polymers have been proposed as a better alternative because of their excellent absorption property similar to Au nanostructures and their improved photostability over metallic nanostructure counterparts[65, 66, 79] [80–82].

## 1.3 *IN VIVO* CELL STIMULATION

### 1.3.1 Modulation of cellular signaling for disease intervention

Untangling the intricacies of biological systems holds a key to comprehension of the fundamentals of life, achieving command over health and disease, and gaining insight into design of novel bio-inspired artificial systems. Yet, biological systems elude our complete understanding and control, in part due to lack of means for interaction with individual cells within complex cellular networks. For example, optogenetics is capable of controlling cell signaling via precise activation of genetically-modified photosensitive ion channels with light[80-84], but its translation is hampered by shallow depth of light penetration into tissues and the requirement for gene transfection. Similarly, microelectrodes have been successfully used for stimulation of voltage-gated ion channels[85], but proven exceedingly invasive for *in vivo* use. Therefore, we posed a question - would it be possible to achieve similar level of cell stimulation precision with a non-invasive remotely activated artificial interface, while overcoming the above-stated limitations? And, more intriguingly, would a newly-established hybrid biological-artificial system exhibit augmented functionality, replacing a pre-existing system with deteriorated or sub-optimal performance?

# CHAPTER 2: *IN VITRO* TOOLS FOR DISEASE DIGANOSIS

## 2.1 DRAMATIC ENHANCEMENT OF THE DETECTION LIMITS OF BIOASSAYS VIA ULTRAFAST DEPOSSITION OF POLYDOPAMINE

Here we present a universal 'add-on' technology that can be plugged into virtually all common biodetection and bioimaging techniques, and enhance their sensitivities by approximately three orders of magnitude. This enhancement is achieved by combining horseradish peroxidase (HRP), one of the most popular reporter enzymes in biology, with polydopamine (PDA), arguably the most versatile coating material in surface treatment. Previously, a simple dip-coating protocol has been demonstrated for spontaneous formation of a thin self-adherent PDA film onto a wide range of surfaces[86]. Interestingly, we found that when dopamine is used in place of the typical HRP substrates, its polymerization rate is increased by 100s of times. In addition, PDA is well known for its outstanding reactivity to the amine, sulfhydryl, and phenol groups in proteins[87], enabling site-specific deposition in the vicinity of HRP and the subsequent sensitive detection based on absorption or fluorescence (**Fig. 2.1.1a**). It is worth mentioning that although we discovered the remarkable performance of HRP-PDA combination in biotechnology, similar mechanism has been utilized in nature for perhaps thousands of years. For example, it has been found that invertebrates take advantage of oxidase-catalyzed rapid melanin deposition to treat mechanical injuries and isolate foreign organisms such as parasites[88, 89]. The chemical reaction is very similar to HRP-catalyzed PDA deposition.

### 2.1.1 Enzyme-accelerated ultrafast PDA deposition

To quantify the effect of HRP on PDA polymerization rate, the enzyme-accelerated signal enhancement (EASE) process is compared to the reaction conditions in the conventional dip-coating polymerization procedure where HRP is not present and $O_2$ is the oxidant.

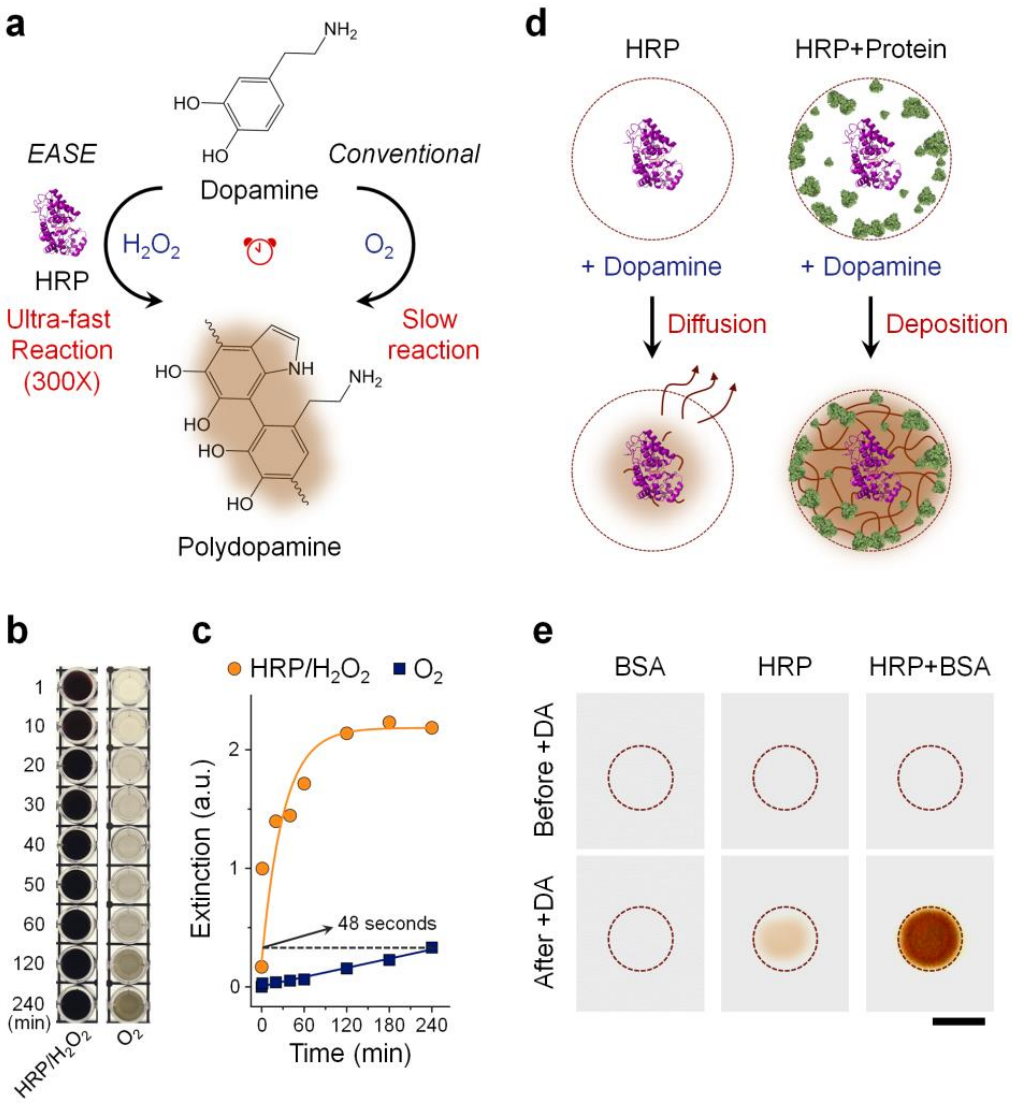


**Figure 2.1.1 HRP-accelerated dopamine polymerization and deposition.** (**a**) Schematic illustration of the EASE technology. Dopamine (colorless) slowly oxidizes in the presence of air ($O_2$ as oxidant) and produces brown-black PDA. This polymerization process can be sped up by approximately 300 times under HRP catalysis ($H_2O_2$ as oxidant). (**b**) Visual observation of dopamine polymerization under conventional and HRP catalyzed conditions at various time points. (**c**) Extinction measured at 700 nm for the samples showing in (**b**). EASE produces the same optical extinction (700 nm) in 48 s compared to 4 h under conventional conditions. (**d**) HRP-catalyzed PDA deposition on solid supports. When protein density on the solid support is low (for example only HRP is present), majority of the PDA molecules diffuse away. For solid supports (*e.g.*, flat surface and membrane) with high protein density (*e.g.*, in cells and surfaces blocked with protein molecules for reduced nonspecific binding), rapid and localized deposition of PDA occurs due to the reactivity of PDA to nearby amines (rich in proteins), leading to formation of a dark spot. (**e**) Images showing membranes immobilized with BSA alone, HRP alone, or HRP/BSA before and after exposing to dopamine. Scale bar, 5 mm.

As shown in **Figure 2.1.1b**, the dopamine solution slowly changes color from colorless to light grey over a period of four hours, indicating slow PDA formation. In contrast, when HRP and $H_2O_2$ of low concentration (typical reaction condition for HRP-catalyzed substrate conversion) were added, the dopamine solution of the same concentration instantly turns to brown-black, showing significantly increased PDA polymerization rate. Quantitative comparison of the reaction kinetics was plotted by measuring the solution light extinction at 700 nm where dopamine has negligible absorption compared to PDA (**Fig. 2.1.2**). Under the dip-coating reaction condition, PDA slowly builds up and is not near completion after 4 h of reaction time; whereas under the EASE condition, the PDA solution reaches the same level of light extinction in 48 seconds (plateaus within 1 h), indicating an approximately 300-fold increase in polymerization rate (**Fig. 2.1.1c**).

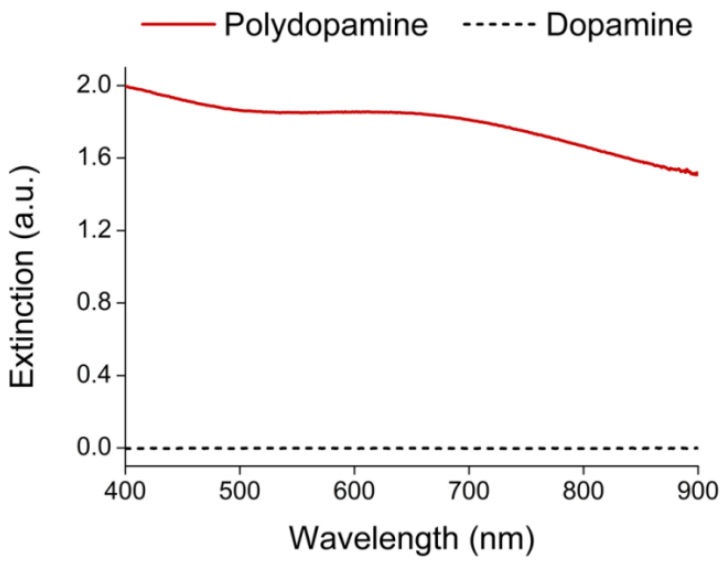


**Figure 2.1.2 Normalized extinction spectra of polydopamine and dopamine.**

Next, we characterized whether the EASE process can be confined to the vicinity of HRP molecules (**Fig. 2.1.1d**), a key factor determining the scope of downstream applications. If PDA molecules quickly diffuse away from HRP, the EASE technology will only be useful for improving the enzyme-linked immunosorbent assay (ELISA) by measuring chromogens in solution. If the PDA molecules are confined near HRP, the EASE technology will be broadly applicable to various bioassays beyond ELISA, such as

immunohistochemistry (IHC), immunofluorescence (IF), fluorescence in situ hybridization (FISH), and immunoblotting, because the spatial information is preserved. To probe it, HRP was immobilized inside a circle on a nitrocellulose membrane, which was also blocked with bovine serum albumin (BSA). Note that BSA, as a standard blocking agent that helps reduce non-specific binding, serves an additional function here. It also provides reactive chemical groups as the PDA deposition anchor sites. As shown in **Figure 2.1.1e**, when the membrane was exposed to dopamine/$H_2O_2$ solution, essentially no PDA was found on the membrane with BSA only (free of background). In contrast, when HRP is present on the membrane, PDA development becomes clearly visible because HRP not only catalyzes the PDA polymerization, but also, as a natural protein molecule, serves as the PDA deposition anchor point. For the membrane incubated with HRP and blocked with BSA, PDA deposition is significantly enhanced due to the high-density reactive sites on the membrane (provided by the BSA molecules) that quickly capture PDA molecules before they diffuse away from the surface. More importantly, the color development is completely confined inside the HRP spot, demonstrating retention of the spatial resolution that makes EASE suited for the aforementioned immuno and hybridization assays.

## 2.1.2 EASE for immunohistochemistry and immunofluorescence

The EASE technology was first applied to IHC and IF, robust technologies capable of interrogating gene expressions in single cells and resolving the heterogeneity issues of complex tissue samples, with well-preserved cell and tissue morphology. IHC and IF work well for high-abundance target molecules, but lacks the sensitivity to detect antigens of low abundance[90, 91].

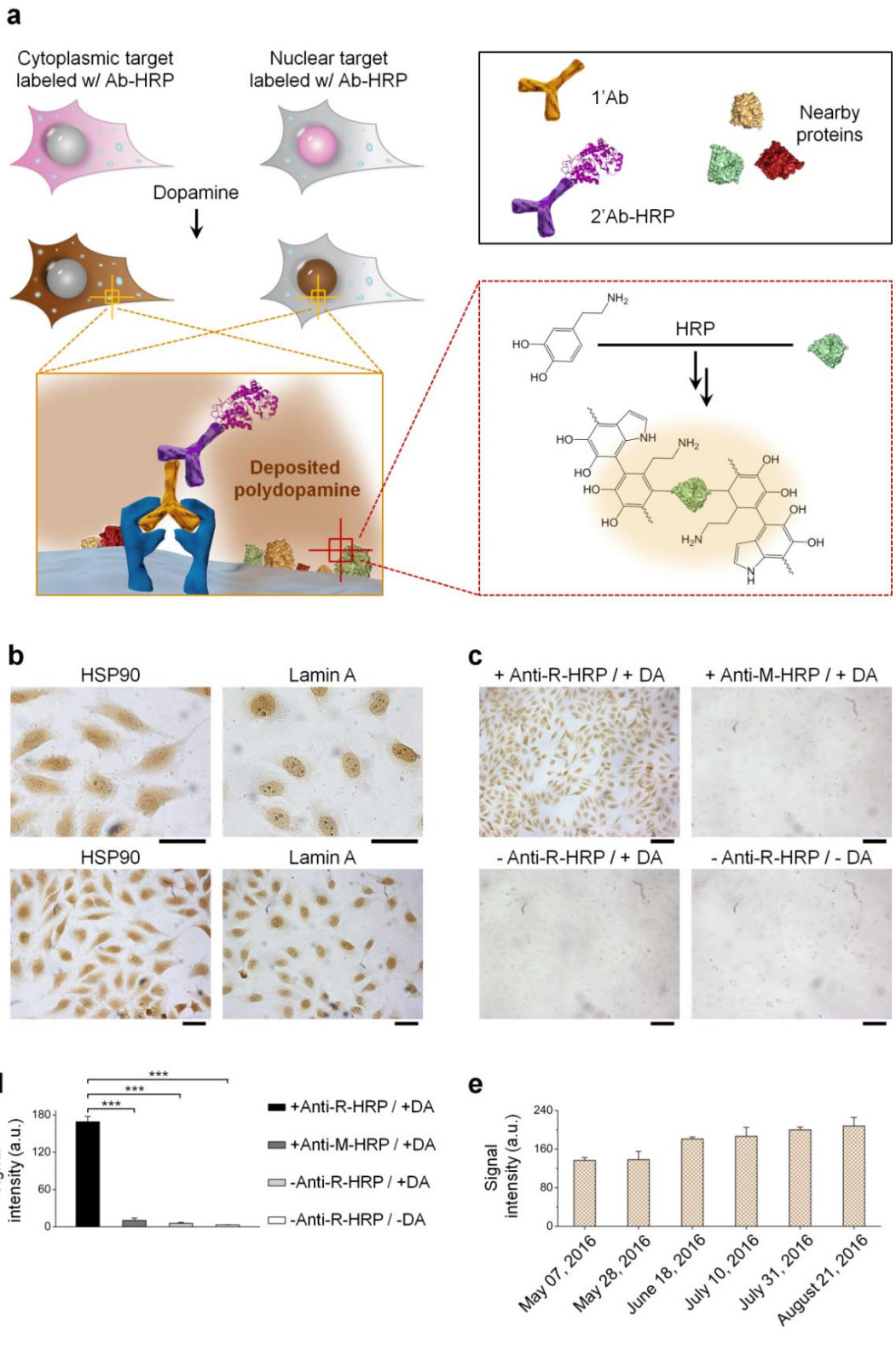
a
Cytoplasmic target labeled w/ Ab-HRP
Nuclear target labeled w/ Ab-HRP
Dopamine
1'Ab
Nearby proteins
2'Ab-HRP
Deposited polydopamine
HRP
b
HSP90
Lamin A
HSP90
Lamin A
c
+ Anti-R-HRP / + DA
+ Anti-M-HRP / + DA
- Anti-R-HRP / + DA
- Anti-R-HRP / - DA
d
Signal intensity (a.u.)
+Anti-R-HRP / +DA
+Anti-M-HRP / +DA
-Anti-R-HRP / +DA
-Anti-R-HRP / -DA
e
Signal intensity (a.u.)
May 07, 2016
May 28, 2016
June 18, 2016
July 10, 2016
July 31, 2016
August 21, 2016

**Figure 2.1.3. IHC-EASE single-cell staining.** (**a**) Schematic illustration of IHC-EASE. Cells are labeled with 1'Ab and 2'Ab-HRP complex sequentially, and exposed to dopamine. Localized PDA deposition (dark brown) indicates the spatial and abundance information of the target. (**b**) Bright-field imaging of IHC-EASE stained cells with different magnifications showing cytoplasmic and nuclear staining of HSP90 and Lamin A, respectively. Scale bar, 50 μm. (**c**) Bright-field imaging of HSP90 staining showing the specificity of IHC-EASE compared to negative controls. Mismatched anti-mouse (M)-HRP, absence of 2'Ab-HRP or dopamine produces negligible signals. Scale bar, 100 μm. (**d**) Quantitative measurements of the staining intensities of samples shown in (**c**). Statistical analysis of cells in four random field-of-views shows significant differences between the experiment and control groups. ***$P$ < 0.001 by two-tailed $t$-test, error bars indicating s.d. (**e**) Quantitative evaluation of the staining stability upon storage. The staining signal does not decay over a period of three and half months. In fact, the signal slightly increases, likely due to aging of the rapid-formed PDA. Error bars, s.d. over four different images.

To test the suitability of EASE, two model antigens, Lamin A (nuclear envelope) and HSP-90 (cytoplasm) were stained in formalin-fixed HeLa cells because these two antigens represent targets in different cell compartments (**Fig. 2.1.3a**). Conventional two-step staining procedure was carried out by incubating cells with the primary antibody (1'Ab) and secondary antibody-HRP (2'Ab-HRP) sequentially, except that dopamine was used as the HRP substrate. Owing to the chromogenic feature of PDA, the staining can be directly visualized. As shown in **Figure 2.1.3b**, the staining patterns for both antigens are the same as those obtained with conventional IHC and IF, demonstrating the staining specificity and confirming the confined PDA deposition on the microscopic scale. The specificity is further confirmed by a series of control experiments where either one of the key agents (1'Ab and 2'Ab-HRP) is missing or a mismatched 1'Ab-2'Ab pair is used (**Fig. 2.1.3c, d**). It is also worth mentioning that the PDA chromogens are highly stable after cell staining. As shown in the same group of cells in **Figure 2.1.3e** and **Figure 2.1.4**, no obvious signal decay was detected after 4-month, allowing samples to be reexamined after long storage.

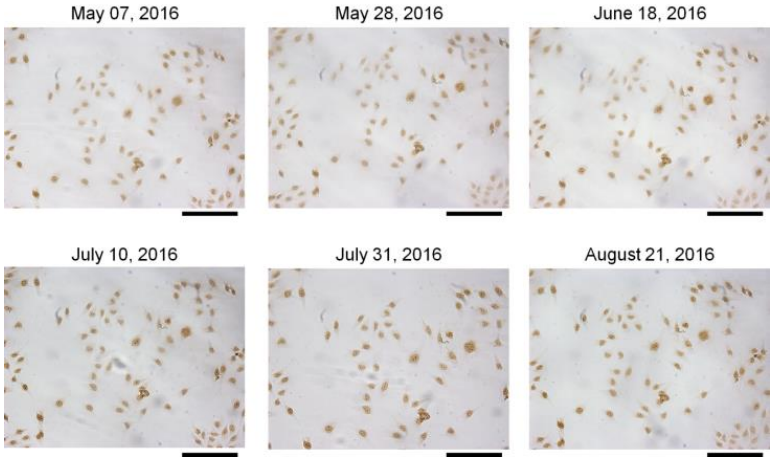

**Figure 2.1.4. IHC-EASE staining stability after storage.** Bright field images of the same group of cells were imaged periodically over ~100 days. The stains stored in 1X PBS at 4 °C show no decay over time. Scale bar, 200 μm.

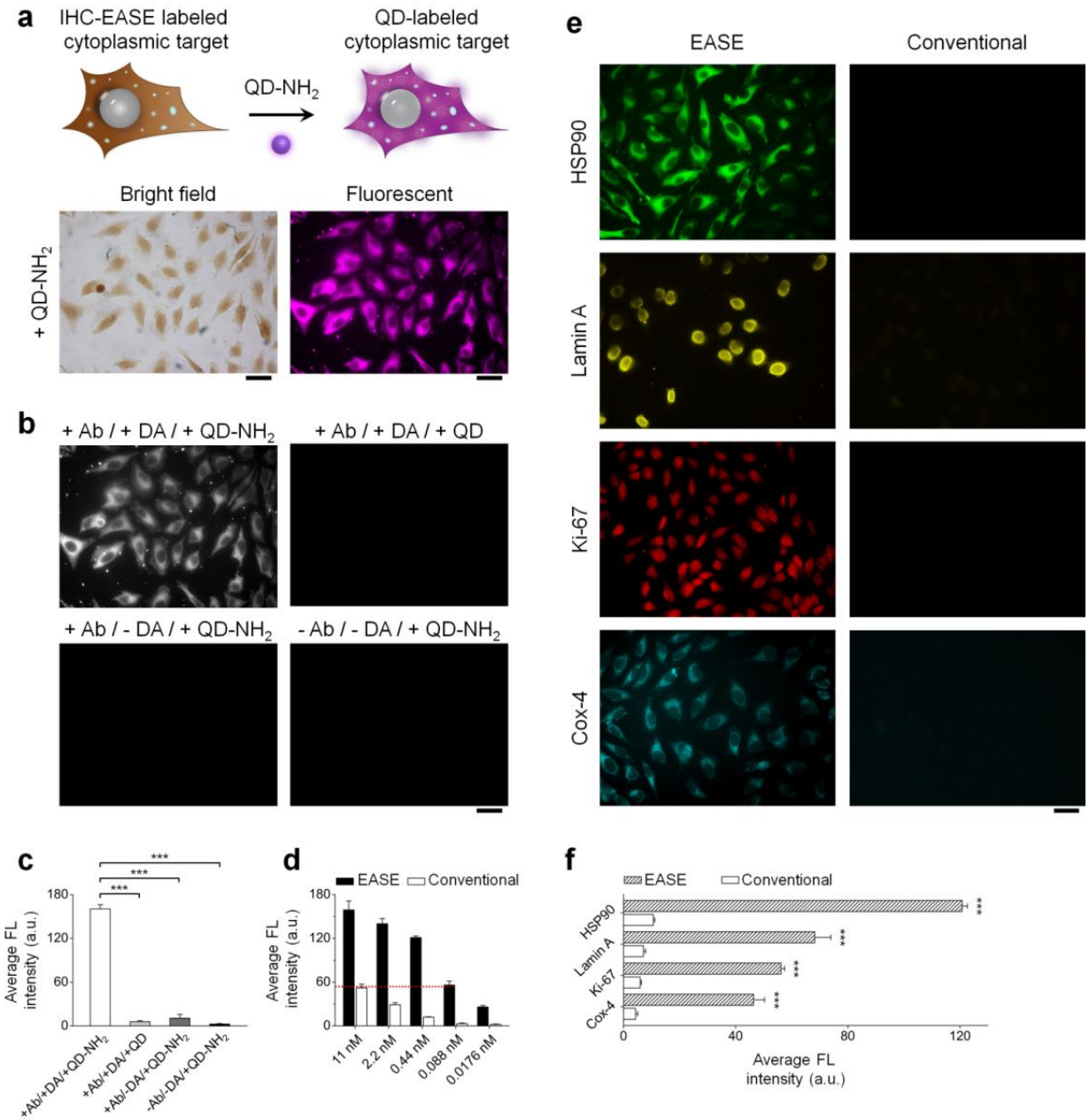

**Figure 2.1.5. IF-EASE cell staining.** (**a**) IHC-EASE labeled cells further labeled with QD-PEG-$NH_2$ ($NH_2$-QDs). Fluorescence imaging of HSP90 shows consistent staining pattern after QD adsorption (compared with the bright-field images before QD labeling). Scale bar, 50 μm. (**b & c**) Verification of staining specificity by comparing the experiment group with various controls (antibody and/or dopamine is missing). Scale bar, 50 μm. The intensity differences between the experiment and controls are highly significant. ***$P$ < 0.001 by two-tailed $t$-test. Error bars, s.d. over four different images. (**d**) Quantitative evaluation of IF staining intensity with or without EASE. Signal intensity obtained using IF-EASE at 88 pM 1'Ab is roughly the same as the intensity obtained with conventional IF at 11 nM 1'Ab. Error bar, s.d. over four different images. (**e**) Fluorescence imaging of four targets (HSP90, Lamin A, Ki-67, and Cox-4) stained with or without EASE at a 1'Ab dilution of 1:25,000. Scale bar, 50 μm. (**f**) Quantitative measurements of the cell fluorescence intensity showing in (**e**). The differences are statistically significant. ***$P$ < 0.001 by two-tailed $t$-test. Error bars, s.d. over four different images.

To probe the sensitivity enhancement of EASE, fluorescence probes were brought into the assay after PDA deposition, taking advantage of PDA's remarkable reactivity to any fluorophores with primary amines and the convenience of quantifying fluorescence signals21. Pegylated QDs with terminal amines were used as the fluorophore because of their photostability so that fluorescence intensity can be accurately measured[34, 92]. As shown in **Figure 2.1.5a**, the fluorescent staining pattern matches that of the PDA, confirming that QD-$NH_2$ immobilization is confined to the PDA network. The specificity is further demonstrated by the control experiments where either one of the key agents (Ab or dopamine) is missing, an isotype 1'Ab is utilized, or un-functionalized QDs are used. As shown in **Figure 2.1.5b, c** and **Figure 2.1.6**, the control experiments did not produce detectable signals.

To evaluate the sensitivity quantitatively, staining was first performed on HSP-90. Unlike ELISA assays where target molecules can be easily immobilized at various densities, engineering cells with a variety of precisely controlled antigen expression levels is extremely difficult. Instead, we reduced the concentration of the 1'Ab in a serial fashion to bring down the signal intensity. As shown in **Figure 2.1.5d** and **Figure 2.1.7**, at 1'Ab concentration of 88 pM, IF-EASE achieves the same signal strength compared to conventional IF using 1'Ab of 11 nM, yielding a 125 fold reduction in 1'Ab concentration, which not only indirectly demonstrates the enhancement in imaging sensitivity, but also shows the possibility to reduce the cost of expensive biological agents such as antibodies.

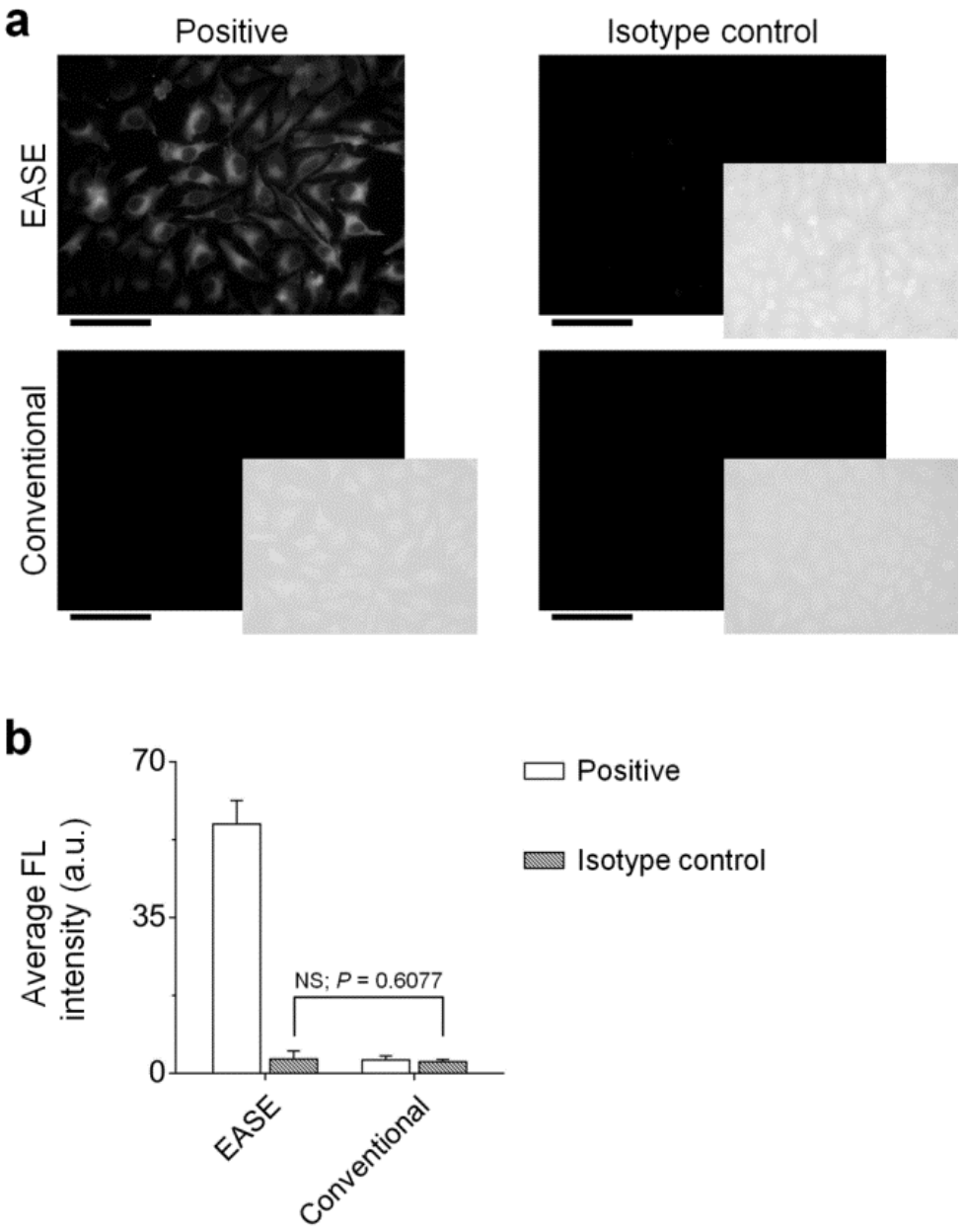


**Figure 2.1.6. Verification of IF-EASE staining specificity.** (**a**) Fluorescence micrograph showing HSP90 (88 pM 1'Ab) staining under various conditions: experiment group (left panels) and control group using isotype rabbit IgG as the 1'Ab (right panels), using both IF-EASE (top panels) and conventional IF (bottom panels). Scale bar, 100 μm, exposure time 100 ms. To better illustrate the background levels, long exposure (2 seconds) images were also shown for the control panels. (**b**) By comparing the isotype Ab control for IF and IF-EASE, no significant background increase was observed. $P > 0.1$, not significant by two-tailed *t*-test. Error bars, s.d. over four different images.

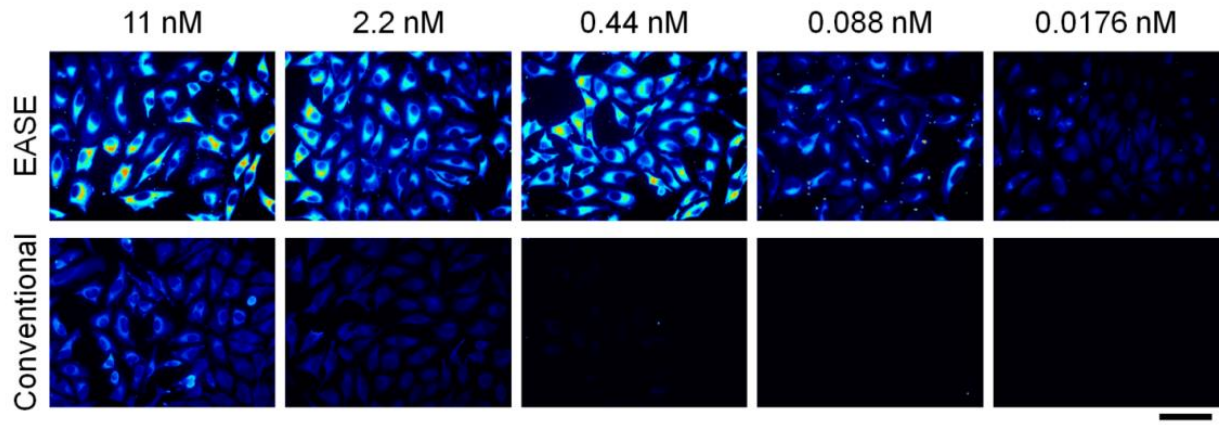


**Figure 2.1.7. Signal strength comparison for IF and IF-EASE in single cells.** False-color (heat map) fluorescence imaging of cells stained with various concentrations of primary antibody. Scale bar, 100 µm.

The signal enhancement is a result of amplifying a limited number of target molecules (as well as bound HRP) to a polymer network that captures a large number of QDs. Indeed, when we applied four tumor biomarkers (HSP90, Lamin A, Ki-67, and Cox-4) covering various intracellular locations, a 1:25,000 dilution of the primary antibodies (typical IF dilution factor ~ 1:100) produced bright and specific staining similar to those from conventional IF assay using high concentration of 1'Ab (**Fig. 2.1.5e & f**). In contrast, without EASE, 1:25,000 dilutions of the primary antibodies did not produce detectable signals.

Next, to directly evaluate IF-EASE in imaging low-abundance targets, we silenced the expression of GAPDH in HeLa cells using RNA interference (RNAi)-mediated gene knockdown[93]. As shown in **Figure 2.1.8**, 36 h post RNAi, the characteristic cytoplasmic distribution of GAPDH can be clearly visualized using IF-EASE, and it is only barely detectable using IF alone. Similarly, at 60 h post RNAi, trace amount of GAPDH can still be detected using IF-EASE, but not with IF alone. This result clearly shows the power of EASE in detected low-abundance targets in cells.

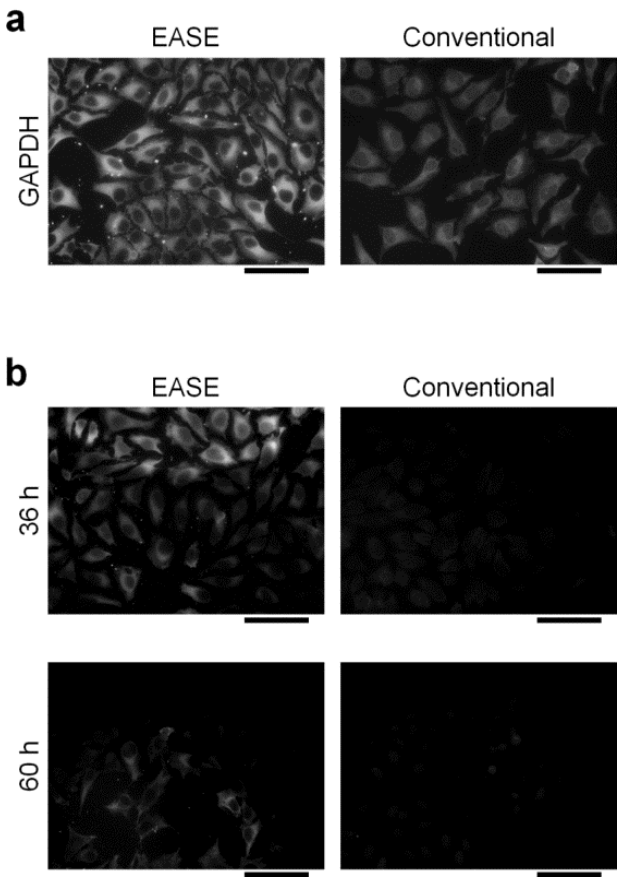


**Figure 2.1.8. Imaging low-abundance protein in cells.** GAPDH expression in HeLa cells was suppressed by RNAi. (**a**) Fluorescence images of GAPDH stained by IF-EASE and conventional IF before RNAi. Scale bar, 100 µm. (**b**) Fluorescence images showing GAPDH staining 36 h and 60 h post RNAi. Despite majority of GAPDH protein is degraded, trace amount left is still picked up by IF-EASE but not by conventional IF. Scale bar, 100 µm.

## 2.1.3 EASE for suspension microarrays

Suspension microarrays are highly multiplexed genotyping and phenotyping platforms used in molecular biology, drug screening, and disease diagnosis[94-96]. Compared to planar microarrays that are spatially addressable, suspension microarrays are often fabricated by doping microspheres with combinations of luminescent materials and are decoded with flow cytometers (e.g., Luminex microbeads)[97, 98]. To determine whether an unknown analyte is present or not, conventional methodologies such as direct or sandwich hybridization and immuno-recognition are applied. The suspension microarrays offer advantages such as faster binding kinetics, but their detection sensitivities are essentially the same as the planar counterparts[99].

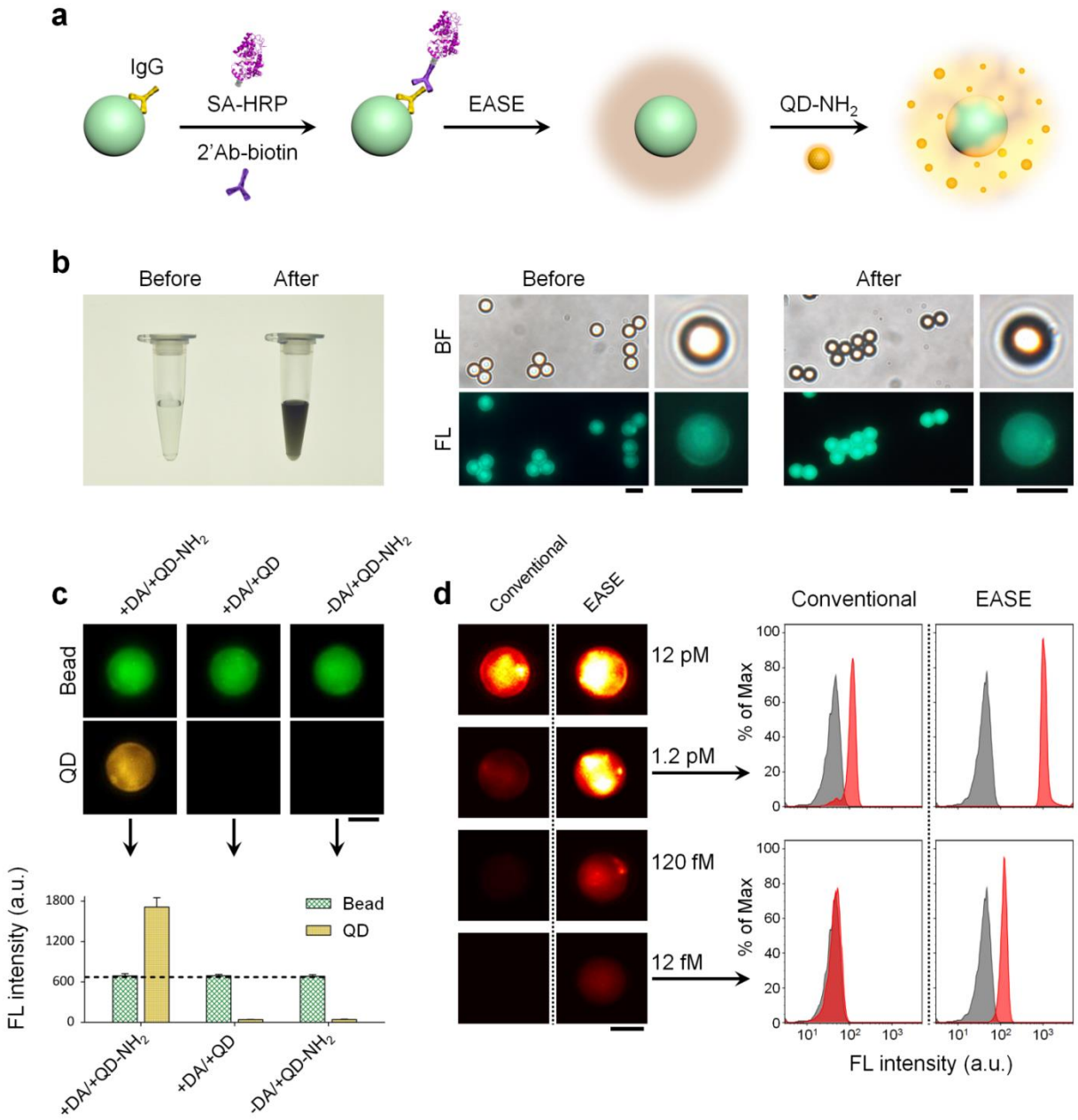
a
IgG
SA-HRP
2'Ab-biotin
EASE
QD-NH2
b
Before
After
Before
After
BF
FL
c
+DA/+QD-NH2
+DA/+QD
-DA/+QD-NH2
Bead
QD
FL intensity (a.u.)
1800
1200
600
0
Bead
QD
+DA/+QD-NH2
+DA/+QD
-DA/+QD-NH2
d
Conventional
EASE
12 pM
1.2 pM
120 fM
12 fM
Conventional
EASE
% of Max
100
80
60
40
20
0
10¹
10²
10³
FL intensity (a.u.)

**Figure 2.1.9. Ultrasensitive suspension microarray enabled by EASE.** (**a**) Schematic illustration showing signal enhancement by EASE. Fluorescent microspheres coated with Abs (IgG) capture 2'Ab-biotin (a model target) in solution. The target molecule is detected by streptavidin (SA)-HRP complex, which catalyzes PDA deposition followed by QD adsorption. (**b**) Effect of PDA coating on microsphere fluorescence ($1\times10^9$ beads $ml^{-1}$, 12 nM 2'Ab-biotin). The dark microsphere suspension shows successful PDA coating, while the microscopy images show no obvious fluorescence change before and after the coating. Scale bar, 5 μm. (**c**) Representative fluorescence images of the microspheres and corresponding quantitative flow cytometry data showing strong QD signals only when both QD-PEG-$NH_2$ and dopamine are present ($1\times10^6$ beads $ml^{-1}$, 12 pM 2'Ab-biotin). Scale bar, 3 μm. Error bars, s.d. over three replicates. (**d**) Quantitative evaluation of detection sensitivity enhancement by EASE. Representative single-bead fluorescence images and flow cytometry histograms ($1\times10^6$ beads $ml^{-1}$) show that the detection sensitivity of the microsphere immunoassay is improved by 100 folds (from 12 pM to 1.2 fM). Scale bar, 3 μm.

To demonstrate the compatibility of EASE with suspension microarrays, fluorescent microspheres were coated with immunoglobulin G (IgG) to detect a model target, biotinylated 2'Ab. Presence or absence of the analyte was detected with either streptavidin-QD conjugates (conventional sandwich method) or the EASE technology (streptavidin-HRP, PDA, and QD-NH2) (**Fig. 2.1.9a**). Before comparing their sensitivities, we first tested whether PDA deposition on microsphere surface reduces the microsphere fluorescence (would interfere with fluorescence barcodes if multiple colors were doped inside). PDA coating on microsphere is easy to monitor since the solution quickly turns dark brown because of the chromogenic PDA (**Fig. 2.1.9b**), yet microscopy images reveal virtually no change of the microsphere fluorescence before and after PDA coating. QDs were used as the fluorescent reporter because of their tunable fluorescence emission and the large Stokes shift (to avoid spectral overlap with the microsphere fluorescence). For QDs with various surface chemistries, only aminated QDs bind with the microspheres, showing their interaction is due to the chemical reactions between amines and PDA rather than physical adsorption (**Fig. 2.1.9c**). Next, we proceeded with the sensitivity comparison. Flow cytometry and fluorescence microscopy both reveal that the target IgG can be detected at a concentration of 1.2 pM using conventional sandwich assay (streptavidin-QD as the reporter), whereas addition of EASE can push the detection limit down by 2 orders of magnitude (fM range) (**Fig. 2.1.9d**).

To assess the specificity of this ultrasensitive detection assay, two control experiments were conducted. In the first experiment where the target molecule was missing, no significant signals were detected with or without the EASE process, confirming the antibody-antigen binding specificity (**Fig. 2.1.10**).

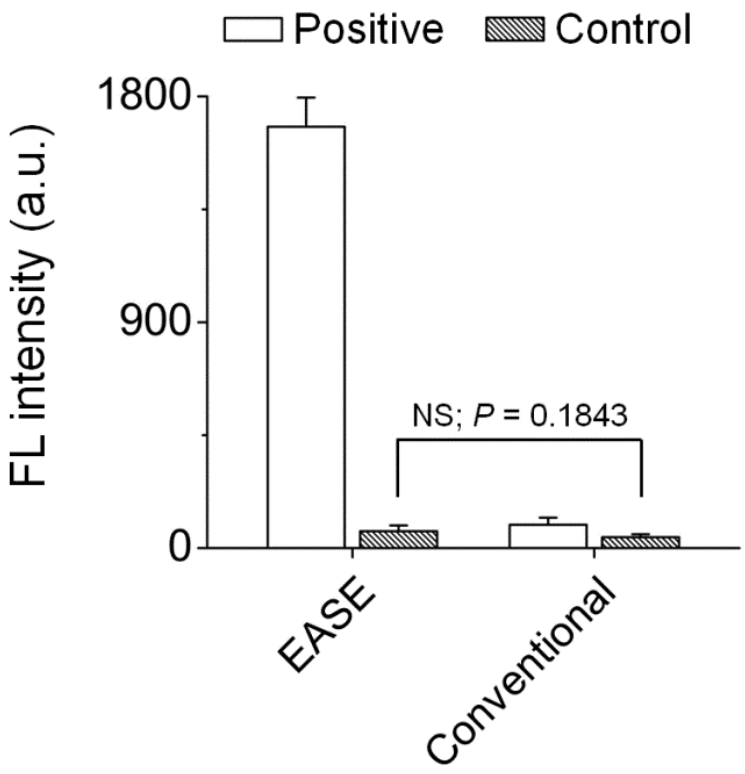


**Figure 2.1.10. Verification of suspension microarray specificity.** At a target (biotinylated 2'Ab) concentration of 12 pM, the EASE technology can help conventional suspension microarray to easily detect the target (two blank bars). When the target is missing (control, dashed bars), the background signal intensity suspension microarrays with or without EASE are statistically indistinguishable. *P* > 0.1, NS, not significant by two-tailed *t*-test. Error bars, s.d. over three replicates.

Second, we also evaluated the potential crosstalk in a dual-color setup. Two types of microspheres were mixed together, green microsphere with mouse IgG on the surface and yellow microsphere with rabbit IgG. When anti-rabbit IgG was added as the target, strong fluorescence signal from the EASE assay was only detected on the yellow microspheres, free of crosstalk (**Fig. 2.1.11**). This remarkable detection specificity lays the foundation for massive parallel screening applications when additional optical barcodes are used[100].

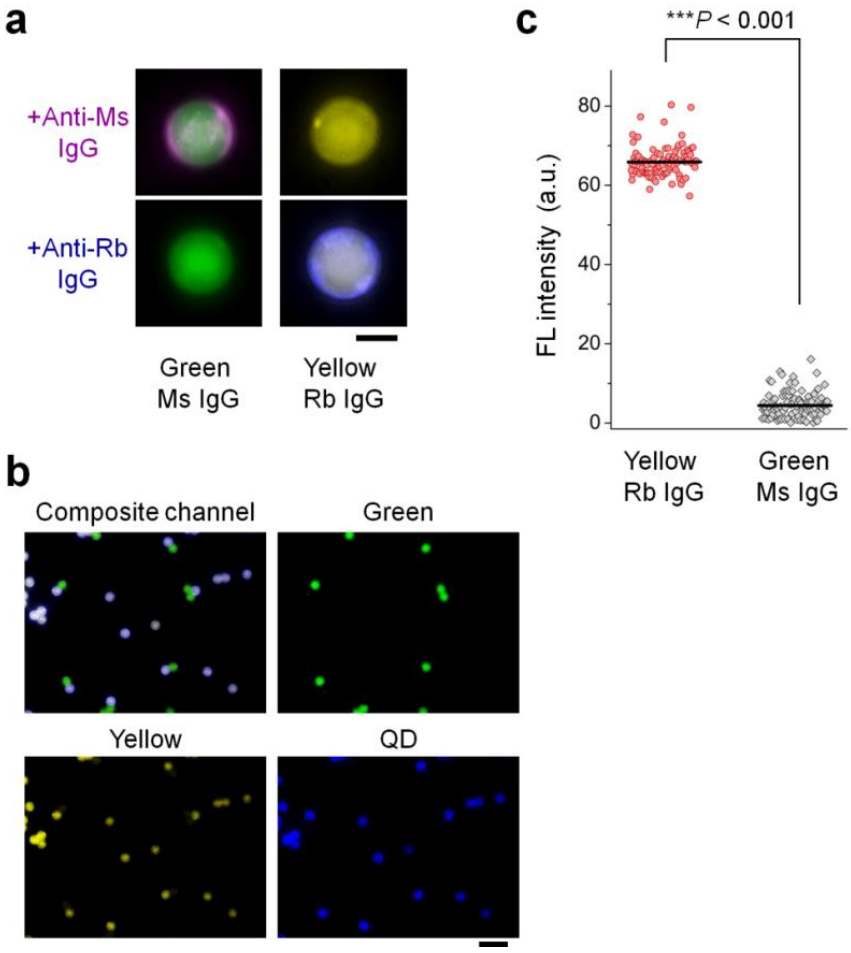


**Figure 2.1.11. Assessment of detection crosstalk using multicolor microspheres.** Mouse IgG and Rabbit IgG are immobilized on green and yellow microspheres separately. (**a**) When matching anti-mouse IgG and anti-rabbit IgG were used as the detection probes, QD fluorescence on beads surface (following PDA deposition) is detected by microscopy. Mismatched antibody pairs do not produce QD fluorescence. Scale bar, 3 µm. (**b**) Two-color microspheres mixture incubated with only one target, anti-rabbit IgG. QD deposition only occurs on the yellow microspheres. Scale bar, 15 µm. (**c**) Single bead counting show detection of the anti-rabbit IgG at 100% accuracy (counted 100 beads for each color).

## 2.1.4 EASE for ELISA and lateral flow strips

To demonstrate the versatility of EASE, it was further applied to ELISA and immuno strip tests, robust and poplar biochemical assays. These assays using antibodies for molecular recognition and enzyme-catalyzed chromogen development for target identification are easy to perform, gaining broad applications in both research and clinical laboratories. On the other hand, their mediocre detection sensitivities are

also well acknowledged[101]. Compared to the suspension assays discussed above, a technical feature of these assays is that they are performed on solid supports (flat surfaces or porous membranes), rendering the sample washing steps quick and easy (dip in and out of washing buffer without the need of a centrifuge). This seemingly insignificant feature combined with the unique bioconjugation capability of PDA allows EASE to be carried over for more than one time. For example, in the first round of amplification, HRP molecules bound to the target can catalyze localized deposition of PDA. The PDA layer can in turn capture a large number of HRP molecules that are capable of catalyzing the conversion of chromogenic substrates (**Fig. 2.1.12a**).

To probe the sensitivity and specificity of ELISA with or without EASE, a standard sandwich ELISA assay was established to detect mouse IgG (model target). Serial dilution of the target molecule resulted in gradients of color development that can be easily visualized by naked eye (substrate: tetramethylbenzidine or TMB). As shown in **Figure 2.1.12b**, without EASE, color development in the ELISA assay is visible at a target concentration between $10^{-7}$ and $10^{-8}$ g $ml^{-1}$; with EASE as an add-on step, the color development becomes clearly visible at $10^{-12}$ g $ml^{-1}$. This significantly improved limit of detection (LOD) was further quantified on a plate reader. The standard curve relating signal strength and target concentration is shown in **Figure 2.1.12c** (left panel), with a zoomed-in low-concentration range plotted in the right panel. The plate-reader readouts reveal the ELISA LODs (3 s.d. from the background) were 85.3 fg $ml^{-1}$ (with EASE) and 108 pg $ml^{-1}$ (without EASE), a 1,266 fold improvement. The specificity of the ELISA assays was demonstrated by control experiments where the target molecule was missing (**Fig. 2.1.13**) or high-concentration non-target analytes were introduced (**Fig. 2.1.14**). The robustness of the EASE-aided ELISA was further demonstrated in another four disease biomarkers: HIV capsid antigen p24 (HIV p24), kallikrein 3 (KLK3), c-reactive protein (CRP), and vascular endothelial growth factor (VEGF). Similarly, their calculated values of LODs of ELISA-EASE are 2.87 fg $ml^{-1}$, 0.31 pg $ml^{-1}$, 0.24 pg $ml^{-1}$, and 11.5 fg $ml^{-1}$ (**Fig. 2.1.12d**), respectively, representing an average 1,217 fold improvement over the conventional ELISA (**Fig. 2.1.12e**).

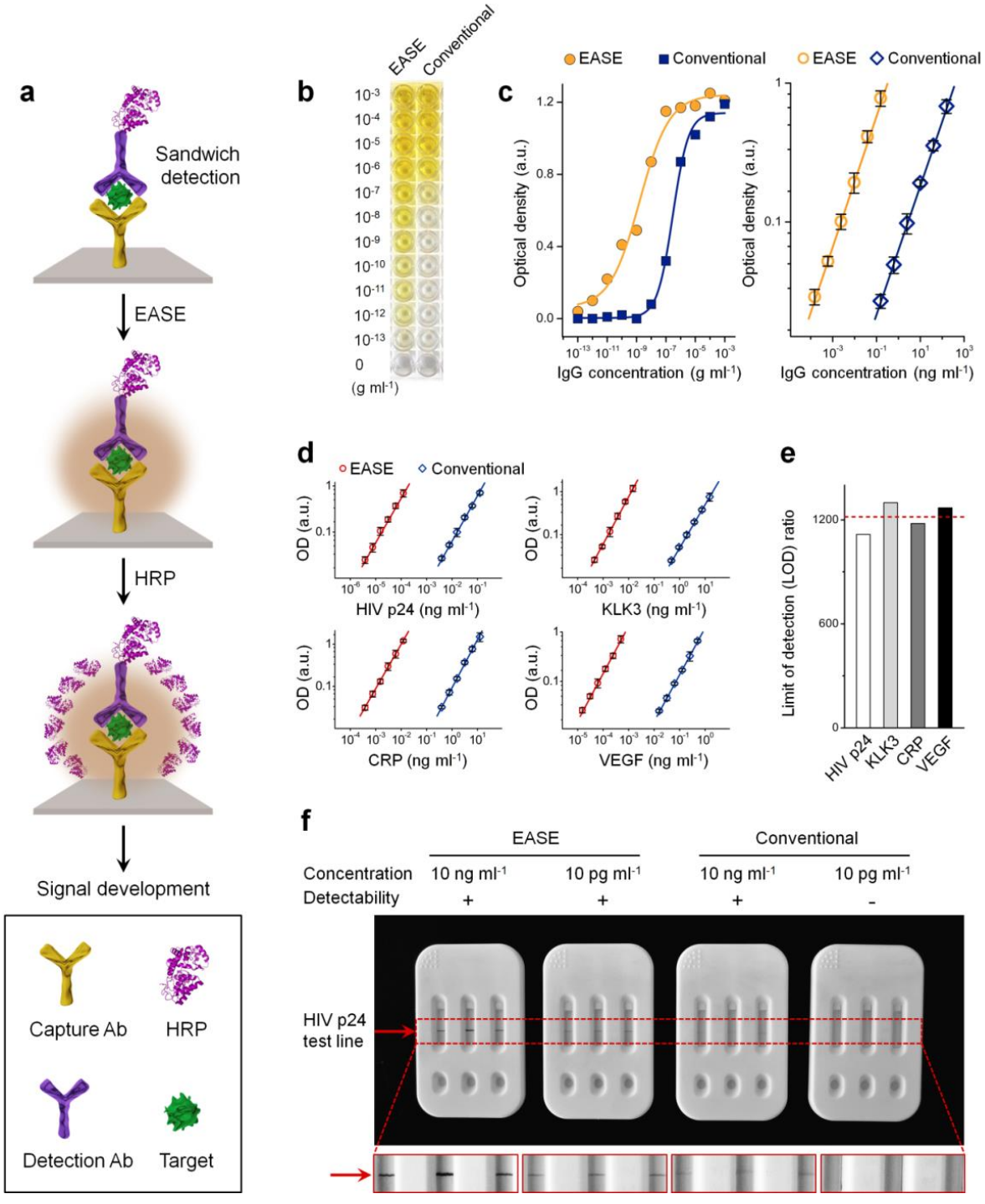
a
Sandwich detection
EASE
HRP
Signal development
Capture Ab
HRP
Detection Ab
Target
b
EASE
Conventional
(g ml-1)
c
EASE
Conventional
Optical density (a.u.)
IgG concentration (g ml-1)
IgG concentration (ng ml-1)
d
HIV p24 (ng ml-1)
KLK3 (ng ml-1)
CRP (ng ml-1)
VEGF (ng ml-1)
OD (a.u.)
e
Limit of detection (LOD) ratio
HIV p24
KLK3
CRP
VEGF
f
EASE
Conventional
Concentration
10 ng ml-1
10 pg ml-1
Detectability
HIV p24 test line

**Figure 2.1.12. ELISA and lateral flow strips with EASE.** (**a**) Schematic illustration of the signal enhancement process. Upon target detection, a layer of PDA is coated around the target molecule, which allows a large number of HRP to adsorb. These HRP molecules, in turn, catalyze the substrate (TMB) conversion at a significantly enhanced rate. (**b**) Visual assessment of the detection sensitivity of ELISA-EASE using mouse IgG as a model target in comparison with conventional ELISA. Colored solutions are visualized in ELISA-EASE wells at target concentrations as low as $10^{-13}$ g $ml^{-1}$, while the conventional assay only produces detectable colors at $10^{-8}$ to $10^{-9}$ g $ml^{-1}$ concentration range. (**c**) Quantitative comparison using values obtained from a plate reader shows the assay response over the full target concentration range (left) and a zoomed-in range close to the essays' LODs (right). Improvement of approximately 3 orders of magnitude is seen. Error bars, s.d. over three replicates. (**d**) ELISA working curves for four targets, HIV p24, KLK3, CRP, VEGF, with or without EASE. Error bars, s.d. over three replicates. (**e**) The average of LOD improvements for all four targets is around 1,200 fold. (**f**) Strip tests of HIV p24 with or without EASE. Positive signals (indicated by the red arrow) are observed at 10 ng $ml^{-1}$ and 10 pg $ml^{-1}$ for the EASE-strips, but the conventional strips can only detect down to 10 ng $ml^{-1}$. Each strip represents three replicates.

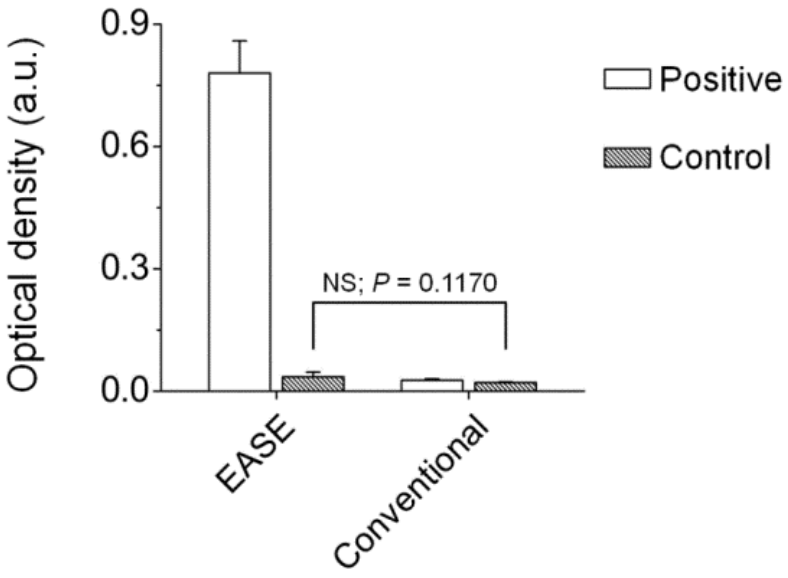


**Figure 2.1.13. Verification of ELISA-EASE specificity.** At a target (mouse IgG) concentration of 154 pg $ml^{-1}$, the target presence can be detected by ELISA-EASE easily, but not by ELISA alone. Without the target molecule, the signal intensity difference of ELISA with or without EASE is statistically insignificant. $P > 0.1$, NS, not significant by two-tailed *t*-test. Error bars, s.d. over three replicates.

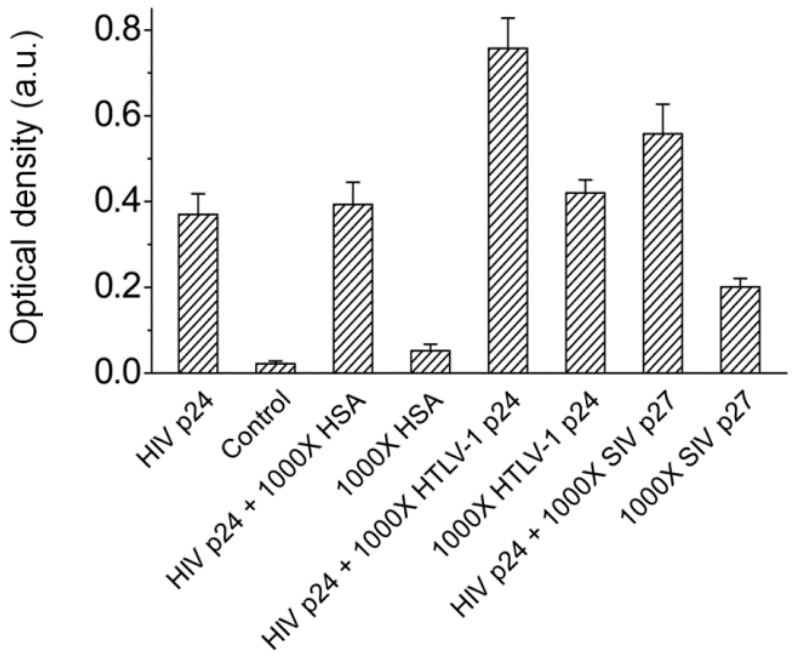


**Figure 2.1.14. Confirmation of ELISA-EASE specificity and cross-reactivity.** At the target (HIV p24) concentration of 60 fg $ml^{-1}$, the target presence can be detected by ELISA-EASE easily with very low background from the controls (without target molecule). To further test the selectivity, 1,000 X more concentrated proteins (60 pg $ml^{-1}$) including human serum albumin (HSA), HTLV-1 p24, SIV p27 were spiked into 1X (60 fg $ml^{-1}$) HIV p24 solution, and probed by ELISA-EASE. No significant cross-reactivity was observed for HSA. The non-specific proteins (HTLV-1 p24 and SIV p27) that are more similar to p24 only produce appreciable signals when their concentrations are 1,000 x higher than p24.

Building on the remarkable sensitivity enhancement achieved on ELISA plate, the HIV biomarker p24 was further tested using lateral flow strips, a simple and low-cost bioassay, sharing similar detection mechanism as ELISA (conducted in porous membranes rather than on flat surfaces), but is better suited for point-of-care diagnosis[102]. As shown in **Figure 2.1.12f** and **Figure 2.1.15**, the strip test detects p24 at a concentration of 10 ng $ml^{-1}$ (spiked HIV p24 antigen in phosphate-buffered saline (PBS)) under conventional conditions (using DAB as the substrate), whereas EASE can improve it by at least 1,000 times (10 pg $ml^{-1}$), enabling ultrasensitive detection of HIV antigens with naked-eye.

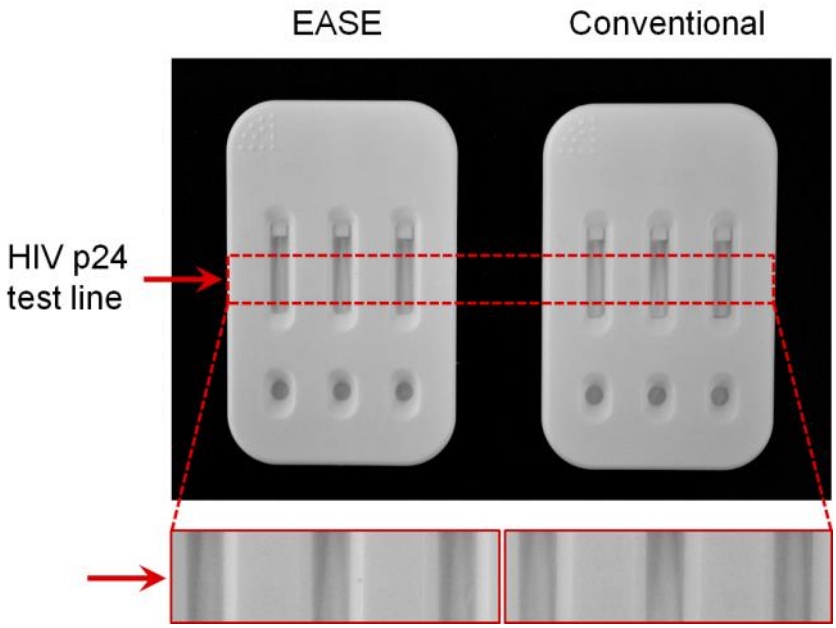


**Figure 2.1.15. Verification of lateral flow test specificity.** Control experiments where the target P24 protein is absent show no detectable signals with or without EASE.

With the EASE platform validated in the above bioassays, we moved on to real biological problems that require much improved detection sensitivity to resolve. We demonstrate the power of EASE assay in detection of four biologically significant low-abundance targets, HIV in blood, in situ protein detection in brain samples, Zika virus (ZIKV) imaging in the placenta, and programmed death-ligand 1 (PD-L1) in tumor.

### 2.1.5 Early diagnosis of HIV using ELISA-EASE

Early diagnosis of HIV provides timely access to treatments, thus improving patient outcomes and quality of life[103]. A study of ~16,000 patients on antiretroviral (ARV) treatment between shows substantial numbers beginning ARV later than recommended due to late diagnosis[104]. For adults, early knowledge of infection also leads to behavioral changes that can reduce 30% new infections per year[105]. For children and infants, earlier diagnosis is even more important. At this time, over 200,000 children acquire HIV worldwide every year, with most cases due to transmission to infants from their mothers during pregnancy, birth, or breastfeeding. HIV progresses rapidly in infants – without treatment they can die

within months – but early treatment by ART greatly improves outcomes. Large-scale programs (e.g., President's Emergency Plan for AIDS Relief (PEPFAR)) have made ART available, but early diagnosis remains a barrier to treatment.

HIV can be detected in blood or plasma by 1) nucleic acid amplification tests (NAAT), 2) lab based immunoassays (ELISA), or 3) rapid tests (similar to pregnancy tests). In general, NAAT is sensitive, but very expensive, and rapid test is of low performance and cannot be used in infants (false positive due to antibodies from mom). For decades, ELISA has been the workhorse laboratory HIV test and is the first test in the Centers for Disease Control and Prevention (CDC) testing algorithm. The sensitivity of ELISA, however, has been a major limitation (even for the most recent generation, detections are made around two weeks after infection). How to push the detection to an earlier time has been a major unmet clinical need.

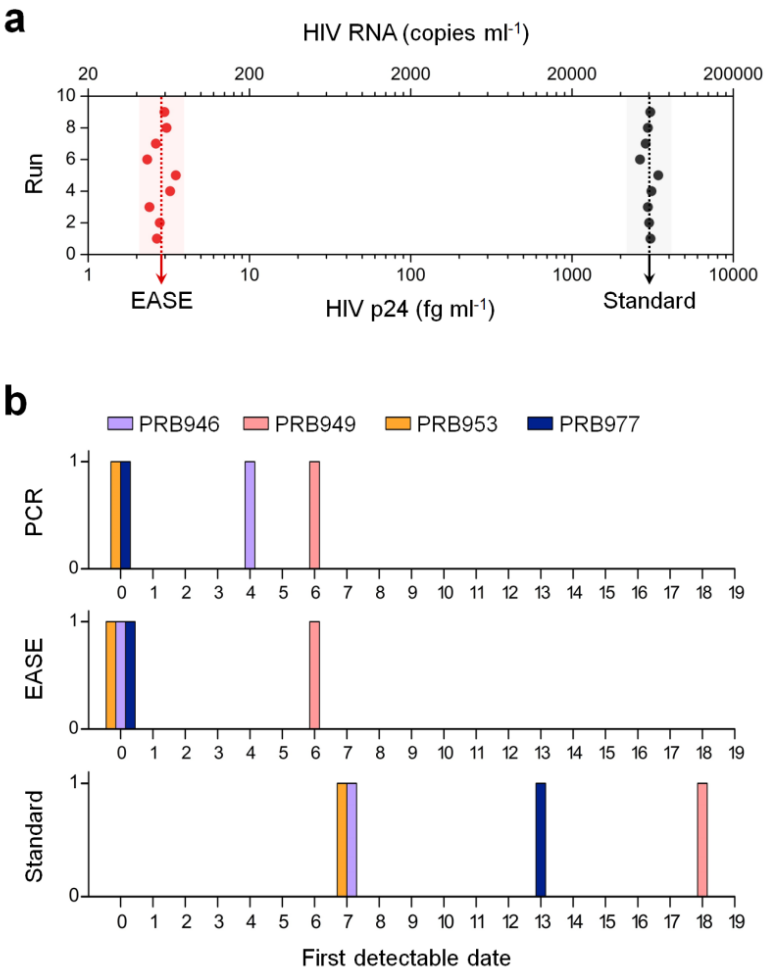

**Figure 2.1.16. Early diagnosis of HIV in patient blood samples using ELISA-EASE.** (**a**) LOD values (obtained in 9 runs performed on different days) of ELISA with or without EASE for detection of HIV p24 spiked in plasma. The average LOD of ELISA with EASE is 2.84 fg $ml^{-1}$, 1,060 fold lower than that of the standard ELISA. (**b**) First date when HIV infection becomes detectable since the first bleed for the four patients. Positive detection is made within the first week for ELISA-EASE and PCR, whereas the conventional ELISA detects infection 2-3 weeks later when the viral load is high.

We used the ELISA assay to detect p24 antigen in real patient samples, the key protein that makes up most of the viral capsid, in patient sera. Quantitative measurement of its presence in serum is highly valuable to blood screening, diagnosis of infection, and monitoring treatment responses[106]. As recommended by the CDC, HIV p24 antigen detection using ELISA offers a number of advantages such as reduced cost, fast assay times, and applicability in low-resource settings. On the other hand, it is commonly acknowledged that p24 ELISA is an insensitive assay with a LOD of approximately 10 pg $ml^{-1}$[1,107] limiting its use to samples with high viral loads. Layering the EASE technology on top, however, can convert the ordinary detection sensitivity of ELISA to extraordinary, as shown in the above ELISA studies conducted in buffers.

| Patient ID | Phlebotomy date | EASE (pg $ml^{-1}$) | Standard (pg $ml^{-1}$) |
|---|---|---|---|
| PRB 946 | 0 | 0.006* | ↓ |
| | 4† | 0.807 | ↓ |
| | 7 | 26.86 | 19.22* |
| | 11 | 39.70 | 50.63 |
| PRB 949 | 0 | ↓ | ↓ |
| | 6† | 0.029* | ↓ |
| | 9 | 0.561 | ↓ |
| | 18 | 22.05 | 17.22* |
| PRB 953 | 0† | 0.043* | ↓ |
| | 3 | 1.320 | ↓ |
| | 7 | 23.36 | 16.01* |
| | 10 | 39.99 | 50.97 |
| PRB 977 | 0† | 0.009* | ↓ |
| | 2 | 0.121 | ↓ |
| | 13 | >100 | >100* |
| | 15 | >100 | >100 |

↓ blow the quantitation range;
† first detectable date using PCR;
* first detectable date using ELISA.

**Table 2.1.1 Viral load assessment using ELISA, ELISA-EASE, and PCR in four HIV-infected patients' plasma samples.** Serial bleeds were collected from individual patients over a course of 18 days during the development of HIV infection (first bleed as day 0). ELISA-EASE detects HIV p24 as early as PCR does.

To demonstrate its ability in clinical diagnosis, sera from 24 donors (obtained from SeraCare, Milford, MA and Discovery Life Sciences, Los Osos, CA) were assayed with either standard ELISA or ELISA with EASE. Among these samples, four were obtained from HIV-infected patients (PRB 946, PRB 949, PRB 953, and PRB 977) whose viral loads had been determined using PCR (data from SeraCare); and 20 HIV-negative donors were included to exclude biased results due to nonspecific interactions. The analytical LOD was determined by spiking HIV p24 antigen of various concentrations into plasma. Results from 9 repeated runs performed on 9 consecutive days show a highly consistent value (**Fig. 2.1.16a**) of 2.84 fg $ml^{-1}$ for ELISA-EASE, representing a 1,060 fold improvement over standard ELISA. Theoretical calculation indicates that this level of protein detection corresponds to samples contain approximately 56 copies $ml^{-1}$ of RNA or 28 $ml^{-1}$ viral particles[108], on par with the sensitivity of PCR, which requires sophisticated instruments and long assay time. Indeed, when ELISA-EASE was applied to the HIV infected patient samples (multiple bleeds obtained on different dates), it can pick up the viral infection on average 10 days earlier (similar to PCR) than the standard ELISA assay (**Table 2.1.1** and **Fig. 2.1.16b**). This remarkable sensitivity potentially can provide a precious time window for treating other time-sensitive infections (e.g., viral and bacterial infections) and diseases (e.g., heart diseases) as well.

## 2.1.6 Resolving corticotrophin releasing factor (CRF) distribution in the brain using IF-EASE

CRF and its canonical G-protein coupled receptors, corticotrophin releasing factor receptor type 1 (CRFR1) and CRFR2 play an essential role in stress responsiveness regulated by the central nervous system[109]. Alterations in the function of the CRF system and changes in CRF receptor signaling are broadly linked to neuropsychiatric disorders including addiction and depression[110]. The ability to resolve the spatial distribution of CRF receptors in the brain will transform our understanding of how these

receptors influence neural circuit function and how alterations in the expression and distribution of these receptors contribute to the disease states. Detection of CRF receptors has been largely limited to in situ hybridization detection on the mRNA level and radio-ligand binding assays[111, 112], which provide poor spatial resolution. High-resolution localization of these receptors using conventional immunostaining techniques has been limited by the low levels of receptor expression. To test the effectiveness of EASE technology to enhance CRFR1 detection using antibody staining, we performed immunostaining for CRFR1 using conventional methods and EASE. Analysis of CRFR1 detection revealed only a small number of CRFR1-positive cells in the cerebral cortex of the mouse brain using conventional immunostaining (**Fig. 2.1.17**). In contrast, EASE amplification revealed numerous CRFR1-positive cells including both small diameter and large diameter cells, indicative of expression in both interneurons and pyramidal neurons, respectively (**Fig. 2.1.17b**). Additionally, EASE detection of CRFR1 localized the protein to the cell bodies of both cell types, as well as the apical dendrites of pyramidal neurons.

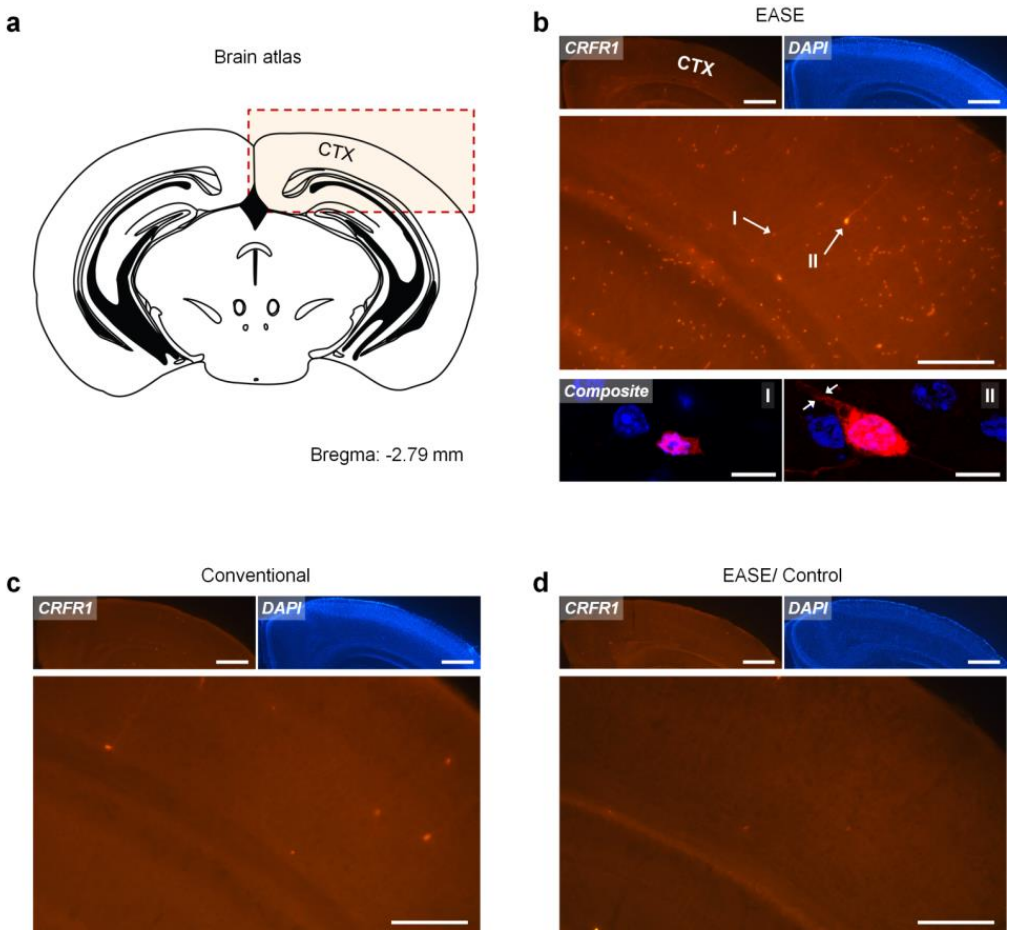

**Figure 2.1.17. Resolving the distribution of CRFR1 in the brain.** (**a**) Schematic of cerebral cortex (CTX) in the mouse brain (Bregma: -2.79 mm). (**b-d**) Representative fluorescence images of CRFR1 neurons in CTX, counter stained with DAPI. Scale bar for the CRFR1 and DAPI images (top panels), 200 µm. Scale bar for the zoom-in images (middle panels), 100 µm. Scale bar for the composite confocal images (bottom panels), 5 µm. A large number of CRFR1-positive cells are observed through IF-EASE staining, but not with the conventional IF. Staining specificity is also confirmed by including the control experiment (without primary Ab). Interneurons (I) and pyramidal neurons (II) are indicated by arrows in the CRFR1 image of (**b**). Apical dendrites of pyramidal neurons are shown by the arrows in the composite image (II).

## 2.1.7 Direct imaging of ZIKV infection in the placenta using IF-EASE

Zika is a mosquito-borne flavivirus initially identified in the 1950s' in monkeys. Its recent outbreak in Brazil has been correlated with cases of fetal microcephaly as well as Guillian-Barré, raising major global concerns. While there is now scientific consensus, including our own work[113], that ZIKV indeed causes fatal brain injury, the mechanism of how it occurs is largely unknown. qPCR and deep sequencing are capable of identifying ZIKV in the placenta, but cannot elucidate the means by which ZIKV crossed the placental barrier due to their inability to track ZIKV through conventional immunohistologic analysis. The EASE technology enabled direct visualization of ZIKV infected cells within the placental chorionic villus core of pregnant nonhuman primates. As shown in **Figure 2.1.18a**, the infected cells appear in the mesenchymal core in close proximity to the cytotrophoblast cell layer. The EASE technology opens a new avenue to understand fetal brain injury and microcephaly caused by ZIKV and potentially to prevent mother-to-child transmission.

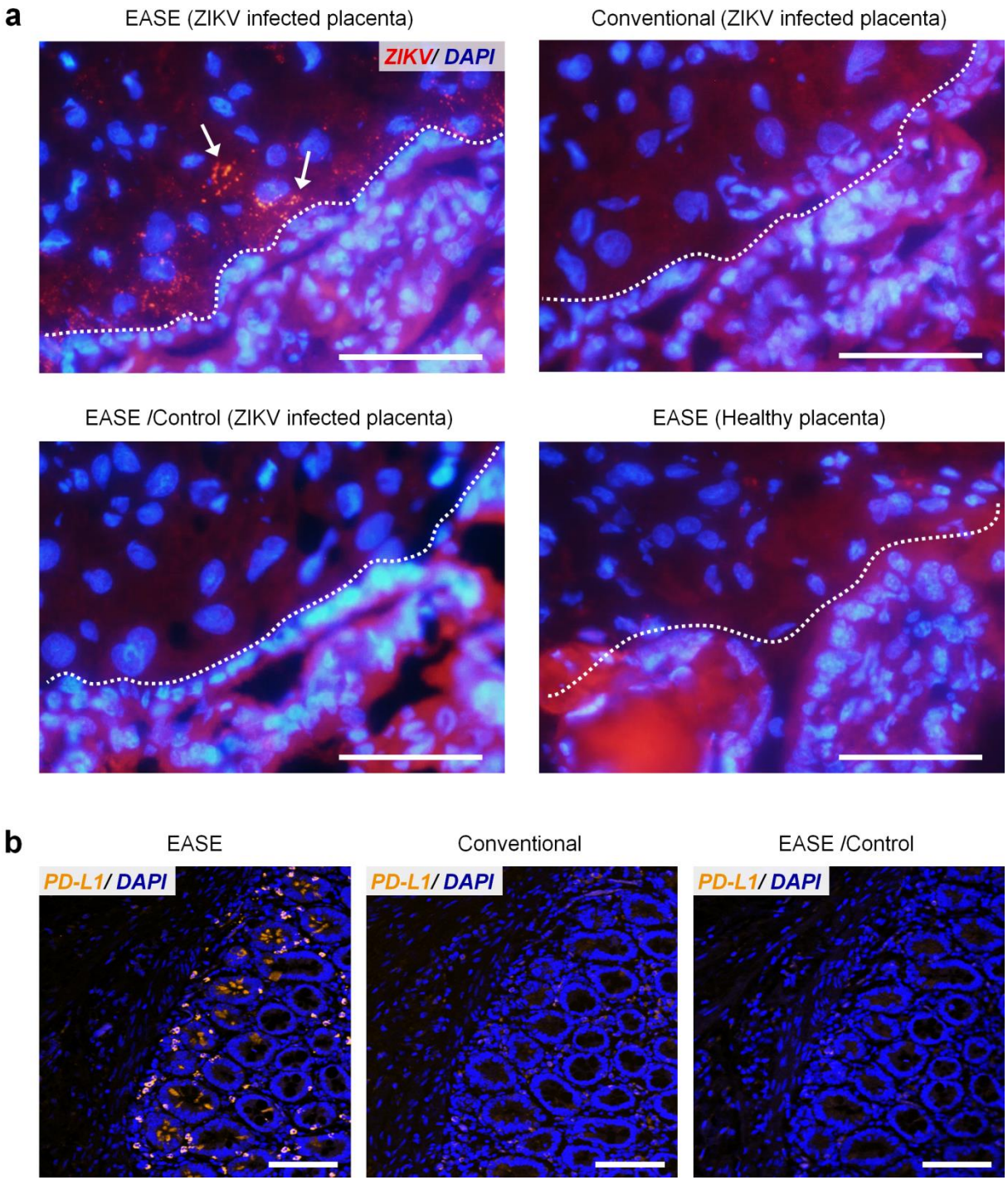
a
EASE (ZIKV infected placenta)
ZIKV/ DAPI
Conventional (ZIKV infected placenta)
EASE /Control (ZIKV infected placenta)
EASE (Healthy placenta)
b
EASE
PD-L1/ DAPI
Conventional
PD-L1/ DAPI
EASE /Control
PD-L1/ DAPI

**Figure 2.1.18. Sensitive imaging of ZIKV in placenta and PD-L1 in FFPE pancreatic tumor specimens.** (**a**) Representative fluorescent images of ZIKV in placental chorionic villi (nuclei counter-stained with DAPI). Scale bar, 100 µm. ZIKV infected cells indicated by arrows can only be observed through IF-EASE, not with conventional IF. Staining specificity is verified using the controls (without primary Ab, or IF-EASE in non-infected placentas). Dashed lines, cytotrophoblast cell layer (identified by morphology). Infected cells appear within the chorionic villus core and villi beneath in close proximity to the cytotrophoblast cell layer. The red background signal is due to tissue autofluorescence, which can be reduced under confocal imaging where the excitation source is a laser (narrow band). (**b**) Representative fluorescence micrographs of PD-L1 expression in pancreatic specimens from the patient (SU-09-21157), samples counter-stained with DAPI. Scale bar, 100 µm. PD-L1 staining can be easily observed through the IF-EASE technology, but very difficult using the conventional IF. The control experiment (without primary Ab) did not show detectable signals either.

## 2.1.8 PD-L1 imaging in patient tumor specimens using IF-EASE

PD-L1, also known as CD-274 or B7-H1 is a cell surface ligand, which binds and triggers PD-1, a potent immune-inhibitory receptor on T cells[114]. Monoclonal antibodies which block this interaction, by binding either PD-L1 or PD-1 have proven to be efficacious immune-oncology agents in a variety of tumor types49-54. Immunohistochemical assays for detecting PD-L1+ cells within tumors have also been approved as companion diagnostic tests for patient selection in limited therapeutic indications, but broader application of anti-PDL1 IHC is limited by both biologic and technical factors. PD-L1 expression vary broadly across a wide range and levels below the detection thresholds of current IHC assays still have biologic significance[115-120]. Therefore, we set out to test whether EASE can be used to detect low-level PD-L1 signals while preserving good signal-to-noise ratios, an unmet clinical need for immunotherapy. Clinical formalin-fixed paraffin-embedded (FFPE) pancreatic tumor specimens with low PD-L1 expression were used to test the performance of IF-EASE with the conventional IF. As shown in **Figure 2.1.18b**, specific detection of PD-L1 is readily achieved with IF-EASE, whereas the signals detected by conventional IF technology are at extremely low levels. These exciting results address the unmet clinical need of detecting low abundance targets in FFPE tissues (high autofluorescence background), proving the feasibility for future large-scale studies.

### 2.1.9 Summary

Since the invention of a simple immersion procedure for slow coating of a PDA layer onto virtually any surface, this mussel-inspired surface chemistry has intrigued the scientists to explore a wide variety of applications such as sensing, tissue engineering, and bioimaging[121, 122]. Similar to the oxidase-catalyzed rapid melanin deposition found in invertebrates, we found that HRP can speed up PDA polymerization by approximately 300 times. More importantly, due to the excellent reactivity of PDA to primary amines, the polymer chains quickly crosslink with nearby biomolecules (rich in many reactive chemical groups including $NH_2$), forming a localized network for immobilization of a large number of reporter molecules and nanoparticles (as long as they have accessible amine groups) for signal enhancement while preserving the spatial information. This technology, dubbed EASE, has been studied in various contexts including immunohistochemistry and immunofluorescence for single cell imaging, ELISA, lateral flow strips, and suspension microarrays. Consistently, it improves bio-imaging and -detection sensitivity by at least 2-3 orders of magnitude regardless of the assay format. Most significantly, EASE achieves this remarkable sensitivity without changing the design of common assay formats, or requiring specialized equipment and reagents, in contrast to most ultrasensitive detection technologies invented in the past 10-20 years. Therefore, EASE can be directly incorporated into the current biology and clinical infrastructure for immediate impact.

The flexibility of this general technology has allowed us to go beyond technology development and tackle a number of real biological problems that cannot be solved (at least extremely difficult to solve) using conventional bioassays. We applied EASE to ELISA-based detection of HIV infection in patient blood samples. For comparison, the measurements were benchmarked against the gold-standard assays, standard ELISA and PCR. Our results show that the EASE-enabled ELISA outperforms the standard ELISA by >1,000 times in sensitivity, which translates into detection of 2-3 viruses per 100 µl of blood. This sensitivity is similar to that of PCR-based approaches allowing HIV detection 1-2 weeks earlier, yet ELISA is faster and cheaper to perform, and compatible with point-of-care (POC) applications (costly thermocycler not needed). Furthermore, EASE is a robust process that can be applied to a variety of real biological and clinical problems, such as brain biology, in situ virus imaging in placenta, and PD-L1

imaging for immunotherapy. We envision that no or only minor developments are needed for broad technology adoption and application, such as early detection of viruses and bacteria without culture, counting disease biomarkers of low abundance, and monitoring treatment responses.

## 2.2 ELIMINATING SIZE-ASSOCIATED DIFFUSION CONSTRAINS FOR RAPID ON-SURFACE BIOASSAYS WITH NANOPARTICLE PROBES

Mass transfer limitation is typically experienced when the probe binding kinetics greatly exceeds probe diffusion from solution to the surface, which creates a depletion layer next to the surface and exposes the specimen to a substantially lower effective probe concentration[8] that free probes in bulk solution need to fill via diffusion (**Fig. 2.2.1a**). Given the relatively fast binding kinetics of most common target-probe systems, such as antigen-antibody and DNA-DNA' pairing[123, 124], mass transfer limitation might be expected even in on-surface assays utilizing relatively small molecular probes. For example, IgG probe depletion layer forms around microspheres in suspension within 1 min of incubation, taking over an hour for the assay to reach steady state[125]. Mass transfer effect amplifies dramatically for larger nanoparticle probes, as diffusion constant inversely relates to particle size by Stokes-Einstein equation, while the time it takes for reaction to switch to a diffusion control is directly proportional to diffusion constant:[125]

$$D = k_b T / 6\pi\eta r \quad (1)$$

$$\tau = D/(k_f \Gamma_0)^2 \quad (2)$$

where D is diffusion constant, $k_b$ is the Boltzmann constant, η is the fluid viscosity, T is absolute temperature, r is probe hydrodynamic radius, τ is time to reaching diffusion control, $k_f$ is intrinsic forward binding rate, and Γ0 is the surface concentration of reactive sites. As a result, assays proceed at a substantially slower speed, often requiring multi-hour incubation steps and presenting a major technical hurdle for time-sensitive applications, such as intraoperative rapid diagnosis, and advanced multi-step procedures, such as multi-cycle staining methodologies increasingly employed for in situ single-cell molecular profiling[126-129].

Mild shaking routinely employed with on-surface assays typically achieves probe mixing within the bulk solution, but fails to eliminate the depletion layer due to the lack of efficient fluid movement next to the surface, thus offering little improvement in assay performance. Similar challenges are faced by efforts in assay miniaturization and automation with microfluidic devices[130], where laminar flow offers poor mixing, quickly developing a diffusion-limited probe depletion layer[131, 132]. A number of techniques have attempted

to address this issue. Some examples include introduction of turbulence[133], oscillatory flow[134], and rapid liquid exchange and recirculation for improved reagent mixing in microfluidic devices and microchambers[135], use of electric field for active probe enrichment at the surface[136], and perfusion of samples through porous membranes for enhanced interaction between the surface and reagents[137]. Diffusion constraints have also been recognized with cell and tissue staining applications, where microfluidic processors[138], ultrasound mixing[139], microwave treatment[140], and automated instruments have been used to speed-up the process[141]. Yet, often marginal benefits achieved at an expense of substantially increased complexity with strictly application-specific setups still limit use of these methodologies in routine practice.

Here, we explore the extent of diffusion constraints on the assay kinetics with nanoparticle probes and report a conceptually distinct methodology of cyclic draining-replenishing (CDR) to completely bypass diffusion limitation regardless of the probe size. CDR directly addresses the need for efficient molecular mixing at the surface by repeatedly draining all liquid from the specimen to strip the surface of its probe depletion layer and then refilling the surface with a freshly mixed probe solution, consistently exposing the surface to bulk probe concentration and reusing the same probe solution through multiple cycles (**Fig. 2.2.1b**).

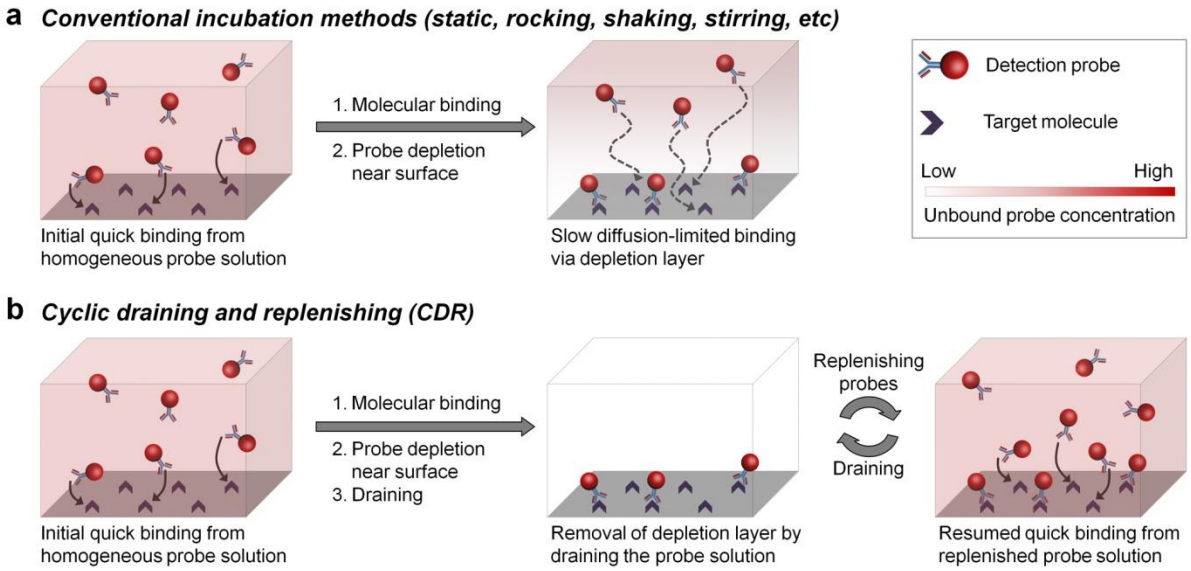

**Figure 2.2.1. Schematic illustration of the cyclic draining-replenishing (CDR) technology. (a)** Conventional surface-based assays typically employ static incubation for probe binding to surface-immobilized targets. As a result of fast binding kinetics and slow diffusion, probes get rapidly depleted from the volume adjacent to the surface, yielding a substantially lower effective probe concentration and limiting further target labeling kinetics by slow mass transfer from the bulk solution. Improving bulk fluid exchange by rocking, stirring, and shaking has little effect on depletion layer near the surface. **(b)** CDR method enables rapid target labeling by eliminating the probe diffusion limitation. The probe depletion layer is quickly removed by complete draining of the staining solution, rather than speeding up probe diffusion in the solution. Subsequent refilling of the surface with the same bulk solution keeps the probe concentration near the surface constant and equivalent to bulk solution, thus maintaining fast target labeling kinetics.

In a simple implementation of this concept broadly accessible to biomedical laboratories (**Fig. 2.2.2**), a molecular target or specimen is immobilized on the plate surface (usually bottom of the well), covered by the probe solution, and sealed with Parafilm. The sealed plate is then affixed onto a laboratory rotator and inverted at the rate of 8 rpm, creating a continuous flow of solution from the well bottom onto the walls, Parafilm cover, and then back to the well bottom, thus driving the probe solution from and to the surface-bound specimen and mixing the solution in the process. Complete solution drainage by gravity and surface tension ensures efficient molecular mixing directly at the specimen surface. At the same time, it is unlikely that any target degradation occurs during the CDR procedure, as effects of drying on the target antigen were only observed if the sample was dried for over 5 minutes prior to replenishing the solution. To demonstrate the concept, we show that both ELISA and IF can be achieved within minutes without sacrificing data quality. Furthermore, we highlight the utility of CDR methodology for rapid single-cell molecular profiling by staining multiple targets in multiple cycles, making this high-content molecular analysis a highly practical approach for the first time.

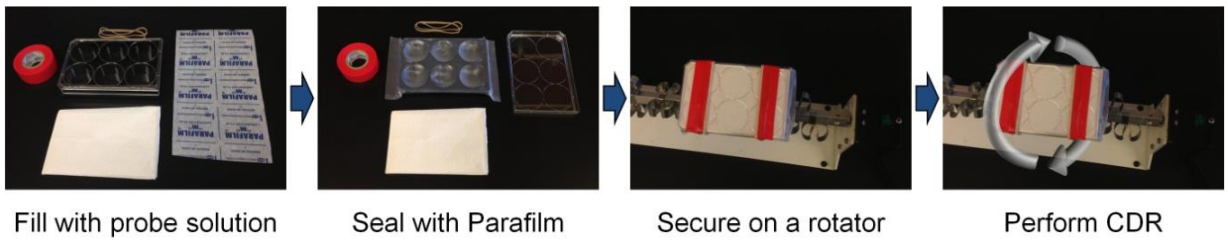

**Figure 2.2.2. Experimental setup for performing cyclic draining-replenishing procedure.** Glass-bottom (for cell staining) or plastic (for ELISA) 6-well plates with specimens attached onto the bottom of wells were filled with 1 ml/well probe solution, sealed with Parafilm, and secured onto a rotator for CDR. Plate inversion created a steady solution flow from the well bottom onto a cover Parafilm and back, thus draining and replenishing the specimen with a probe solution in a cyclic manner.

## 2.2.1 Kinetics of rapid ELISA diagnostics

To explore the effect of mass transfer on the overall assay kinetics and quantitatively evaluate the performance of CDR methodology in a diffusion-limited assay setting, a simple ELISA was established by immobilizing a molecular target (mouse IgG) onto the bottom surface of a microplate at an optimal concentration as determined from standard curves for each probe (**Fig. 2.2.3**). Two types of probes routinely employed in ELISA were tested – relatively small monomeric horseradish peroxidase (HRP)-linked antibody (Ab) bioconjugate (mono-HRP, 8-10 nm in size) and larger polymeric HRP-Ab cluster (poly-HRP, ~100 nm) as an ultrasensitive nanoprobe. The CDR incubation process was benchmarked against the well-established conditions, static incubation on a bench and rotary shaking on a shaker. Nonspecific binding was checked by either using rabbit IgG as a target together with anti-mouse HRP-Ab detection or using anti-rabbit HRP-Ab probe on mouse IgG-coated plates.

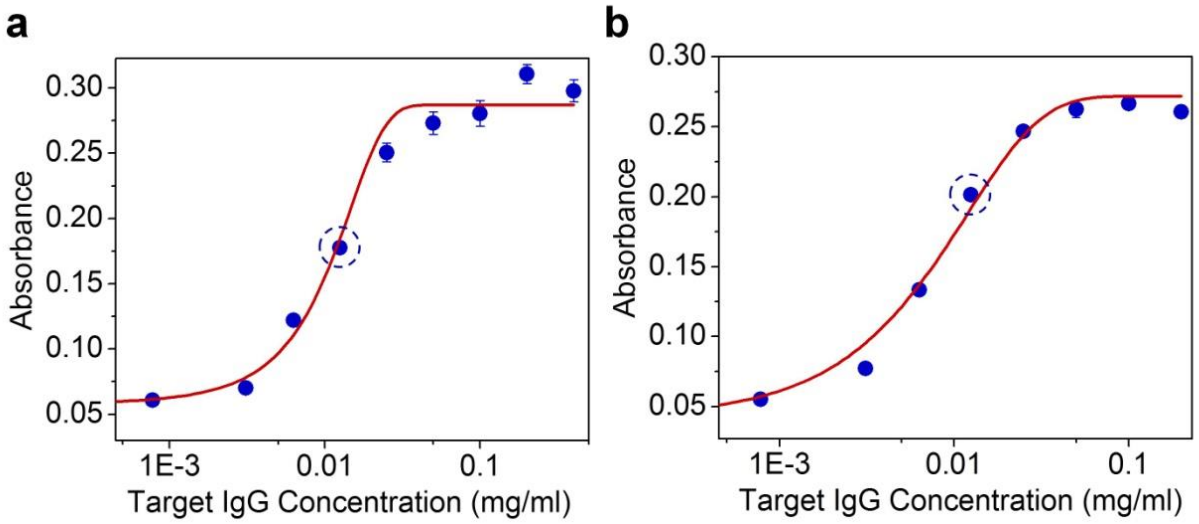

**Figure 2.2.3. Working curves for model ELISA.** ELISA plates were coated with target molecules (IgG isolated from mouse serum) at varying target concentrations and then incubated under static conditions with either goat anti-mouse Poly-HRP (a) or Mono-HRP (b) probes. Colorimetric assessment of the Mouse IgG abundance on the plate surface was then performed using 1-Step Turbo TMB-ELISA substrate and measuring the solution absorbance at 450 nm with a plate reader. Target IgG concentrations in the middle of the assay linear range (blue dashed circles) were picked for the study of target labeling kinetics under static incubation, rotary shaking, and cyclic draining-replenishing conditions.

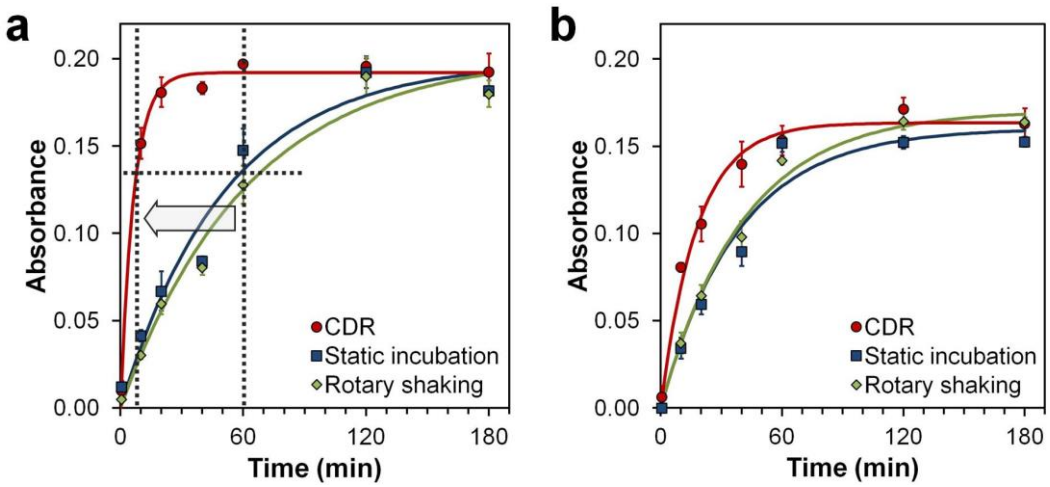


**Figure 2.2.4. Kinetics of rapid ELISA diagnostics. (a)** Assay performed with Poly-HRP probes exhibited slow mass transfer-limited kinetics under static incubation (t½ = 36 min) and rotary shaking (t½ = 43 min) conditions, but demonstrated a dramatically improved performance with CDR (t½ = 5 min). Compared to standard ELISA protocols where incubation typically takes 1 h, CDR reaches the same staining intensity in 7 minutes. **(b)** Smaller mono-HRP probes exhibited faster kinetics under static incubation (t½ = 26 min) and rotary shaking (t½ = 28 min) conditions, featuring further improvement in assay speed with CDR (t½ = 12 min). Solution absorbance at 450 nm with respect to assay time is shown and fitted by an exponential curve. Background absorbance by the TMB substrate alone was subtracted from all measurements. Error bars represent one standard deviation from triplicate assays.

Assay kinetics was characterized by the increase in HRP substrate absorbance at 450 nm with respect to incubation time (10-180 min), and the data was fitted with an exponential growth curve modeled after a typical bimolecular association-dissociation reaction[142]. Under the conventional static and rotary shaking conditions, both Poly-HRP and Mono-HRP probes exhibited only initial fast binding, which then slowly leveled off as incubation time increased. In contrast, CDR produced a sustained fast binding, quickly reaching equilibrium (**Fig. 2.2.4**). In comparison to a typical ELISA incubation time of ca. 1 hour, when a

major proportion of signal build-up happens without necessarily reaching equilibrium, CDR method produced the same signal intensity within 7 minutes of incubation with Poly-HRP nanoprobes, thus yielding an approximately one order of magnitude increase in assay speed (**Fig. 2.2.4a**), while retaining assay specificity. It should be noted, nonetheless, that all methods yielded similar maximum steady-state labeling intensities, confirming that only the diffusion component was eliminated by CDR, while keeping the antibody-antigen binding parameters unperturbed. It is also noteworthy that smaller mono-HRP probes, which already exhibited faster binding kinetics under static incubation, showed further increase in binding speed under CDR (**Fig. 2.2.4b**), confirming the presence of mass transfer limitation even with relatively small mono-HRP-Ab bioconjugates.

Importantly, CDR-based assay with Poly-HRP probes proceeded with a binding half-time of just 5 min, despite probes being over 100 nm in size. Considering typical kinetic parameters for antibody-antigen binding ($k_{on}$ = 5x10$^{5}$ M$^{-1}$ s$^{-1}$ and $k_{off}$ = 5x10$^{-4}$ s$^{-1}$), labeling half-time of 2-20 min can be estimated for 10-0.1 nM antibody concentration (i.e., an order of magnitude above and below $K_D$) and no mass transfer limitation. The half-time value of 5 min directly falls within this range, suggesting that the assay proceeds in reaction-limited regime under CDR incubation, while being heavily diffusion-limited under static and rotary shaking conditions.

It follows that the phenomenon of enhanced target labeling is directly associated with fluid draining from the surface rather than bulk fluid movement. The general perception that performing ELISA (or other surface-based bioassays) on a shaker or rocker would help with reagent mixing and improve binding kinetics is not supported by our data, which instead shows that static and shaking tests produce quite similar binding kinetics profiles and highlights the lack of additional molecular mixing at the surface via rotary shaking. In contrast, CDR eliminates diffusion limitation under a range of rotation rates, as long as efficient draining is achieved (**Fig. 2.2.5**).

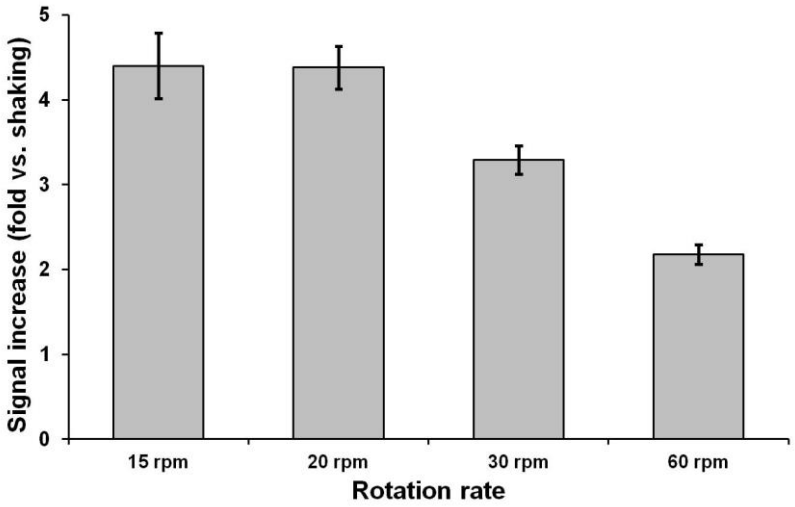


**Figure 2.2.5. Effect of rotation rate on CDR-based labeling efficiency.** ELISA plates were coated with target molecules (IgG isolated from mouse serum at 0.0125 mg/mL) and labeled with goat anti-mouse Poly-HRP for 10 minutes under rotary shaking (as a reference) and CDR at rotation rates of 15, 20, 30, and 60 rpm. Plates were then treated with Turbo TMB-ELISA substrate for colorimetric assessment of target concentration. Absorbance of CDR-based assays was normalized by ELISA signal from the rotary shaking reference. Similar to a 4-5 fold enhancement achieved with a laboratory rotator setup operating at 8 rpm, CDR can be performed at rotation rates of up to 20 rpm without loss of function. At higher rates CDR performance degrades, likely due to insufficient time provided for gravity-driven draining of solution. Error bars represent one standard deviation from triplicate assays.

## 2.2.2 Rapid IF staining with antibody-QDot nanoprobes

The utility of CDR approach for rapid immunofluorescence assays with nanoprobes was evaluated using fluorescent quantum dot (QDot)-antibody conjugates. QDot technology represents a promising tool for variety of sensing and imaging applications, and it has solved the multiplexing limitation often experienced with organic dyes. However, having a hydrodynamic size of ~20 nm, this advanced class of fluorescent imaging probes is expected to experience major diffusion constraints. Indeed, 2-3 hour incubation steps are typical with QDot-based IF[143].

Studies were performed on HeLa cells that were grown directly inside the wells of a glass-bottom 6-well plate, fixed with formaldehyde, and permeabilized with detergents to allow probe access to intracellular targets. Lamin A, a component of nuclear envelope, was used as a target due to its characteristic staining pattern, ease of quantitative analysis of staining intensity, and intracellular localization. The staining

specificity was confirmed by incubating cells with anti-Lamin A QDot-Ab and dye-labeled Ab probes under static conditions and comparing results to a conventional 2-step staining procedure performed with unmodified primary antibodies and secondary Ab-QDot bioconjugates (**Fig. 2.2.6a-d**).

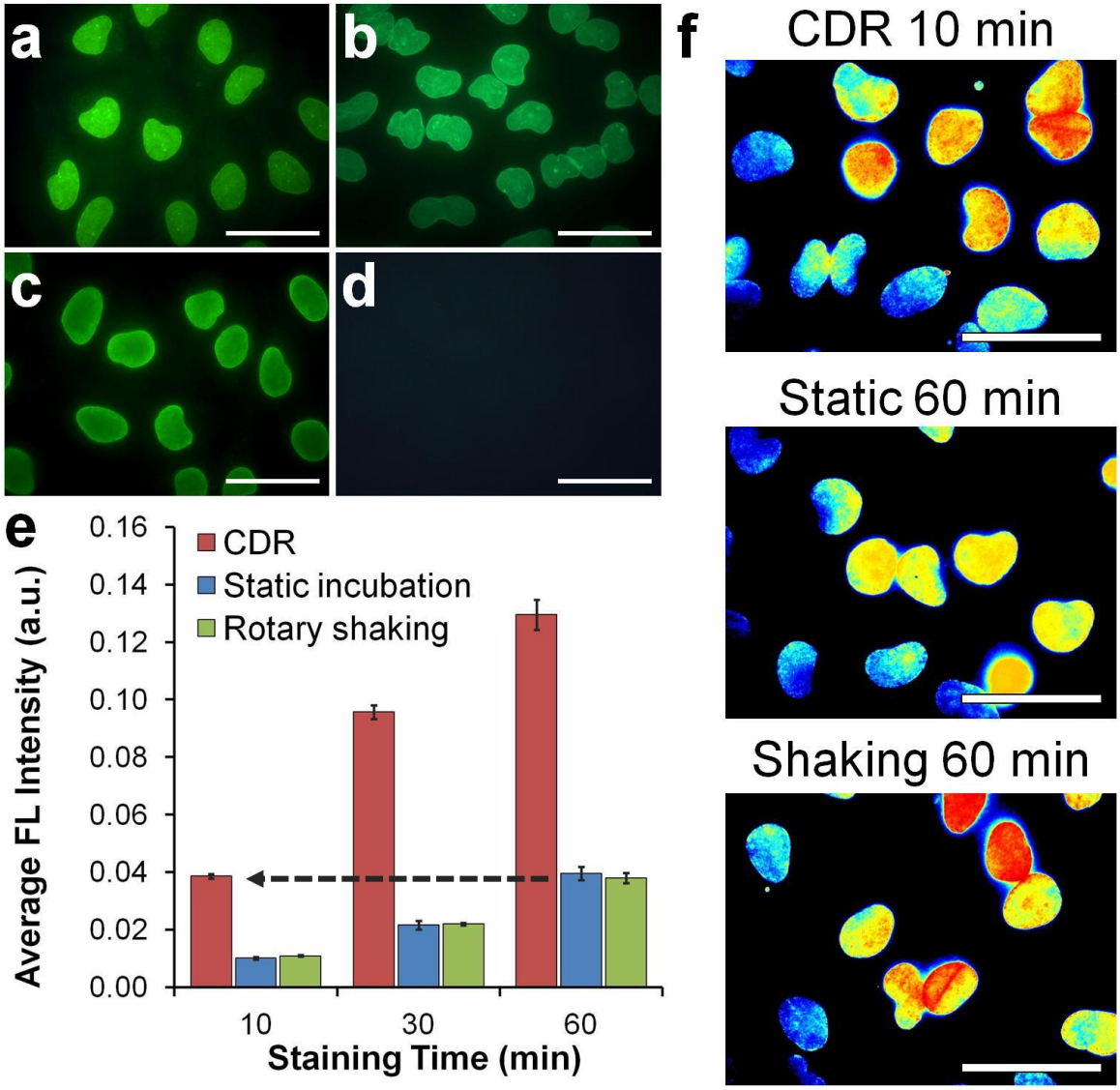

**Figure 2.2.6. Rapid immunofluorescence staining with QDot probes. (a-d)** Characterization of QDot-1'Ab and dye-labeled 1'Ab probes targeting Lamin A. One-step immunofluorescence images obtained with **(a)** QDot-1'Ab and **(b)** dye-labeled 1'Ab probes produced staining patterns consistent with the nuclear membrane localization of Lamin A and **(c,d)** results obtained with QDot-2'Ab in a conventional two-step staining procedure (positive Lamin A staining is shown in **(c)** and control lacking 1'Ab incubation in **(d)**). Scale bar, 50 μm. **(e)** Quantitative evaluation of staining intensity with respect to staining time achieved via CDR, static incubation, and rotary shaking techniques. Notably, CDR achieved comparable staining intensity 6 times faster than conventional methods, producing detectable signal within the first 10 minutes of staining. Error bars represent one standard deviation of an average Lamin A staining intensity from four different fields of view. **(f)** Representative cell staining intensity maps obtained after 10-min CDR in comparison to 60-min static and rotary shaking incubation. All images were normalized and color-coded with a heat map for direct comparison of staining pattern and intensities. Scale bar, 50 μm.

The evolution of staining intensity under CDR, static incubation, and rotary shaking was monitored over a period of 8 h. Consistent with the expectation of slow diffusion-limited kinetics, IF staining indeed approached a steady-state intensity level only after 8 hours of incubation under static and shaking conditions (**Fig. 2.2.7**). At the same time, CDR efficiently reduced the binding time toward saturation to 2 hours. More importantly, under practical IF staining applications, it took just 10 min to yield the same level of fluorescence signals of 1-hour conventional IF incubation (**Fig. 2.2.6e,f**).

Taking advantage of the substantial enhancement of binding kinetics with CDR, we proceeded to explore two applications previously inaccessible with conventional IF methods: background-free monitoring of staining evolution and high-content single-cell molecular profiling in practical time frame (hours rather than a week).

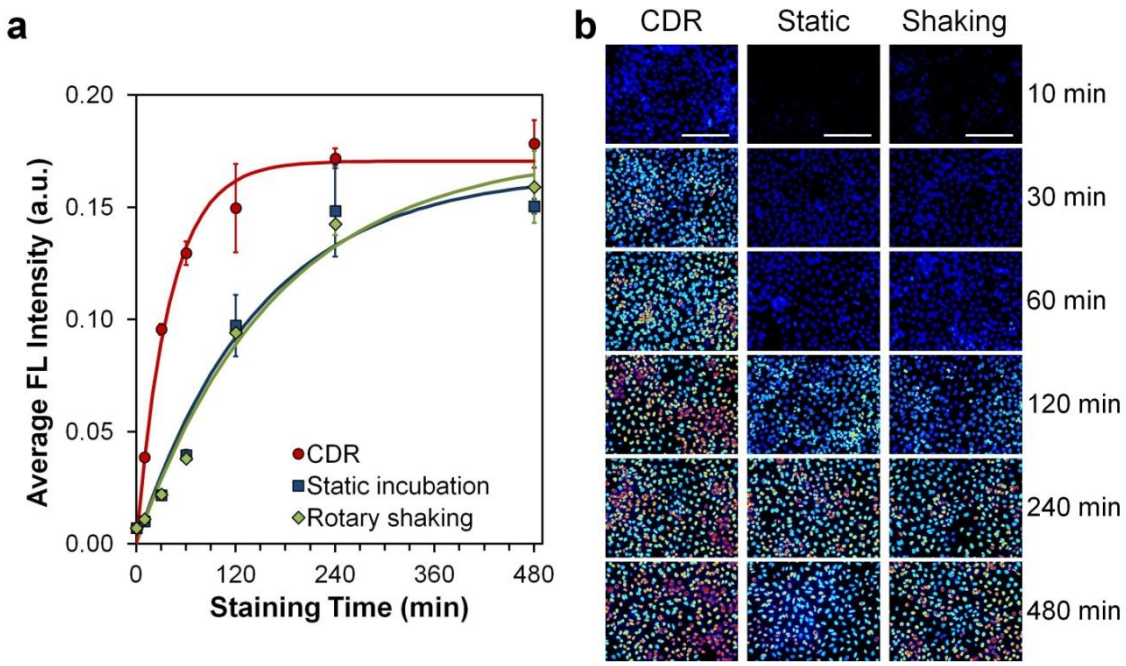


**Figure 2.2.7. Effect of mass transfer on immunofluorescence staining kinetics with QDot-antibody bioconjugates.** HeLa cells grown in glass-bottom 6-well plates were fixed and stained with anti-Lamin A QDot-1'Ab probes via cyclic draining-replenishing (CDR), static incubation, or rotary shaking procedure. **(a)** Quantitative analysis of staining intensity with respect to incubation time yielded substantially slower diffusion-limited target labeling under static incubation (t½ = 102 min) and rotary shaking (t½ = 117 min) conditions, whereas an overall 4-times faster staining kinetics was achieved with CDR procedure (t½ = 28 min). Average staining intensities with respect to incubation time were fitted by exponential curves. Error bars represent one standard deviation of an average Lamin A staining intensity from four different fields of view. **(b)** This analysis was fully corroborated by the qualitative evaluation of normalized cell staining images (intensity color-coded with a heat map) obtained after incubating cells with QDot-1'Ab probes for 10-480 min. CDR produced a clearly detectable target labeling within the first several minutes of incubation, whereas it took up to 1 hour to achieve comparable staining level with conventional methods. Scale bar, 250 μm.

## 2.2.3 Background-free monitoring of staining evolution

Strong background fluorescence originating from the bulk high-concentration probe solution often interferes with in situ IF staining applications, requiring specimen washing prior to imaging and, thus, precluding real-time monitoring of staining evolution and increasing assay time. Reducing the probe concentration might be beneficial in this situation (which also helps to reduce costs of expensive biological reagents), but it would necessarily slow-down staining kinetics under diffusion-limited

conditions. In this regard, we hypothesized that elimination of probe diffusion limitation should yield comparable staining intensity with lower probe concentration due to improved assay kinetics.

To test this hypothesis we first compared staining intensities obtained after 1-h CDR with 0.3 nM, 0.9 nM, and 1.5 nM QDot-Ab probes to a conventional 1-h staining with 7 nM QDots. Qualitative evaluation of representative normalized images (**Fig. 2.2.8a-d**) and quantitative analysis of average staining intensities (**Fig. 2.2.8e**) confirmed that similar labeling intensity could be achieved after 1-h incubation with either 7 nM probes under rotary shaking or 0.9 nM probes under CDR. Therefore, the CDR methodology enabled an approximately 8-fold reduction in probe concentration without any loss in sensitivity.

We then tested whether such reduction of probe concentration below 1 nM was sufficient in order to eliminate the undesirable fluorescence background. Fixed HeLa cells were incubated with QDot-Ab probes at 7 nM under rotary shaking or 0.9 nM under CDR and imaged prior to and after washing (**Fig. 2.2.8f**). As expected, 7 nM QDot solution produced a strong fluorescence background, which masked specific target labeling and had to be removed by washing. In contrast, 0.9 nM QDots featured nearly no background, while producing comparable nuclear membrane staining via CDR. Thus, we confirmed that CDR could be used for background-free monitoring of staining evolution and, potentially, could be applied for efficient capture of low-abundance targets.

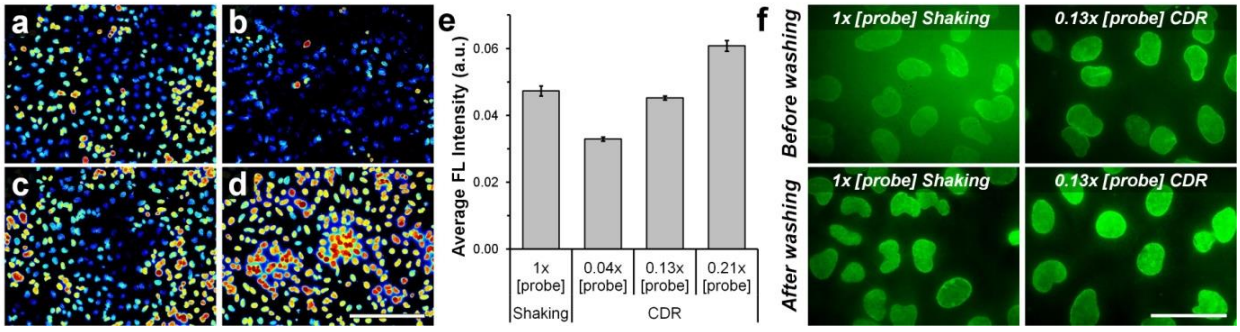

**Figure 2.2.8. Background-free immunofluorescence staining via CDR. (a-d)** Representative fluorescence intensity maps obtained after a 1-hour incubation with **(a)** 7 nM QDot-1'Ab (1x [probe]) under rotary shaking and **(b)** 0.3 nM (0.04x [probe]), **(c)** 0.9 nM (0.13x [probe]), and **(d)** 1.5 nM (0.21x [probe]) QDot-1'Ab using CDR procedure. Images were normalized and color-coded with a heat map. Scale bar, 250 μm. **(e)** Average fluorescence intensities of Lamin A staining achieved after a 1-hour incubation under rotary shaking with 1x [probe] and CDR with 0.04x, 0.13x, and 0.21x QDot-1'Ab concentration. Consistent with qualitative observations in **(a-d)**, quantitative analysis demonstrated that comparable staining could be obtained with ~8-times lower probe concentration via CDR methodology. Error bars represent one standard deviation of an average Lamin A staining intensity from four different fields of view. **(f)** A strong background fluorescence originating from the QDots in 1x [probe] bulk solution used for staining under rotary shaking required extensive specimen washing prior to imaging. At the same time, 0.13x [probe] solution employed with CDR methodology featured nearly no background, enabling real-time monitoring of staining evolution. Scale bar, 50 μm.

## 2.2.4 Enabling practical multicycle IF staining

A number of recently developed multicycle IF staining methods have captivated bioengineers and biologists because of their enormous potential in comprehensive in situ molecular analysis of single cells. Subsets of molecular targets in the same cells are stained with antibody-fluorescent reporter conjugates in multiple cycles with 2-10 targets in each cycle (depending on the availability of spectrally distinctive fluorophores). One such technology, recently reported by our group, is based on QDot probes that enable simultaneous 5-10 color labeling during each cycle (in comparison to organic dyes that are typically limited to 3 colors)[144]. Repeated staining of subgroups of antigens potentially allows examination of over 100 molecular targets in individual cells with the resolution of optical imaging. However, a drawback of this powerful technology for real-world research and clinical applications is the slow assay speed, as each staining cycle takes approximately 4 hours, largely due to the long diffusion-limited incubations including blocking, staining, destaining, and all the washing steps in between. When 10 cycles are performed at this speed, it takes 40 hours (whole week of work time) to complete the experiment. Therefore, enhancement of assay kinetics 5-10 times without the loss of sensitivity and capacity for quantitative analysis is highly desirable and will significantly enhance the practicality of virtually all the sequential cyclic staining technologies.

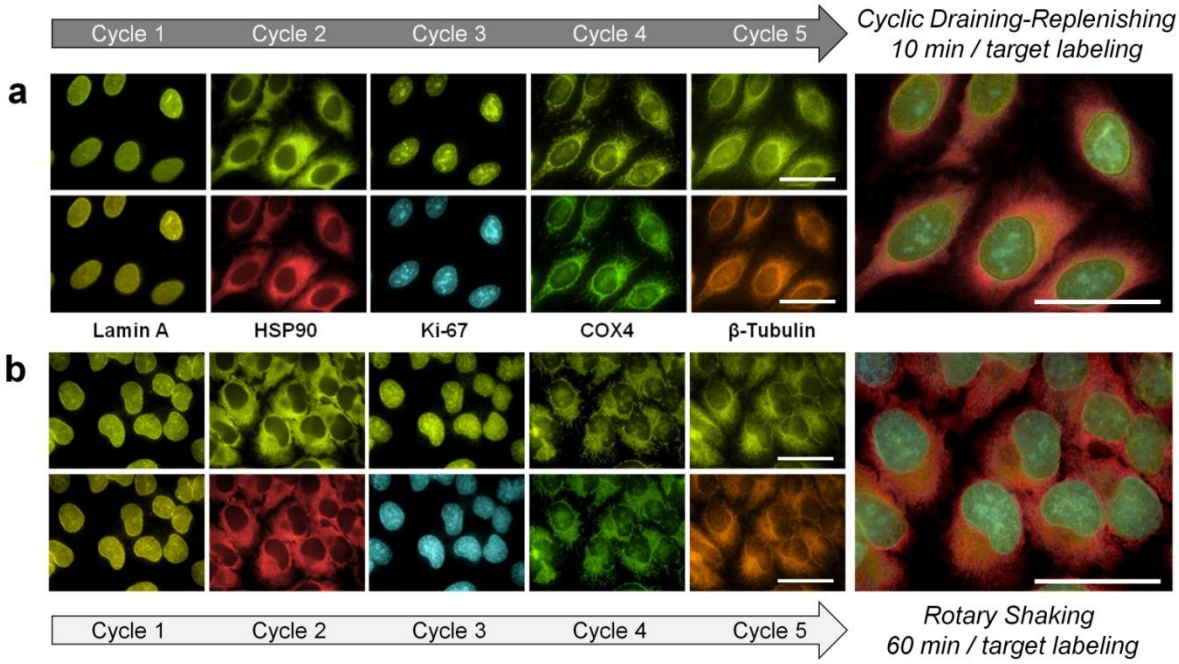


**Figure 2.2.9. Rapid multicycle immunofluorescence staining.** Five sequential cycles of single-color staining and imaging were performed on the same cell subpopulation for multiplexed detection of five molecular targets (Lamin A, HSP90, Ki-67, Cox-4 and β-tubulin) using self-assembled QDot-SpA-Ab probes. During each cycle, labeling was done via either a 10-minute CDR **(a)** or 1-hour rotary shaking **(b)** incubation. Both methods produced highly specific staining patterns with no carry-over fluorescence, build-up of background fluorescence, or cross-staining between cycles, yielding accurate 5-target imaging and analysis. However, CDR methodology enabled a substantial reduction in the overall assay time due to a dramatically improved labeling kinetics. Composite 5-target images were generated from false-colored, aligned, and cropped images of individual targets. Scale bar, 50 μm.

To demonstrate the concept, five intracellular targets (Lamin A, HSP90, Ki-67, Cox-4 and β-tubulin) were labeled with same-color QDot probes through 5 sequential staining / imaging / regeneration cycles. QDot-Ab bioconjugates were applied to cells either for 10 min via CDR or 1 h under conventional rotary shaking. Fluorescence microscopy with hyperspectral imaging was employed for imaging and quantitative analysis of staining intensity. In complete consistency with the rapid IF results shown above, shortened probe incubation through CDR produced accurate staining patterns (**Fig. 2.2.9a**) comparable to those produced via a regular multicycle procedure with 1-h QDot incubation steps (**Fig. 2.2.9b**). Importantly, quantitative analysis indicated that the fast CDR procedure yielded staining intensity levels very similar to those obtained with reference static incubation (**Fig. 2.2.10**), producing accurate molecular expression profile at a substantially reduced assay time.

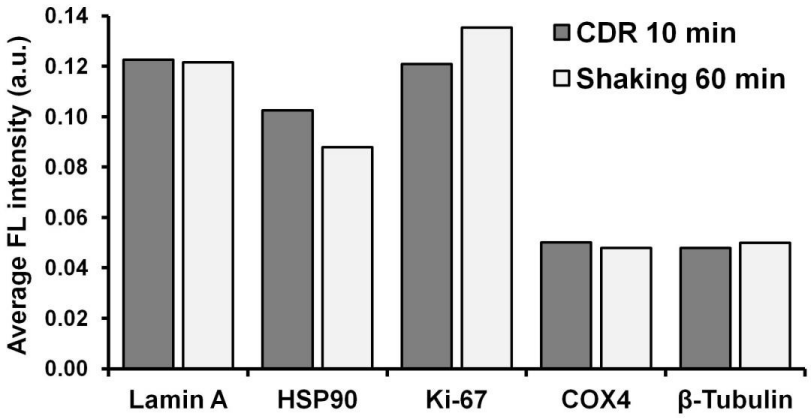


**Figure 2.2.10. Quantitative analysis of target staining intensity in multicycle immunofluorescence procedure.** Same subpopulation of cells grown in glass-bottom 6-well plates was exposed to 5 cycles of single-plex staining/imaging/de-staining with self-assembled QDot-SpA-Ab probes for multiplexed detection of five molecular targets (Lamin A, HSP90, Ki-67, Cox-4 and β-tubulin) in a sequential manner. Each target was labeled by either a cyclic draining-replenishing (CDR) methodology for 10 minutes or incubation under rotary shaking for 60 minutes. The average fluorescence intensity throughout all regions of interest within a single low-magnification image (containing at least 400 cells within a field of view) was recorded. Independent of the method used, all targets were reliably stained, showing correct relative staining intensity. However, with CDR methodology comparable staining intensities were achieved 6 times faster in comparison to diffusion-limited incubation under rotary shaking, thus offering a simple strategy for dramatically reducing the duration of multicycle immunofluorescence procedures.

## 2.2.5. Summary

On-surface assays have become an indispensable tool for numerous bio-analytical and imaging applications, with nanoparticle probes expanding assay capabilities and enabling novel assay formats. However, most of these techniques are strictly limited by the slow probe diffusion from the bulk solution to the surface, which has proven virtually inevitable with conventional assay setups. Diffusion limitation is highly detrimental to advanced multi-step procedures, such as powerful multi-cycle IF techniques for single-cell molecular profiling,[145] and is undesirable in single-step procedures when the assay time is of essence, such as in intraoperative and infectious disease diagnostics[146-148].

The cyclic draining-replenishing (CDR) technology reported here completely eliminates the chronic and fundamental problem of diffusion limitation, achieving efficient molecular mixing at the surface and "erasing" the effect of the probe size in a simple and affordable setup easily adaptable by a wide range of biomedical laboratories. Through proof-of-concept studies, we have demonstrated that ELISA with ~100

nm poly-HRP nanoprobes could be performed in a much faster reaction-limited regime, and IF cell staining with QDots could be achieved in under 10 min incubation with CDR. Further, a substantial enhancement in assay kinetics has rendered multi-step and multi-cycle high-content molecular analysis technologies practically useful for the first time.

We anticipate CDR technology to be incorporated within existing on-surface assays and become an enabling component of novel ultra-rapid technologies for high-content scientific analysis and fast clinical diagnostics. The concept of CDR could also inspire a broad spectrum of applications in basic and clinical research (e.g., cell transfection and fast detection of time-sensitive diseases, such as infectious and cardiovascular diseases) and industrial fields (e.g., on-surface catalysis)[149]. Finally, elimination of at-surface molecular depletion might prove instrumental for applications requiring efficient capture of low-abundance targets onto a surface, which might take hours or days under mass transfer-limited condition.

# CHAPTER 3: *IN VIVO* TOOLS FOR DISEASE IMAGING

## 3.1 CONJUGATED POLYMERS FOR PHOTOACOUSTIC IMAGING

### 3.1.1 Comparison of conjugated polymer with gold nanorods as photoacoustic imaging contrast agents

To illustrate the concept of PA imaging using conjugated polymers, we synthesized a NIR-absorbing conjugated polymer, poly[9,9-bis(4-(2-ethylhexyl) phenyl) fluorene-alt-co-6,7-bis(4-(hexyloxy)phenyl)-4,9-di(thiophen-2-yl) thiadiazoloquinoxaline] (PFTTQ) **(Fig. 3.1.1a)**, and encapsulated it into nanoparticles using a standard emulsion process.

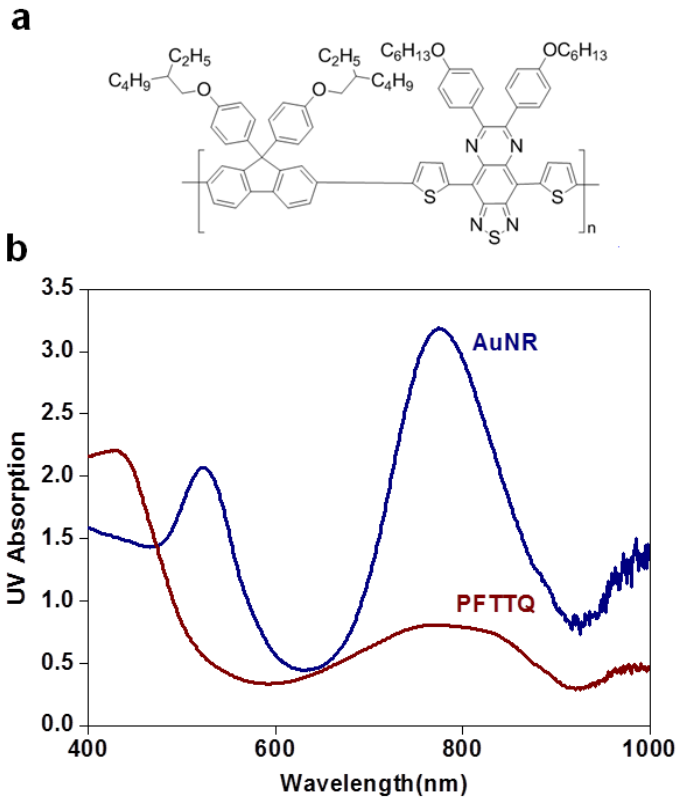

**Figure 3.1.1. Conjugated polymer as a new photoacoustic imaging contrast agent. (a)** Chemical structure of PFTTQ. **(b)** UV absorption measurements of AuNRs and PFTTQ nanoparticles of the same weight concentration.

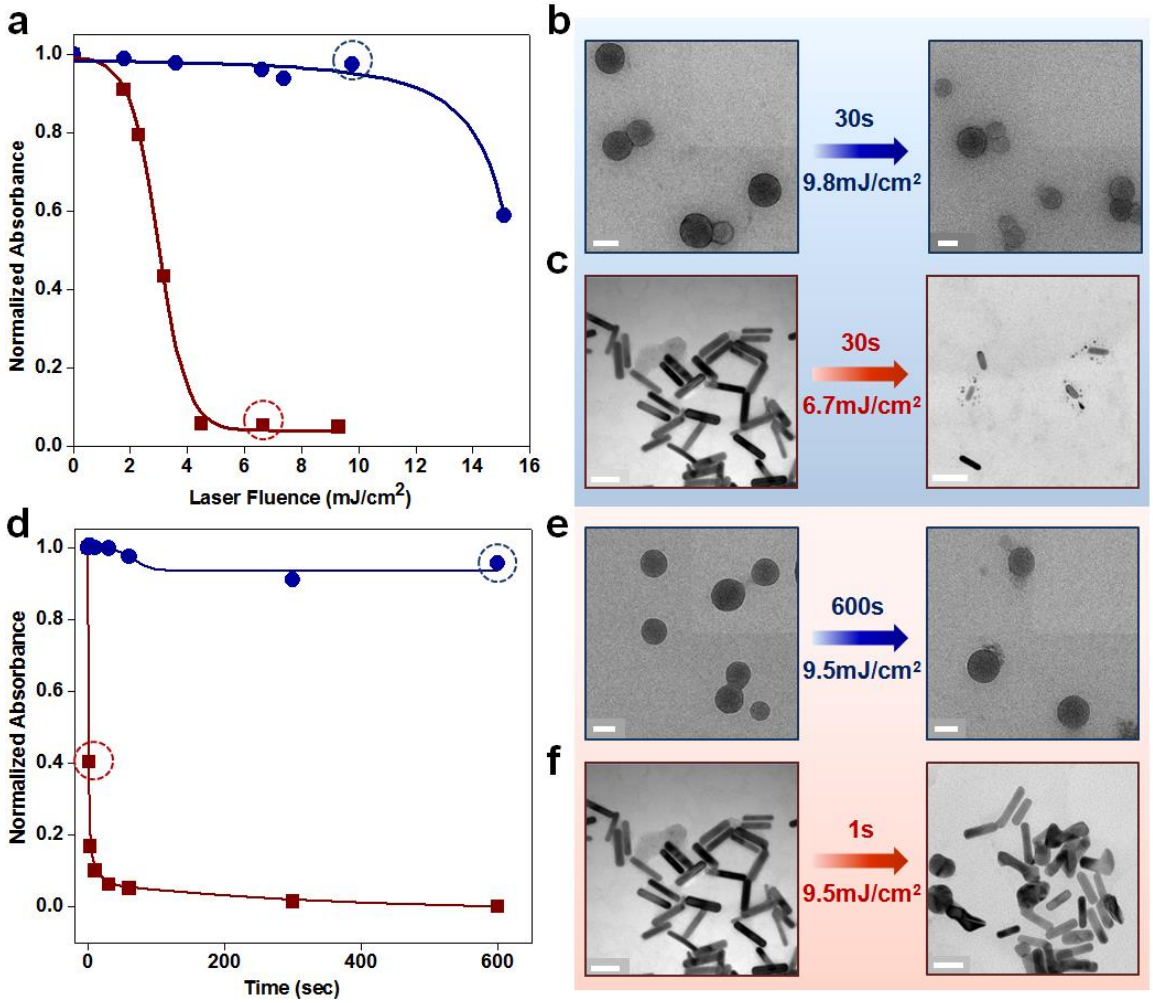


**Figure 3.1.2. Photostability comparison of PFTTQ nanoparticles and AuNRs.** PFTTQ nanoparticles and AuNRs are treated by laser for 30 seconds with increasing laser intensity from 2 to 15 mJ/cm$^2$. UV absorption measurements **(a)**, and TEM imaging of PFTTQ **(b)** and AuNRs **(c)** before and after laser irradiation both show superior photostability of the conjugated polymer. Significant amount of AuNRs are found fragmented and shortened. PFTTQ nanoparticles and AuNRs are also treated under the same laser intensity (9.5 mJ/cm$^2$) for varying durations (1 to 600s). UV absorption measurements **(d)** and TEM imaging **(e and f)** of nanoparticles before and after laser irradiation again show improved stability for PFTTQ over AuNRs (many fused together).

Transmission electron microscopy (TEM) and UV absorption measurements of the as-synthesized nanoparticles show a mean diameter of 70 nm, and a broad and strong absorption peak from 700 to 900 nm (note that possible absorption beyond 900 nm are not detected due to limited UV detector spectral range) **(Fig. 3.1.1b)**. Compared to the most common PA imaging contrast agent, gold nanorods (AuNRs) with absorption at the longitudinal surface plasmon peak (overall sizes are also similar), PFTTQ's absorptivity at 800 nm is approximately a quarter of that of AuNRs of the same weight.

This is impressive for an organic material considering AuNRs offer orders of magnitude higher molar extinction efficiency over dyes and quantum dots, and the highest absorptivity per unit volume compared to other gold nanostructures (such as spherical particles and nanoshells). More remarkably, the PFTTQ nanoparticles are significantly more stable against photo-induced degradation compared to AuNRs, the most popular PA imaging contrast agent. As shown in **Figure 3.1.2a**, when PFTTQ nanoparticles and AuNRs are treated by laser for 30 seconds with increasing laser intensity from 2 to 15 mJ/cm$^2$ (fixed time, varying laser intensity), AuNRs quickly degrade and lose their characteristic NIR absorption profile; whereas PFTTQ nanoparticles remain intact for laser intensities up to ~10 mJ/cm$^2$. TEM imaging before and after laser irradiation shows that the PFTTQ nanoparticles are largely intact, but the AuNRs are shortened and fragmented **(Fig. 3.1.2b and c)**. Similarly, under the same laser irradiation (fixed laser intensity at 9.5 mJ/cm$^2$, varying exposure time), AuNRs are degraded in less than a second, but the conjugated polymer nanoparticles are stable even after 10-minute exposure **(Fig. 3.1.2d-f)**. Photoacoustic imaging of PFTTQ nanoparticle and AuNR suspensions show similar results as the UV absorption measurements (data not shown). Photoacoustic signal from AuNRs quickly drops when illuminated with pulsed laser of high intensity or extended periods.

## 3.1.2 Summary

The improved photostability of CP nanoparticles over AuNRs is perhaps a little surprising because inorganic nanomaterials are generally perceived to be more stable contrast agents against laser irradiation than organic compounds. A closer look at the two types of nanoparticles indicates that the photostability of CPs are highly dependent upon their molecular structures as well as the encapsulation

matrix and packaging. Fortunately, due to the fast advances in organic electronics, critical parameters influencing the stability of CPs have been mapped out, which can be used as a guideline for PA contrast agent synthesis. In contrast, AuNRs can melt into spherical particles of similar volumes or even fragment into smaller particles under pulsed laser irradiation. High-resolution TEM also reveals that different from thermal melting, which starts from the nanomaterial surface, the photothermal melting process starts with the formation of defects inside AuNRs. This photostability comparison renders CP nanoparticles a very promising probe for bioimaging utilizing high-intensity or extended laser illumination such as PA imaging and multiphoton microscopy, and enables the possibility for tracking complex biomolecular events in real-time.

## 3.2 MAGNETO-OPTICAL NANOPARTICLES FOR CYCLIC MAGNETOMOTIVE PHOTOACOUSTIC IMAGING

Here, we report a comprehensive solution to these requirements by developing a new class of compact, uniform, NIR-responsive, and magnetic contrast agent composed of a core magnetic nanoparticle (MNP) and a shell of conducting polymers (PPy, **Fig. 3.2.1a**). In parallel, to accelerate potential clinical translation, we developed the next generation of mmPA imaging by introducing multicycle magnetic motion (**Fig. 3.2.1b**) and coupling photoacoustic imaging with ultrasound speckle tracking (USST). Previously, contrast enhancement based on the absolute amplitude of spatial displacement has been explored by us (first generation mmPA) and others, but these techniques based on single-cycle displacement magnitude thresholding are intrinsically sensitive to physiological motion[150]. Cyclic mmPA (cmmPA), based on signal time coherence, is significantly more robust in distinguishing true magnetomotion from physiological motion artifacts. More importantly, besides speckle tracking performed with photoacoustic images, we show that estimation of magnetically-induced displacement in the new mmPA technology can be obtained with a series of US images at kHz frame rates, hundreds of times faster than photoacoustic imaging's frame rate determined by the current laser repetition rate (10s Hz). These advances enable the first demonstration of mmPA *in vivo*.

### 3.2.1 MNP-PPy core-shell nanoparticle preparation and the mechanism of cyclic mmPA

A number of attempts have been reported to make MNP-PPy core-shell nanoparticles due to their attractive properties and potential impact on bio-sensing, -imaging, and photothermal therapy. Relatively large particles (sub-micron) coated with conjugated polymers have been made with uniform size and shell thickness, and clear observation of the core-shell structures[151, 152].

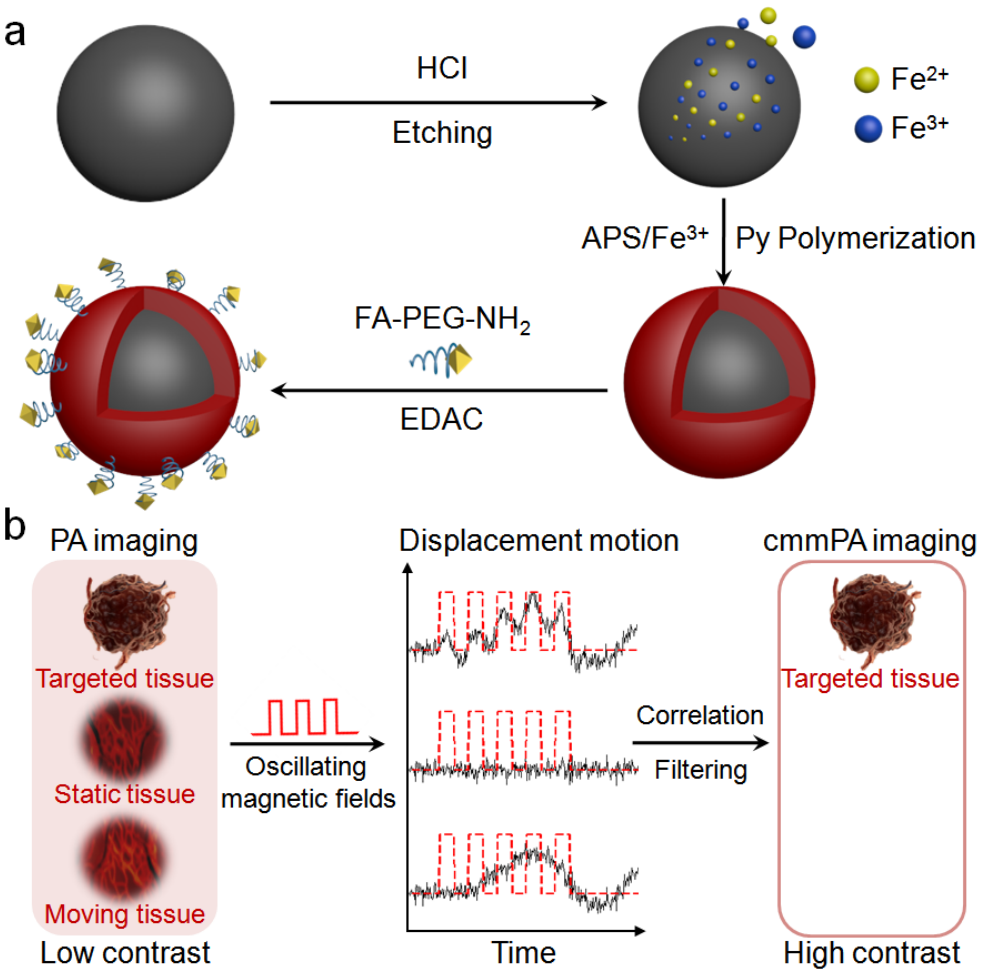


**Figure 3.2.1. Schematic of MNP-PPy core-shell nanoparticle fabrication and the mechanism of cyclic mmPA in imaging contrast enhancement. (a)** Key steps involved in hybrid nanoparticle synthesis: $Fe^{2+}/Fe^{3+}$ generation though acid etching of monodisperse MNPs, PPy shell formation through in the presence of $Fe^{3+}$ and APS, and conjugation of FA-PEG-$NH_2$ to nanoparticle surface. **(b)** Schematic of tumor detection *via* cyclic mmPA imaging. Contrast enhancement of tumor/background by suppressing both signals from static tissues and regions with random motions from moving tissues not related to the frequency of oscillating magnetic fields while identifying specific tumor signals from targeted tissues coherently responsive to cyclic magnetic motions.

Unfortunately, these particles are too big for efficient receptor-mediated endocytosis (optimal size ~50 nm) and *in vivo* vascular extravasation, particularly for hypopermeable disease sites[153, 154]. Compact MNP-PPy composite nanoparticles with uniform size, good colloidal stability, and balanced magnetization and NIR absorption are difficult to achieve simultaneously. Dr. Liu and coworkers recently demonstrated the synthesis of uniform core-shell iron oxide@PPy using MNP clusters as the core[155]; whereas the

majority of previous reports using a single magnetic nanoparticle core yield MNP-PPy hybrid particles with poor size distribution and indirect proof of the core-shell internal structure[156-161]. This is not too surprising since polymer shell formation on a preformed nanoparticle core made from different materials (seeded polymerization) is in direct competition with homogeneous nucleation and growth of the shell material. We solved this problem by promoting Py polymerization on nanoparticle surfaces and suppressing formation of pure PPy nanoparticles.

**Figure 3.2.1a** schematically illustrates the key steps in the synthesis of MNP-PPy core-shell nanoparticles. Highly monodisperse oleic acid-coated MNPs of 40-50 nm diameter are first solubilized into aqueous solution using an amphiphilic polymer and further stabilized with sodium dodecyl sulfate (SDS). The pH of the solution is adjusted to 2-3 using HCl to slowly etch the MNPs to generate iron ions, which have been shown to catalyze conjugated polymer polymerization[162]. Pyrrole and pyrrole-3-carboxylic acid (Py-COOH, to improve solubility and provide reactive sites) are added to the MNP solution and oxidized into a shell of polypyrrole on the MNP surface in the presence of an oxidizing reagent $(NH_4)_2S_2O_8$ (APS) (**Fig. 3.2.2a**).

The resulting core-shell magneto-optical nanoparticles are purified with magnetic separation (to remove free PPy nanoparticles), pegylated to reduce nonspecific binding, and functionalized with a targeting ligand. In this work, folic acid (FA) is used as a model to recognize a human cervical cancer cell line, HeLa.

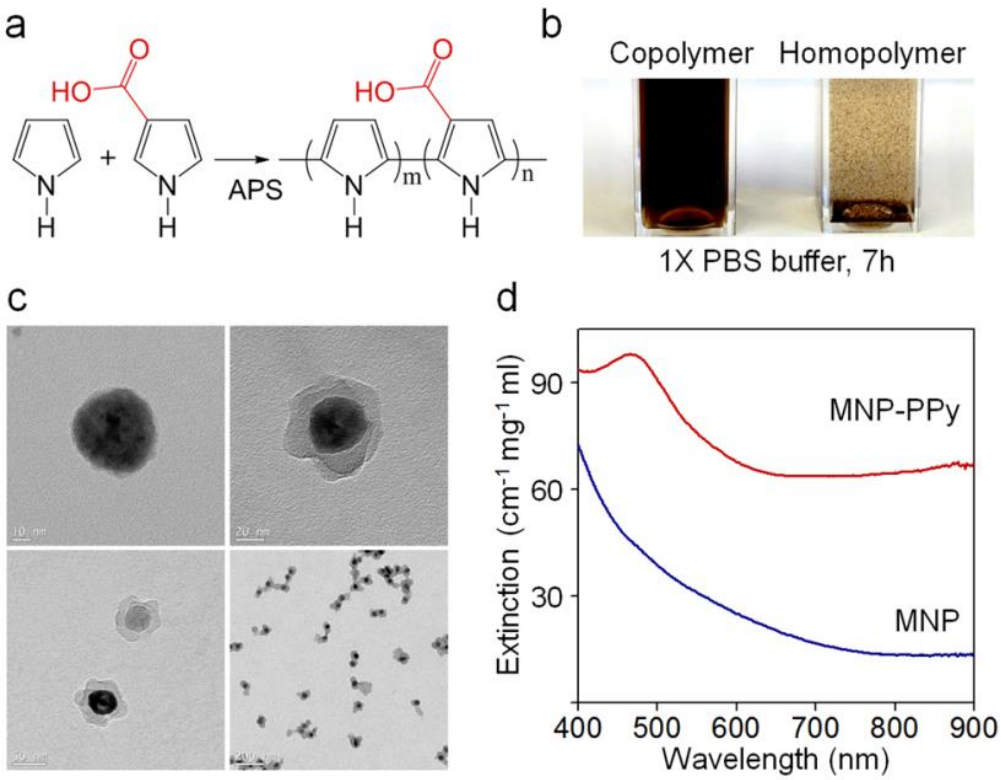


**Figure 3.2.2. Preparation and characterization of the MNP-PPy hybrid nanoparticles. (a)** Construction of nanoparticle shells *via* copolymerization of Py and Py-COOH monomers catalyzed by APS. **(b)** Photograph of MNP-PPy hybrid nanoparticles dispersed in 1X phosphate buffered saline (PBS) solution after 7 h (Left: copolymerization of Py and Py-COOH with 8:1 molar ratio; Right: homopolymerization of Py). **(c)** TEM images of the MNPs (47.5 ± 7.0 nm) and typical MNP-PPy core-shell nanoparticles (core: 35.5 ± 8.6 nm; shell: 15-25 nm) at low and high magnification. **(d)** Absorption spectra of MNP-PPy hybrid nanoparticles (red) and MNPs (blue) after being isolated from their respective solutions.

Transmission electron microscopy (TEM) measurements clearly show the core-shell structure of MNP-PPy nanoparticles (**Fig. 3.2.2c**). The PPy nanoshells show petal-like shell structures with a thickness ranging between 0-20 nm. Although the PPy shell is not perfectly spherical and smooth, it does not affect its intended use, an efficient NIR light absorber. In comparison with the original MNP, the size of the iron oxide core reduces from 47.5 ± 7.0 nm to 35.5 ± 8.6 nm, as a result of acid etching. Dynamic light scattering (DLS) measurements show that the hydrodynamic diameter of the core-shell nanoparticles is 51.1 ± 7.5 nm, an excellent size range for efficient endocytosis and deep tissue penetration. Moreover, DLS also confirmed their narrow size distribution with a polydispersity index of 0.18 ± 0.01. Copolymerization of Py and Py-COOH improves the solubility and colloidal stability of the resulting

nanoparticles. As shown in **Figure 3.2.2b**, MNP-PPy made from polymerization of pure Py form aggregates in phosphate buffered saline (PBS) and precipitates out of solution in a few hours; whereas MNP-PPy made from copolymerization of Py and Py-COOH remains stable. The PPy nanoshell formation is further confirmed by the absorption spectrum. Strong light extinction was observed around 470 nm, indicating formation of the polymer shell. Compared to the typical bipolaron absorption peak of pure PPy centered at 480 nm, the slight spectral blue-shift is likely due to the incorporation of Py-COOH (11% by molar ratio) in the copolymer. Compared with the original MNPs, the core-shell nanoparticles show a broad absorption profile in the NIR region (**Fig. 3.2.2d**), highly desirable for absorption-based applications such as photoacoustic imaging and photothermal therapy. At equal weight concentration, the extinction profile of MNP-PPy is 4.8 times stronger than that of MNP at 800nm. Because light extinction comprises absorption (which really matters for PA) and scattering, we further measured the photoacoustic signal strength, which is linearly related to the nanoparticles' wavelength-dependent absorption profile. At 800 nm, the photoacoustic signal generated by the MNP-PPy nanoparticles is 10 times stronger than that generated by MNP. This larger difference could be attributed to absorption's dominance of the MNP-PPy overall extinction.

Under the current reaction conditions, both $Fe^{3+}$ ions leached from the MNP surface and the added APS can serve as the oxidant for Py polymerization. In the absence of an anionic surfactant, SDS, APS is significantly more effective in PPy formation, measured by absorbance at 800 nm (**Fig. 3.2.3a**). This is expected since APS is of higher oxidation potential than $Fe^{3+}$.[163] Addition of MNPs to the reaction only slightly increases the rates for both APS and Fe3+ oxidized polymerization (**Fig. 3.2.3b**). Interestingly, however, addition of SDS completely reverses the efficiencies of the two reactions (**Fig. 3.2.3c**). The reaction yield of $Fe^{3+}$ oxidized polymerization increases by 40 times (10 hour reaction time), and that for APS-based polymerization decreases by 3 times. These reaction rate changes are in agreement with previous research and have been attributed to electrostatic attraction between negatively charged SDS and $Fe^{3+}$ and the increased solution viscosity[164, 165]. Based on these observations, synthesis of MNP-PPy core-shell particles can be rationally designed. For example, if bulk $Fe^{3+}$ is used as the oxidant, polymerization of PPy would occur in solution regardless of the presence of MNPs (**Fig. 3.2.3d**). Using

APS as the oxidant in the presence of SDS, in contrast, would slow formation of solid PPy nanoparticles (homogeneous nucleation) and their aggregates. At the same time, because the reaction is conducted in acidic conditions (pH=2-3) where Fe ions are slowly released from MNP, PPy oxidation on the MNP surface by $Fe^{3+}$ is promoted by the MNP surface (reduced $Fe^{3+}$ can be regenerated by bulk APS). It is worth mentioning that the pH was optimized to 2-3 because more acidic conditions dissolve MNPs too fast, whereas higher pH dramatically reduces the polymerization rate.

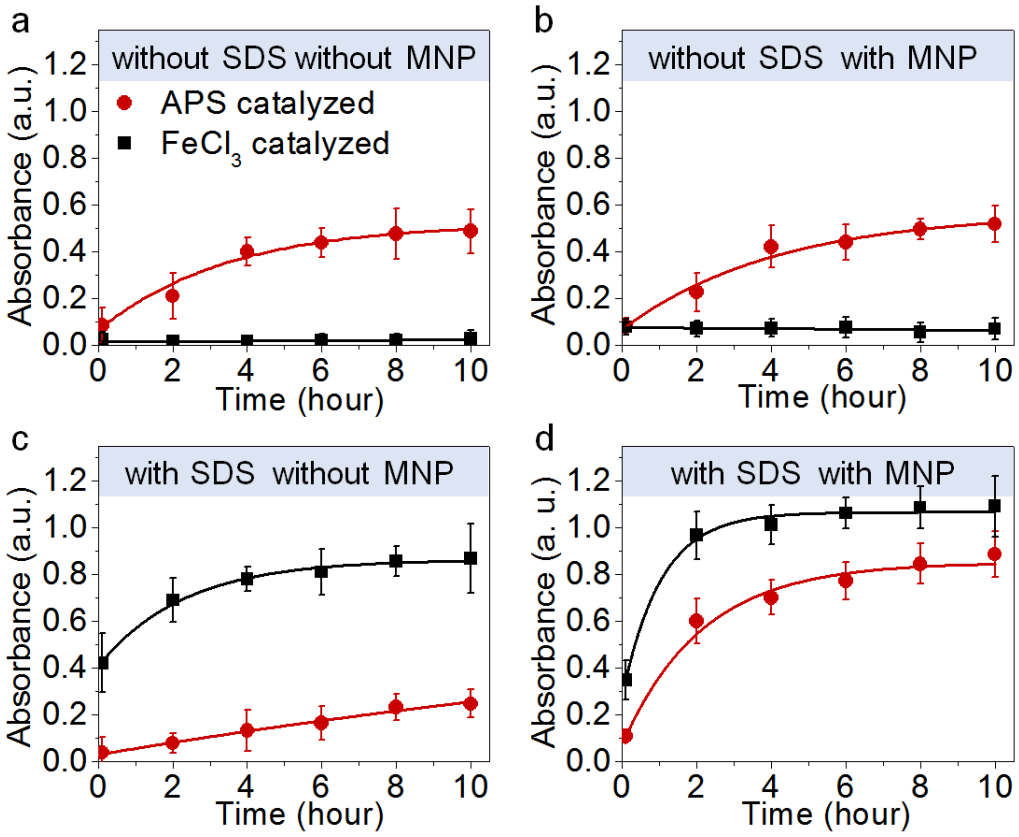


**Figure 3.2.3. Kinetics of Py polymerization for eight reaction conditions.** Eight individual vials containing the same amount of water (pH 2.5, 4.5 ml), Py monomers (20 mM, 450 µl), sodium dodecyl sulfate (SDS; 120 mM, 300 µl), MNPs (70 nM, 60 µl) or equally the same amount of water (control groups) prepared for polymerization. APS (2 mM, 4.5 mL) or $FeCl_3$ (4 mM, 4.5 ml) catalyzed the four vial reaction at the same time. Polymerization yield (PPy absorbance at 800 nm) is plotted as a function of time for eight conditions: **(a)** without SDS, without MNP; **(b)** without SDS, with MNP; **(c)** with SDS, without MNP; **(d)** with SDS, with MNP added inside initial prepared solutions catalyzed by APS (red) or $FeCl_3$ (black), respectively. Concentration of $FeCl_3$ is twice as much as that of APS due to APS twofold higher valence than $FeCl_3$. Error bars represent standard deviations of three separate measurements.

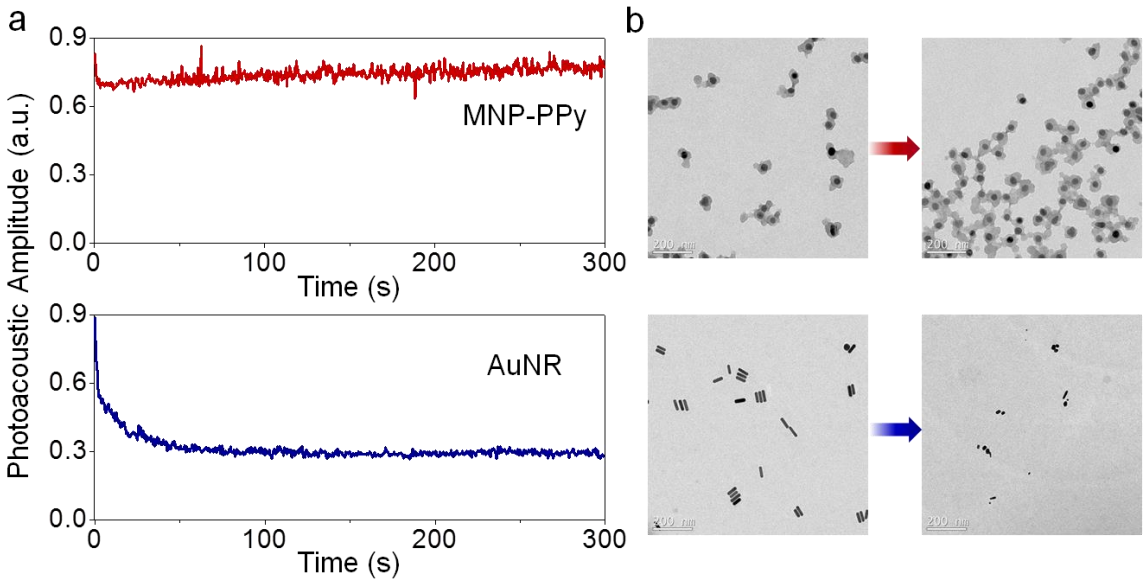


**Figure 3.2.4. Photothermal stability of MNP-PPy hybrid nanoparticles compared with gold nanorods at the same mass (30 μg ml$^{-1}$) concentrations in polyvinyl alcohol (PVA) phantoms. (a)** Photoacoustic amplitudes of indicated nanoparticles in phantoms versus laser exposure time. The photoacoustic signal amplitude generated by gold nanorods drops from 0.89 to 0.27 after 300 s laser irradiation. **(b)** TEM images of typical MNP-PPy nanoparticles (top) and gold nanorods (bottom) before and after laser irradiation treatment for 300 s. A single laser pulse at 800 nm with a laser fluence of 11 mJ/cm$^2$ and a pulse repetition rate of 20 Hz was utilized for all experiments. The total pulse number for each sample is 6000 within 300 s. The fluence is calculated by divided the pulse energy by the illumination area.

### 3.2.2 Comparison of the photothermal stability between MNP-PPy nanoparticles with gold nanorods

To address the issue of agent stability under the intense laser irradiation required for photoacoustic imaging, we directly compared the photostability of MNP-PPy and gold nanorod, one of the best photoacoustic contrast agents commonly used as a benchmark.

At the same mass concentrations, the amplitudes of photoacoustic signals generated with MNP-PPy and gold nanorods are similar. The photostability of MNP-PPy nanoparticles, however, is significantly better. When the MNP-PPy nanoparticles and gold nanorods are treated with a low-intensity pulsed laser (5 mJ/cm$^2$, pulse repetition rate of 20 Hz), both MNP-PPy and gold nanorods remain intact during continuous illumination of 300 second, as indicated by the constant photoacoustic signals. When the laser

intensity increases to 11 mJ/cm$^2$, however, the photoacoustic signal of gold nanorods drops approximately 40% within just 2 seconds of illumination and continuously decays over time (**Fig. 3.2.4a**), because they quickly degrade and lose their characteristic NIR absorption. Under the same condition, the photoacoustic signal from MNP-PPy is still constant, revealing their superior photostability and suitability for long-term mmPA imaging. TEM imaging before and after laser irradiation confirmed these results. As shown in **Figure 3.2.4b**, the MNP-PPy nanoparticles are largely intact after exposure to laser irradiation, but the gold nanorods are shortened and fragmented.

The greatly improved photostability of PPy nanoparticles over gold nanorods is a little surprising since inorganic nanomaterials are generally perceived to be more photostable than organic compounds. For example, semiconductor quantum dots are thousands of times more stable than organic fluorophores[166]. However, gold nanorods are not the most thermodynamically stable structure, and can melt or fragment into spherical particles.

High-resolution TEM has revealed that unlike thermal melting, which starts from the nanomaterial surface, photothermal melting of gold nanorods starts from defect formation inside the nanorods.9 In contrast, the photostability of conjugated polymers can be optimized by varying their molecular structures, encapsulation matrix, and packaging[167]. This photostability comparison demonstrates MNP-PPy's outstanding potential for bioimaging utilizing high-intensity or extended laser illumination.

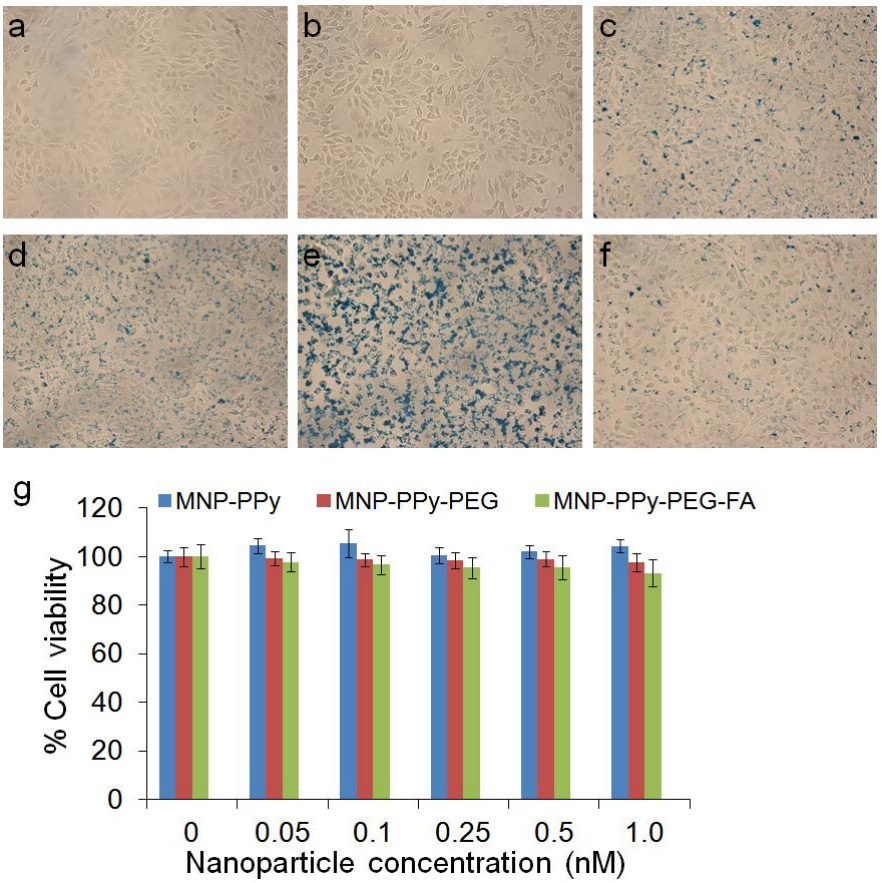


**Figure 3.2.5. Targeting specificity and cytotoxicity of hybrid nanoparticles.** Bright field micrographs of HeLa cells **(a)** with no treatment, and treated with **(b)** Prussian blue, **(c)** 0.5 nM MNP-PPy nanoparticles, **(d)** MNP-PPy-PEG nanoparticles, **(e)** MNP-PPy-PEG-FA nanoparticles, and **(f)** MNP-PPy-PEG-FA nanoparticles together with 1 mM free FA. **(c-f)** stained with Prussian blue. **(g)** Dose-dependent cytotoxicity of MNP-PPy, MNP-PPy-PEG, and MNP-PPy-PEG-FA nanoparticles in HeLa cells plotted against the control groups with no treatment. In the concentration range probed between 0 and 1.0 nM, the three types of nanoparticles do not show significant cytotoxicity. Error bars represent standard deviations of three separate measurements.

### 3.2.3 Cancer cell targeting specificity and cytotoxicity of MNP-PPy hybrid nanoparticles

For cell labeling, the MNP-PPy nanoparticles are further pegylated and conjugated with FA as a model cell targeting ligand. HeLa cells are treated with the targeted MNP-PPy at a concentration of 0.5 nM for 2h, in comparison with non-targeted MNP-PPy and MNP-PPy-PEG. Using Prussian blue staining (formation of ferricyanide), nanoparticle uptake can be directly visualized and qualitatively analyzed.

**Figure 3.2.5** shows pronounced differences between the targeted nanoparticles (**Fig. 3.2.5e**) and the control groups (no treatment, treatment with MNP-PPy nanoparticles, or MNP-PPy-PEG nanoparticles, **Fig. 3.2.5a-d**). To further confirm that targeting was achieved through FA targeting ligands, a competition assay was conducted by co-incubation of the targeted nanoparticles with free folic acid molecules. As shown in **Figure 3.2.5f**, Prussian blue staining is reduced to approximately the same level of the pegylated nanoparticles (**Fig. 3.2.5d**), demonstrating targeting specificity.

Before moving to tumor cell detection with mmPA, a remaining characterization experiment for the MNP-PPy hybrid nanoparticles examines cytotoxicity. As shown in **Figure 3.2.5g**, cell viability is not affected by the final FA-targeted MNP-PPy or the control particles (original unmodified MNP-PPy and pegylated MNP-PPy) in the concentration range from 0 to 1.0 nM. At 1.0 nM, twice as high as the particle concentration used in cell labeling, cell viability only decreases by 7% for the FA-targeted MNP-PPy, which has the highest cell uptake.

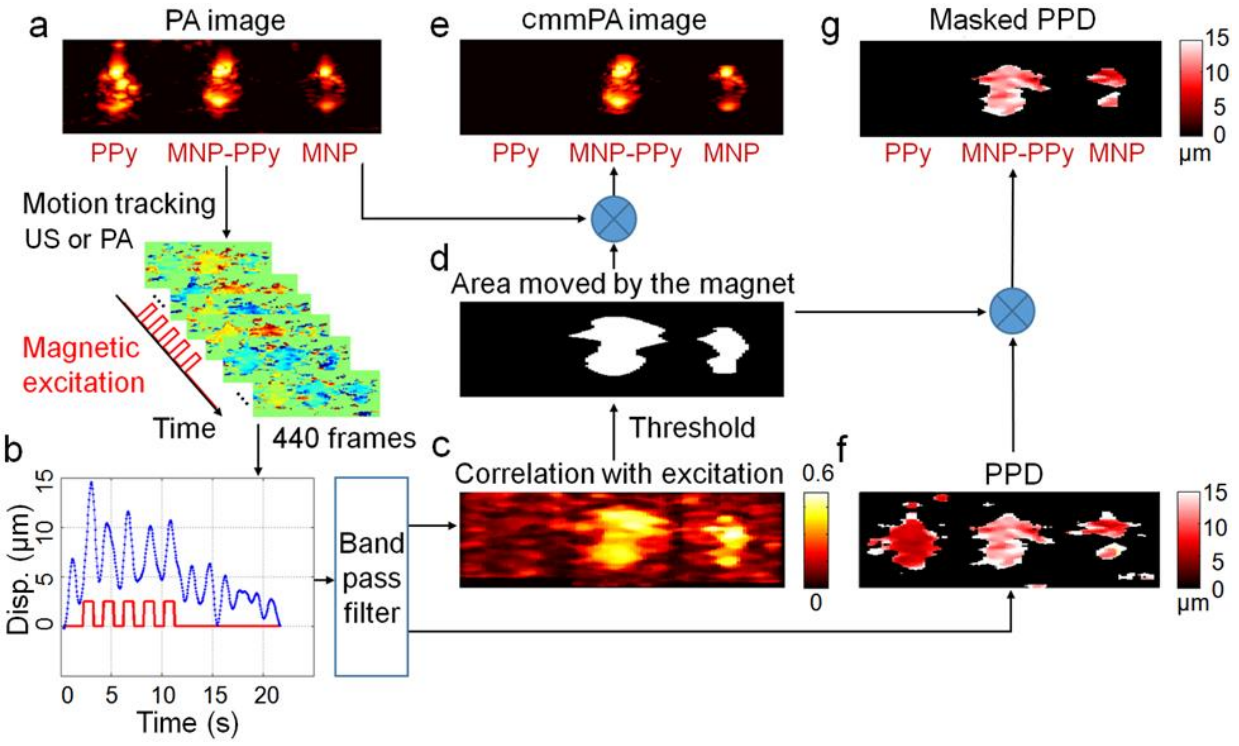

**Figure 3.2.6. Data processing of cyclic mmPA.** A PVA phantom with three 2 mm diameter inclusions, in which the one on the left contains PPy nanoparticles with absorption comparable to 5 nM MNP-PPy hybrid nanoparticles placed in the center of phantom, and the third inclusion on the right contains 5 nM MNPs. **(a)** A conventional photoacoustic image of this phantom presented on a logarithmic scale over a 40 dB display range. **(b)** A representative displacement of MNP-PPy inclusion during 5-cycle square wave magnetic excitation with a frequency of 0.5 Hz. **(c)** Correlation with excitation map (CEM) utilized to produce photoacoustic image background suppression with a threshold of 0.5. **(d)** Mask produced by thresholding the CEM with 0.5, and used to identify MNPs. **(e)** The cmmPA images produced by multiplying the threshold mask from **(a)**, in which the PPy inclusion is almost completely suppressed. **(f)** Peak to peak displacement images before and **(g)** after background suppression with the threshold mask.

### 3.2.4 Evaluation of cmmPA for cancer cell detection in *ex vivo* condition

Next, we evaluated the design and performance of the new generation of mmPA technology featuring two major innovations for *in vivo* applications. **Figure 3.2.1b** demonstrates the concept of the first innovation, multicycle magnetomotion. Under simplified imaging conditions where specific signals from contrast agents are buried by static background signals, single-cycle magnetic-induced physical movements of the contrast agent (or cells labeled with the contrast agents) is sufficient to retrieve the moving signal from the contrast agent and completely reject the background static signals (1st generation mmPA). For *in vivo* imaging, however, the motion sources can be complex, including magnetic motion as well as physiological movements such as cardiac and respiratory motions (background motions). To mitigate the interference from background motions, previous *in vivo* studies have taken advantage of the “grace period” of breathing cycles using single element scanning to form a 2D image. Hence, continuous measurements cannot be performed since each sequence has to be triggered on every breathing cycle, limiting the frame rate to less than 1 line/s.

In addition, thresholding of displacement magnitudes also has major limitations, because the amplitudes of background motion vary dramatically and a consistent threshold is difficult to find. For second generation mmPA, we acquire 2-D (3-D) photoacoustic images in a single laser shot using a conventional 1-D (2-D) ultrasound array and a cyclic excitation method (thus dubbed cmmPA) to separate magnetomotive displacements from background motions. As a result, the threshold is independent of displacement amplitude and only depends on the time coherence of the displacements. Thus, both the amplitude and phase of displacements are taken into account. This cmmPA technology enables real-time

mmPA *in vivo* even with significant physiological motions. Magnetically-induced displacements with frequency ranging from 1 to 50 Hz and velocities up to 1 cm/s can be used to resolve molecular events with enhanced time resolution.

To evaluate cmmPA, three cylindrical inclusions, PPy, MNP-PPy, and MNP, were embedded in a polyvinyl alcohol (PVA) phantom. PPy NPs with absorption comparable to 5 nM MNP-PPy nanoparticles serve as the negative control for magnetic displacement; and MNPs (5 nM) serve as the negative control for NIR absorbance. An electromagnet (0.7-Tesla at the source, and approximately 0.2 Tesla at the inclusion region) outputs pulsed magnetic fields with tunable frequencies. **Figure 3.2.6a** shows the cross-sectional photoacoustic image on a dB scale. Illuminated with a pulsed laser at 800 nm, the MNP-PPy and PPy inclusions show similar photoacoustic signal intensity, whereas the photoacoustic signal of the MNP inclusion is approximately one order of magnitude lower because of the low absorbance of MNP in the NIR spectrum.

A series of photoacoustic images (440 frames over 22 seconds) were recorded during which 5 cycles of 0.5-Hz magnetic movements were applied (**Fig. 3.2.6b**). The photoacoustic images were beamformed using a simple delay-and-sum approach and the resultant analytical signals were filtered with a bandpass filter ([0.35-1.83 Hz]) in the time direction. The motion of every pixel in the photoacoustic image is tracked using a speckle tracking algorithm[168, 169], and the corresponding displacement curve is cross-correlated with a bipolar derivative of the magnetic shaking signal (**Fig. 3.2.6c**). This correlation with excitation map is referred to as CEM. By setting a threshold on the CEM (0.5 in the current study), an image mask (**Fig. 3.2.6d**) can be created to reject both stationary signals and displacements that are not synchronized with magnetic shaking, such as slow physiological motion or drifts and high-frequency vibration artifacts. Indeed, when this mask is applied to the original photoacoustic image with the three inclusions, signals from MNP-PPy and MNP are retained whereas those from PPy are filtered out (**Fig. 3.2.6e**).

**Figure 3.2.6g** presents the peak-to-peak displacement (PPD) map (**Fig. 3.2.6f**) after applying the cmmPA mask over it. This PPD map can be useful for further quantitative analysis. For example, *in vivo* tumor targeting could result in increasing PPD over time at the lesion site after injection as nanoparticles

accumulate. Alternatively, the quality of motion estimates can also be used as an additional mask to eliminate poor signal regions which can be affected by artifacts from bright neighboring regions, resulting in high values in CEM. We define the quality of speckle tracking as the mean value over all the frames of the normalized inter-frame cross-correlation magnitude. If corresponding regions in two consecutive images are too different (low signal-to–noise ratio or artifact), the quality coefficients of these regions are typically lower than those of bright regions. By setting a second threshold on the map of quality coefficient, poor signal regions can be filtered out.

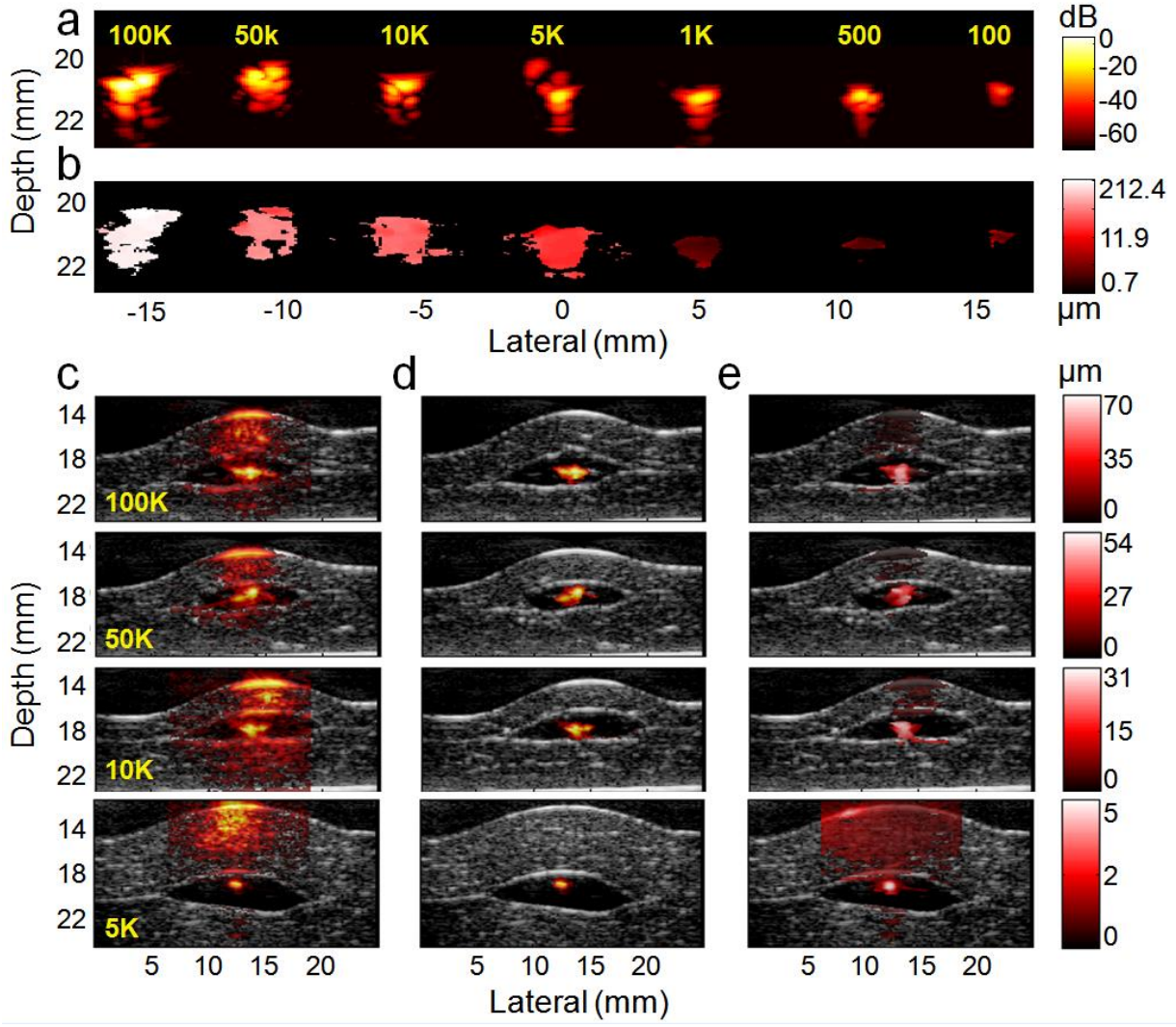

**Figure 3.2.7. Sensitivity and selectivity of cmmPA imaging for cancer cell detection through photoacoustic speckle tracking (PAST, 0.5 Hz magnetic excitation). (a)** Photoacoustic images of the phantom embedded with seven cell pellets (cell number from 100 to 100K) on a logarithmic scale over a 70 dB display range. **(b)** Peak to peak displacement image over a display range of 0.7-212.4 µm. Magnetic displacement decreases with smaller tumor size. **(c-e)** *Ex vivo* photoacoustic and cmmPA images of cell pellets (cell number from 5K to 100K) embedded in the middle of two porcine liver slices (producing strong background signals). c) Photoacoustic and **(d)** cmmPA images though PAST (hot colors) superimposed on ultrasound images (gray colors) on a logarithmic scale over a normalized dB display range. The black region around the centre hot spot (cell pellet) corresponds to the thin acoustically and optically transparent PVA layer used to encapsulate the cell pellets to avoid cell diffusion in tissues. **(e)** Displacement images of cell pellets over various displacement ranges.

To test cmmPA for tumor cell imaging, we first evaluated photoacoustic sensitivity under background-free conditions and the minimum number of cells required to detect magnetically-induced motion. HeLa cells tagged with the targeted MNP-PPy nanoparticles are pelleted, mimicking solid tumors, and embedded in a PVA phantom with elasticity similar to that of biological tissues (Young's modulus E = 4-8 kPa). As shown in **Figure 3.2.7a**, because the PVA phantom has low NIR light absorbance and, consequently, low photoacoustic signals, all seven cell pellets containing 100 to 100,000 tumor cells are clearly visible.

For magneto displacement characterization, peak-to-peak displacement was mapped for the seven cell pellets, using photoacoustic motion tracking. **Figure 3.2.7b** shows that tumor displacements vary from approximately 2 µm to 200 µm, depending on the total number of magnetic nanoparticles in the embedded cells, which contributes to the final magnetic response. Despite the general trend that larger tumor cell clusters move more than smaller ones, no simple relationship between displacements and cell numbers is found, because the volume of each inclusion cannot be controlled easily by manual pipetting of cells. Still, the magnetic motion of 100 tagged cells can be clearly differentiated using the cmmPA technology. These studies show that a small number of cells tagged with photoacoustic contrast agents can be readily detected under background free conditions.

In the presence of biological tissues, however, signals from the small number of cells are difficult to distinguish from tissue background signals. We evaluated cyclic mmPA's ability to enhance image contrast. MNP-PPy tagged tumor cell pellets were embedded in a PVA phantom and sandwiched

between two slices of porcine liver tissue. Pellets of 100k, 50k, 10k and 5K cells are used in this study because they are simple models of solid tumors, and are clearly visible when cutting the PVA phantom around them (smaller number of cells are hard to visualize during phantom cutting). Photoacoustic tracking (magnet excitation at 0.5 Hz) was used for cmmPA.

**Figure 3.2.7c** shows photoacoustic images (hot color scale) superimposed on ultrasound images (gray scale, to show tissue structure). The black region around the central hot spot (tumor cells) corresponds to the acoustically and optically transparent PVA layer. Clearly, due to the high photoacoustic background of liver tissue, tumor cells cannot be distinguished without a priori information of their location. Quantitative measurements show that the contrasts on dB-scale images of the four inclusions are +3.9 dB, +0.83 dB, -6.07 dB and -0.25 dB respectively, suggesting that small tumors cannot be detected by conventional photoacoustic imaging. In contrast, cmmPA images (**Fig. 3.2.7d**) show clear isolated signals from the tumor cells with background almost completely suppressed. The contrast improves by +31.3 dB, +34.5 dB, +41.4 dB and +29.1 dB, approximately 2 orders of magnitude better than the original photoacoustic images.

Based on these remarkable results, we expect smaller number of cells in the 100s to 1000s range can be detected with this technology, especially using MNPs of higher magnetic permeability, stronger magnets, and additional repetition cycles of magnetic shaking. Considering current tumors are often detected when they reach $mm^3$ and $cm^3$ in size, which constitutes 106 and 109 tumor cells[170], mmPA shows excellent potential for early diagnosis of small lesions. In addition, quantitative magnetic displacements values can potentially provide information correlated with the concentration of cells per imaging pixel (voxel). This hypothesis will be tested in future studies.

For *in vivo* testing, the frequencies of physiologic motions should be considered for cmmPA imaging. For example, human cardiac and respiration frequency are 0.6-1.2 Hz and 0.1-0.5 Hz, respectively, which are 5-10 times lower than those of mice. Clearly, the frequency of magnetic motions (0.5 Hz) overlaps with (or is too close to) physiological motion frequencies, making the background motion artifact difficult to reject. Therefore, the magnetic oscillation should be increased to a higher frequency. Note that the increased

frequency leads to reduced displacement during each magnetic pulse, thus the frequency and displacement should be balanced for both sensitive and specific detection of magnetic motions (e.g., 10 or 20 Hz). A practical difficulty encountered by first generation mmPA, however, is the slow frame rate of PAST, limited by the laser repetition rate (in our current setup, 20 Hz pulsed laser). Reliable speckle tracking (image patterns are tracked consecutively frame to frame) requires a large number of images to be captured during each magnetic pulse, but the frame rate of PAST is too slow when magnetic excitation is at 10 or 20 Hz. This issue is addressed by another key innovation in second-generation mmPA, hybridizing photoacoustic imaging with USST, because US plane wave imaging enables kHz frame rates.

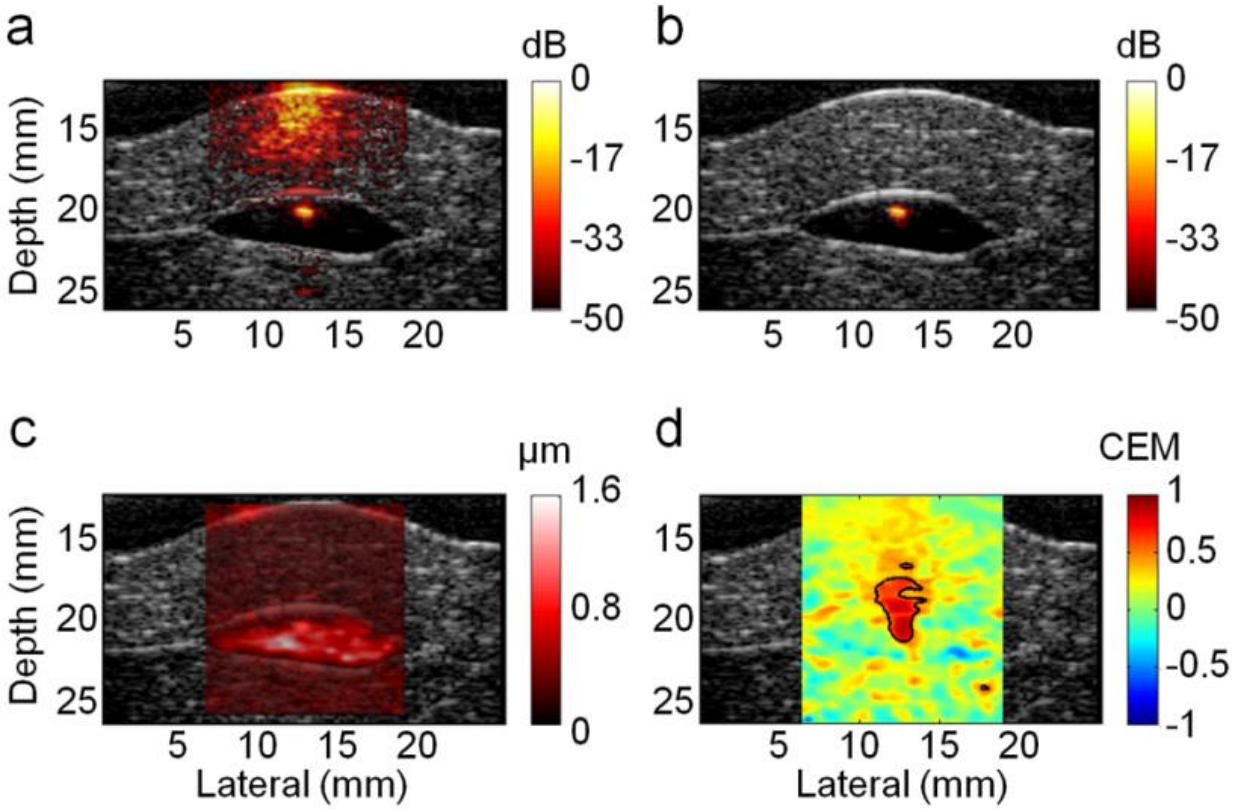


**Figure 3.2.8. Sensitivity and selectivity of *ex vivo* cmmPA imaging using US speckle tracking (USST). (a)** Photoacoustic image of the cell pellet containing 5K cancer cells overlaid on ultrasound images (gray colors) on a logarithmic scale over an 50 dB display range. **(b)** cmmPA image obtained with USST (10 Hz magnetic excitation). **(c)** Peak to peak displacement image over a display range of 0-1.6 μm. **(d)** Correlation with excitation map utilized to produce photoacoustic image background suppression with a threshold of 0.5.

To evaluate US tracking performance, the inclusion of 5K tumor cells, which is the detection limit of PAST at a magnet excitation of 0.5 Hz, was probed again using USST (magnet excitation at 10 Hz). **Figure 3.2.8b** shows clear isolated cell signals after background suppression from photoacoustic image (**Fig. 3.2.8a**). The contrast improves by +30.9 dB from +7.3 dB, consistent with the order of PAST improvement (+29.1 dB). However, it is important to note the difference between the results obtained with USST and PAST. Using PAST at the magnetic excitation of 0.5 Hz, the peak displacement is on the order of 5 μm. At magnet excitation 20 times faster, USST readily detects PPD at the 1 μm level (**Fig. 3.2.8c**). Remarkably, as shown in **Figure 3.2.8d**, the correlation map has high contrast with a clear delineation. It confirms that regardless of the speckle checking method, thresholding based on correlation functions is much more robust than thresholding on displacement magnitude in the presence of significant physiological motion.

### 3.2.5 *In vivo* cmmPA imaging of cancer cells from a mouse model

This technique was evaluated *in vivo* using a mouse model bearing subcutaneous injected HeLa cells pre-tagged with MNP-PPy nanoparticles. All animal procedures were approved by the University of Washington Institutional Animal Care and Use Committee.

The instrument setup is shown in **Figure 3.2.9a and b**. An imaging array working at 15 MHz (element pitch=0.1 mm) was connected to an ultrasound scanner. Light was delivered by two optical fibers and a magnetic core was positioned near the targeted zone. A translation stage was used to scan all devices along the mouse body for full 3-D data acquisition. Mice were anesthetized with isoflurane and positioned on an angled bench placed inside a tank. 10K tagged cells mixed with 100 μl Pluronic-127 gel (30%), a thermoresponsive and biodegradable polymer to hold the cells underneath the skin, were injected subcutaneously into the dorsum. An 8-cycle, 20 Hz magnetic excitation was applied during acquisition of 400 US frames (total imaging time of 0.5 s, frame rate 800 Hz).

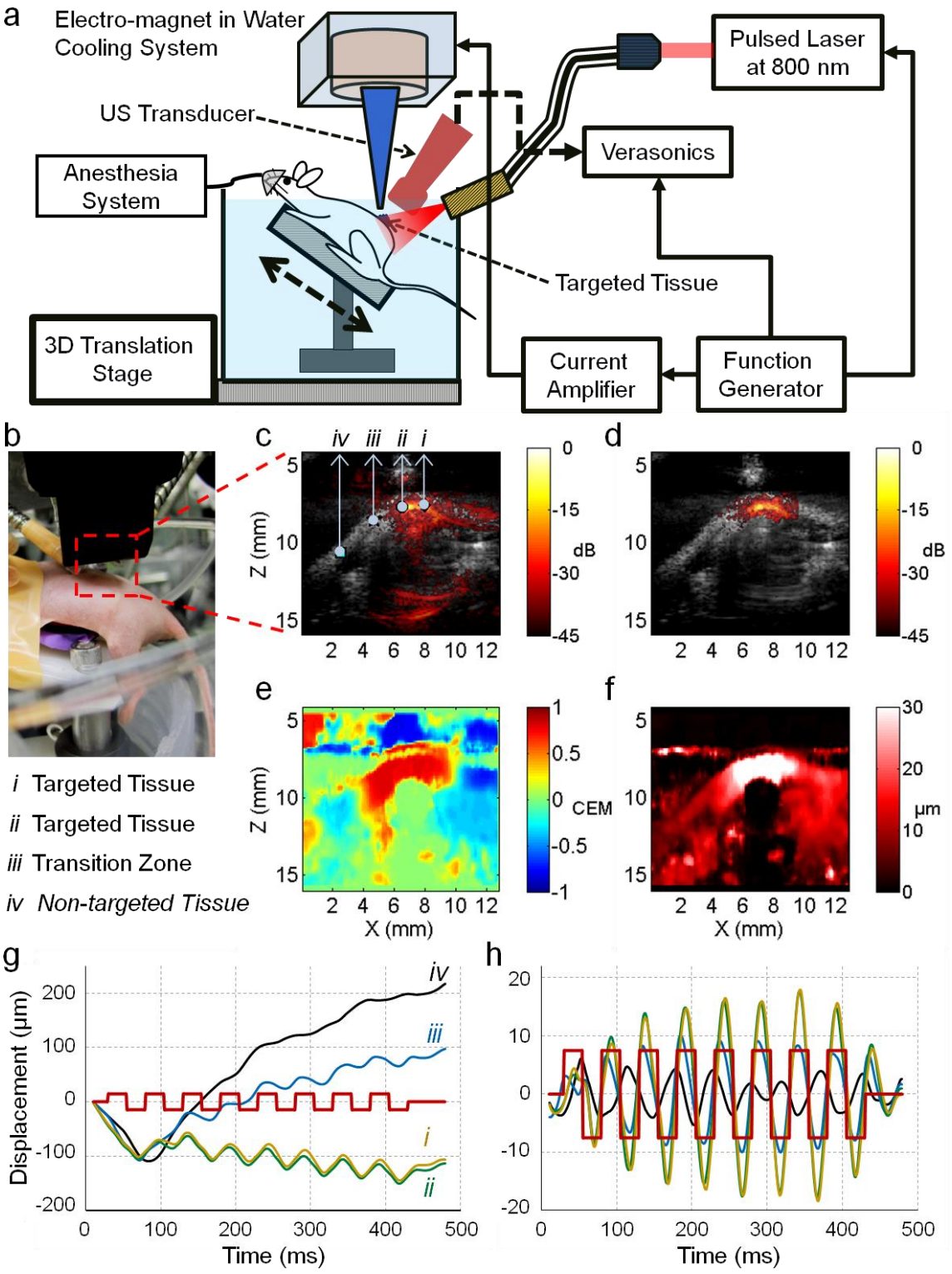
a
Electro-magnet in Water Cooling System
US Transducer
Anesthesia System
3D Translation Stage
Pulsed Laser at 800 nm
Verasonics
Targeted Tissue
Current Amplifier
Function Generator
b
i Targeted Tissue
ii Targeted Tissue
iii Transition Zone
iv Non-targeted Tissue
c
d
e
f
Z (mm)
X (mm)
dB
CEM
μm
g
Displacement (μm)
Time (ms)
h
Time (ms)

**Figure 3.2.9. *In vivo* cmmPA imaging of cancer cells from a mouse model following subcutaneously injection. (a)** Schematic of the *in vivo* cmmPA imaging set up. b) Photograph of a mouse imaging experiment. Anesthetized mouse positioned on an angled bench placed inside a tank and subcutaneously injected 10K cancer cells (tagged with nanoparticles) into the dorsum site, which was imaged (after 1h injection) through conventional photoacoustic imaging, cmmPA and US. **(c)** Photoacoustic/ultrasound overlaid image of tumor region containing i, ii) targeted, iii) transition and iv) non-targeted zones in the dorsum of living mice. **(d)** cmmPA image obtained with USST using 8-cycle 20 Hz magnetic excitation. **(e)** Correlation with excitation map utilized to produce photoacoustic image background suppression with a threshold of 0.5. **(f)** Peak to peak displacement image over a display range of 0-30 µm. **(g)** Raw cumulative displacements at zones indicated by markers (i-iv) on the photoacoustic image **(c)**. **(h)** Filtered displacement curves using a bandpass filter [8-70] Hz. The red square wave indicates magnetic excitation cycles.

**Figure 3.2.9c** presents a photoacoustic image (hot scale) overlaid on a US image. The injected cells cannot be distinguished from background tissues. However, the cmmPA image (**Fig. 3.2.9d**) shows a clearly delineated area corresponding to the tagged cells lying beneath the skin. This masking was obtained using a threshold of 0.5 on the correlation with excitation map (**Fig. 3.2.9e**) and a second threshold of 0.9 on the quality coefficient of motion tracking. Even if the peak-to-peak displacement map (**Fig. 3.2.9f**) could be used to obtain similar information, the amplitude of the threshold would have to be set to different values depending on the conditions without a universal standard. Moreover, a region with high displacements can be identified along a thin horizontal line at a depth of 7 mm through PPD map, while corresponding to image artifacts moving incoherently with the magnet, which is negative in CEM (**Fig. 3.2.9e**).

**Figure 3.2.9g** presents the absolute displacement curves at different locations (marked from i to iv with arrows pointing to in **Fig. 3.2.9c**). It can be seen that physiological motion produces a lower frequency response with continuous large drifting displacement than that from the magnet. These motions can be low-pass filtered and the resulting signals are shown in **Figure 3.2.9h**. Coherent motion is retrieved for the points (i and ii) at the center of the targeted zone whereas out-of-phase smaller motion is obtained a few millimeters away (point iii), corresponding to the propagation of a shear/surface mechanical wave along the skin. Low-frequency mechanical waves (surface or shear waves) can possibly propagate away from the targeted area and create a wrong interpretation about the measured displacements in term of source delineation. The bandpass filtering can also result in ringing of wideband physiological motion.

Thus, it is essential to account for the phase of the displacement to retrieve the location of the source of magnetic displacements.

The ultimate limit of induced displacements for the magnetic modulation technique is determined by the frequency (f) of the ultrasound signal and the electronic signal to noise ratio (SNR) of the imaging system. A simple propagation of error analysis yields the minimum detector displacement as a function of these two parameters:

$$displacement_{min} = \left[\frac{c}{4\pi\ SNR}\right]\left[\frac{1}{f}\right]\ ,$$

where c is the sound speed, f is the frequency, and the SNR is a dimensionless number. For a 15 MHz transducer and an SNR of 100 (40 dB, a typical value for the ultrasound images used in this study), this represents a minimum detectable displacement of 8 μm. Because a correlation technique is used over several periods of the magnetic excitation, representing a dwell interval on the order of 100 ultrasound frames, this means the minimum detectable displacement for the modulation technique should be on the order of 0.8 μm. As is evident from the results, sub μm displacements are clearly detected and can be used to produce a robust correlation with excitation map (CEM), leading to a highly selective cmmPA image.

The overall robustness of the magnetic modulation technique is a combination of its inherent sensitivity and immunity to background motion. Clearly, the displacement sensitivity approaches theoretical limits, as noted above. The results show that cmmPA can produce highly selective imaging of cancer cells tagged with magnetic nanoparticles for background displacements well over an order of magnitude larger than magnetically induced ones. Clearly, there will be cases where background motion may be several orders of magnitude larger than magnetically-induced motion, especially as the frequency of the magnetic excitation is increased, but simple time gating can be used to reduce this ratio to manageable levels. Consequently, the magnetic modulation technique presented here has both the sensitivity and robustness for potential *in vivo* application.

### 3.2.6 Summary

In summary, we have developed a new class of magneto-optical dual functional particles that are compact and uniform in size, NIR light absorbing, and scalable in synthesis. Compared to the conventional gold nanostructure-based NIR absorbers, the MNP-PPy nanoparticles are significantly more stable against laser irradiation, which is critical for imaging applications involving high-intensity lasers. In parallel, we have also developed a new generation of mmPA technology featuring two key innovations in motion detection, time coherence of displacement with cyclic magnetic excitation and ultrasound-based speckle tracking. In contrast to the first generation mmPA based on the absolute amplitude of magnetic-induced motion, the new system is capable of distinguishing contrast agent movement from physiological motions. Combined, the new imaging probe and cmmPA technology enable the first demonstration of mmPA in live animals, a key step toward ultrasensitive molecular imaging and clinical translation.

## 3.3 STABLY DOPED CONDUCTING POLYMER NANOSHELLS BY SURFACE INITIATED POLYMERIZATION

Conducting polymers such as polyaniline and polypyrrole (PPY) have captivated scientists for decades due to low cost, light weight, dispersibility, and more importantly their fascinating electrical, mechanical, and optical properties[56-58]. These properties have enabled a broad spectrum of applications such as optoelectronics, flexible circuits, catalysis, and smart fabrics[59-64]. Most recently, conducting polymers have emerged as an attractive material for biosensing and a better alternative to metal nanoparticles for photothermal imaging and therapy due to their improved photostability over metallic nanoparticles. Regardless of the applications, however, a long-standing intrinsic problem of conducting polymers is their poor resistance to de-doping. Current conducting polymers must be doped (often by oxidation, adding dopants to remove some delocalized electrons) to maintain their signature electrical and optical properties, but these dopants are not permanently 'integrated' into the polymer backbone, thus susceptible to dissociation.

Using PANI as an example, it is one of the first conducting polymers discovered, and arguably the most popular one for bioapplications (e.g., photothermal therapy and photoacoustic imaging (PA)) due to its concentrated NIR absorption[67-69]. The imaging contrast and heating efficiency, however, are far below expectation due to the de-doping issue in physiologic environment. PANI has two protonation states, emeraldine salt and emeraldine base, that are reversible through proto-nation (oxidization) and deprotonation (reduction). The two protonation states show very different electro-optical properties. In acidic environment, protonated emeraldine salt is highly conductive and has a strong NIR absorption peak (visually appears green due to strong ab-sorption in the blue and red); whereas in neutral or basic environment, the deprotonated emeraldine base is nonconductive and has extremely low NIR absorption (appears blue). Prior attempts to solve the problem have been focused on chemical modification of aniline's molecular structure (e.g., by covalently integrating negatively charged functional groups) to make its derivatives self-doped. These derivatives indeed show electroactivity in extended pH range, but at the cost of significantly reduced conductivity and absorption (orders of magnitude lower)[70-72].

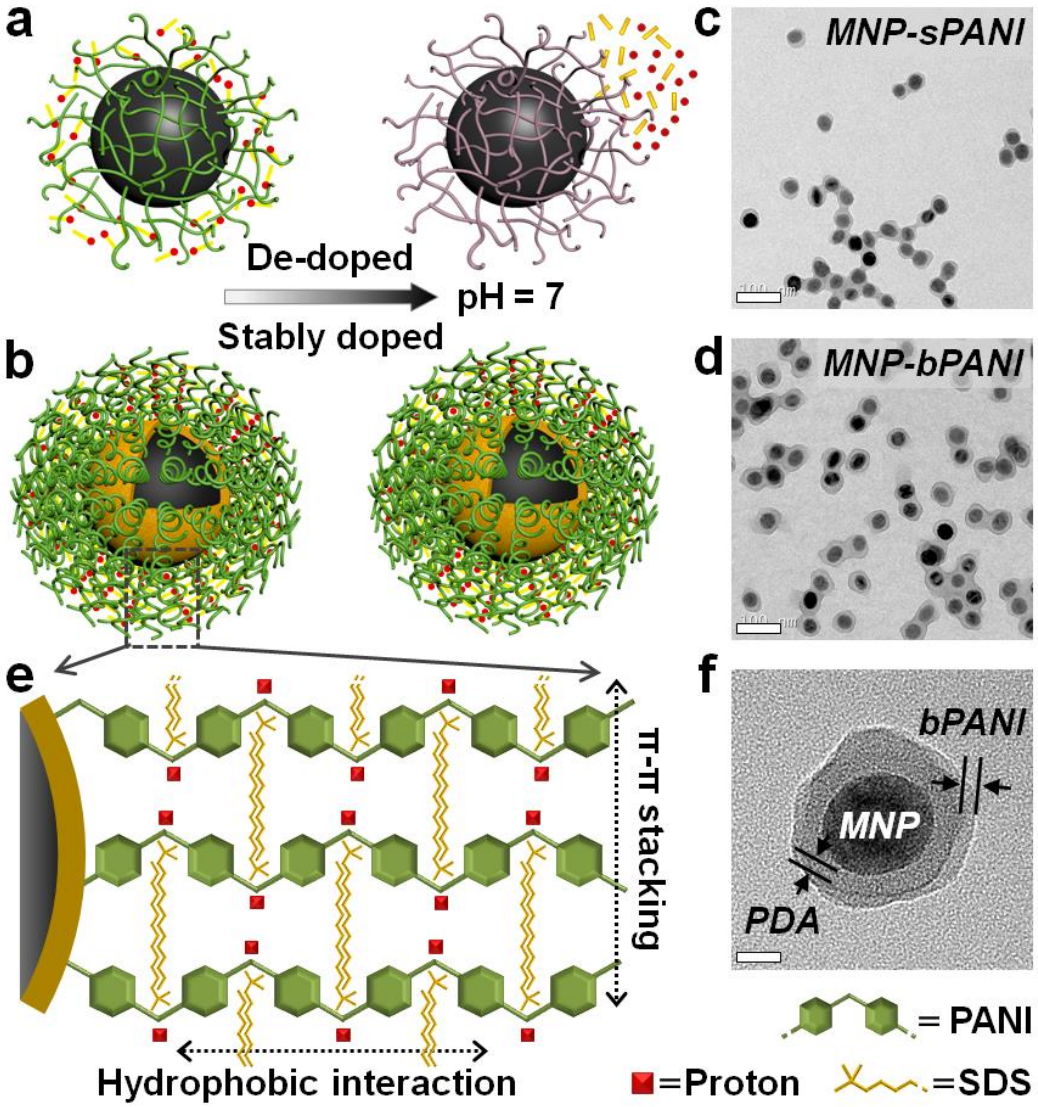


**Figure 3.3.1. Design of stably doped polyaniline nanoshells. (a)** Scheme illustrating conventional loosely packed PANI (spaghetti-like). The PANI layer losses its signature properties due to dopant leaching at neutral pH. **(b)** Densely packed brush PANI with excellent doping stability. **(c&d)** TEM showing successful coating of PANI nanoshells on MNPs. Scale bar, 100 nm. **(e)** Diagram illustrating high-density PANI brush polymerized on an intermediate PDA layer. Protons (red dots) and SDS (gold wires) are stably trapped due to strong interactions between the conjugate polymer chains and the dopants. **(f)** TEM showing PDA-PANI dual shell layers on a MNP. Scale bar, 20 nm.

### 3.3.1 High-density PANI brush polymerization on an intermediate polydopamine layer

To simultaneously achieve excellent electro-optical properties and doping stability at physiological pH, we proposed a new strategy, changing the polymer configuration and density rather than its molecular structure, and we demonstrated this design using PANI as an example. The same strategy can be readily extended to other conducting polymers because complex chemical reactions are not needed. As shown in **Figure 3.3.1**, stronger interactions between conjugated polymers and dopant ions can be expected if the polymer chains are densely packed because of increased interactions between adjacent dopant ions and aniline segments. Achieving this design experimentally, however, is difficult. Conventional approaches of making and depositing PANI on a surface result in random aggregated chains that are only loosely packed (spaghetti like)[171], because polymer chains must fight against steric hindrance and diffuse through existing polymer layer to increase packing density. In contrast, if PANI can be grown in situ on a surface (surface initiated polymerization), it would be much easier for small monomer molecules to diffuse to the propagating end of immobilized polymer chains, producing densely packed polymer brushes[172-175]. Here, we report such a general platform by exploiting an intermediate layer made of biomimetic polymer, polydopamine (PDA), which exhibits excellent reactivity towards nucleophiles (e.g., the amine group in aniline) even in aqueous environment[87, 121]. Magnetic nanoparticles (MNP) coated with a thin layer of PDA allow aniline to anchor on it at high density for surface initiated polymerization. The resulting multi-functional PANI nanoparticles show outstanding conductivity, NIR absorbance at physiologic pH, and surprising non-fouling property.

Before probing the electro-optical properties of the MNP-PANI nano-particles with spaghetti or brush shell structures (MNP-sPANI or MNP-bPANI), we first characterized their sizes with transmission electron microscopy (TEM) and dynamic light scattering (DLS) to confirm successful synthesis. **Figure 3.3.1c and d** clearly show the core-shell structure for both nanoparticles confirming successful coating of PANI nanoshell. From TEM measurements, the core MNPs have a diameter of 39.7 ± 6.1 nm. Upon coating with PDA and the PANI brush, the nanoparticle size increases to 48.8 ± 5.6 and 65.2 ± 7.9 nm, respectively. Due to similar electron density, it is difficult to clearly visualize the boundary between the

PDA and PANI layers, but some particles under high-resolution TEM indeed show dual shell layers (**Fig. 3.3.1f**). Particle formation was further confirmed with DLS, which shows that the hydrodynamic diameters of MNP, MNP-PDA, and MNP-PDA-bPANI are 37.8 ± 7.8 (PDI, 0.157), 43.8 ± 6.0 (PDI, 0.166), and 68.1 ± 9.1 nm (PDI, 0.117), respectively, not only matching the values obtained with TEM, but also the size range for efficient cell uptake and tissue penetration[153, 154]. The size of MNP-PDA-bPANI can be also tuned depending on applications.

### 3.3.2 Comparison of the doping stability between MNP-sPANI and MNP-bPANI

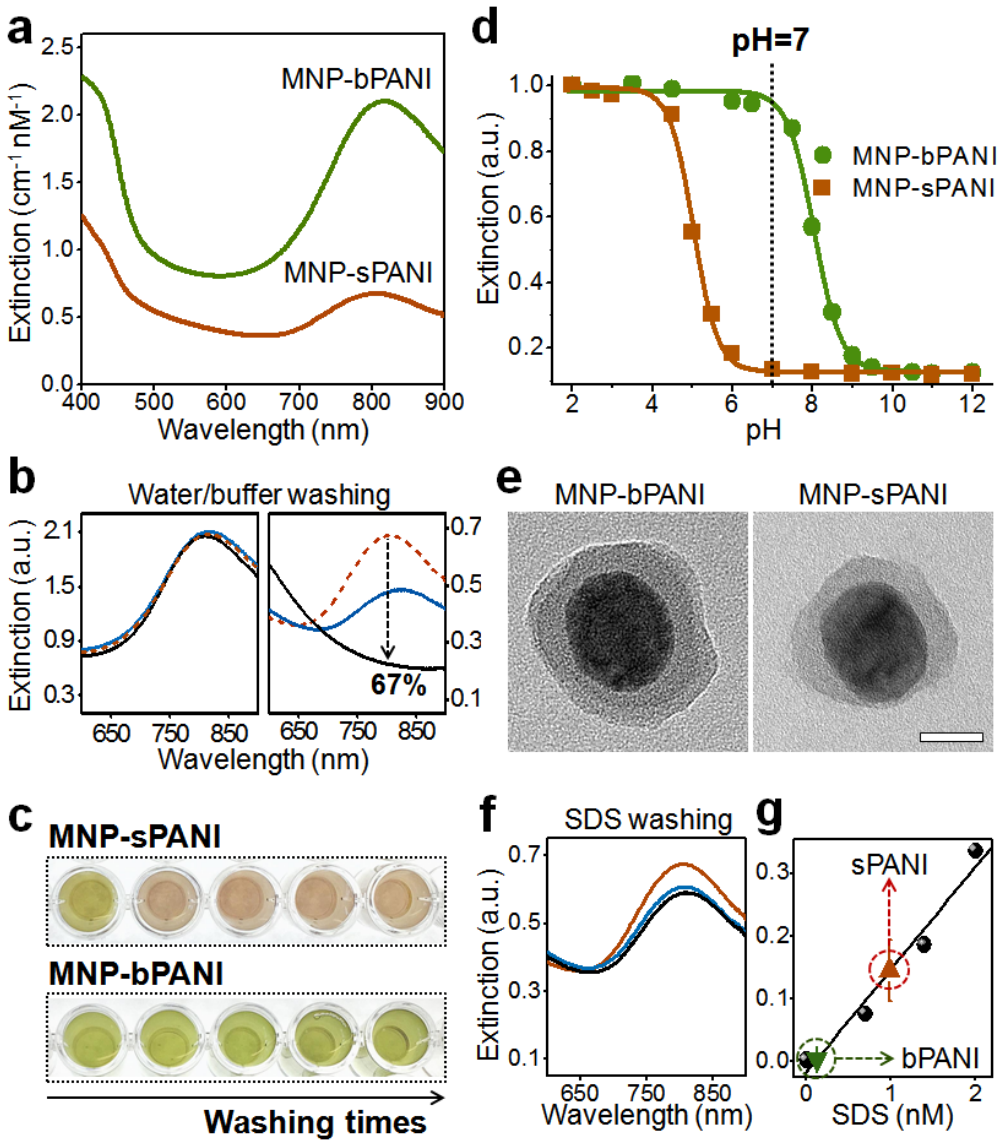

**Figure 3.3.2. Doping stability comparison between MNP-bPANI and MNP-sPANI. (a)** Extinction spectra of MNP-bPANI (green) and MNP-sPANI (red) at pH 2. **(b)** Extinction spectra of MNP-bPANI (left) and MNP-sPANI (right) before (red) and after rinsing with water (blue) or PBS buffer (black). MNP-bPANI's extinction at 800 nm remains constant, whereas MNP-sPANI drops by 67%. **(c)** Color change of MNP-sPANI with one-round of washing. MNP-bPANI remains unchanged with repeated washing. **(d)** Normalized extinction at 800 nm of PANI under various pH. MNP-sPANI's NIR absorption is strong below pH 4, but reduces to background level at neutral pH. MNP-bPNAI's absorption remains strong at pH 7. **(e)** TEM showing PANI nanoshells after rinsing. Scale bar, 20 nm. **(f)** Minor extinction reduction of MNP-sPANI before (red), and after washing with water (blue) or PBS buffer (black) both containing 40 mM SDS. **(g)** Detection of SDS leaching from MNP-sPANI, but not from MNP-bPANI.

Next, we directly compare the doping stability of MNP-sPANI and MNP-bPANI. Due to the large surface area and thin shell thickness (~ 15 nm PANI layer for both cases), the dopants are highly accessible and responsive to the environment. Immediately after synthesis, the MNP-sPANI and MNP-bPANI nanoparticles were magnetically isolated and suspended in water at the same concentration. **Figure 3.3.2a** shows that, in acidic condition (pH 2), both MNP-sPANI and MNP-bPANI have concentrated NIR extinction. At 800 nm, MNP-bPANI's extinction is approximately 3x stronger than MNP-sPANI, largely due to bPANI's higher polymer density. When the two nanoparticles were rinsed with water or phosphate-buffered saline (PBS) buffer, however, the conventional MNP-sPANI quickly became de-doped and lost its signature optical properties. As shown in **Figure 3.3.2b**, while the extinction value of MNP-bPANI at 800 nm remains constant, MNP-sPANI's extinction drops by 30% after rinsing with water once and completely flats out after rinsing with PBS buffer for only one time. Note that the remaining 33% extinction after PBS washing is mainly due to the scattering contribution, which is not useful for photothermal imaging and therapy. Indeed, when the solutions of MNP-sPANI and MNP-bPANI were probed by photoacoustic imaging, the signal strengths (reflecting the absorption contribution in overall extinction) of MNP-bPANI is 71 times stronger than MNP-sPANI, demonstrating the significance and impact of stable doping on photothermal nanoprobes.

De-doping also can be easily detected by visual observations. Due to strong extinction in the blue and red regions, the doped PANI (emeraldine salt) is green. As shown in **Figure 3.3.2c**, the color of MNP-sPANI changed from green to brown after one-round rinsing with PBS, whereas MNP-bPANI remained the same color even after repeated washing. Quantitative measurements of MNP-sPANI's extinction at 800 nm

against pH values show a sharp drop at pH 4 (**Fig. 3.3.2d**). At pH 7, the NIR extinction virtually disappears, making it unsuitable for photothermal-based applications. In contrast, the transition of MNP-bPANI occurs in alkaline conditions. At physiological pH, its absorption remains constant compared to that in acidic conditions. Although not directly used in the current study focusing on bioapplications of PANI, we probed the conductivity of MNP-sPANI and MNP-bPANI because it is the signature property of PANI and is directly affected by the doping state, too. Remarkably, the conductivity of MNP-bPANI reaches an unprecedented value of 3.25 S/cm for PANI nanostructures approaching that of bulk PANI (~5 S/cm), while the conductivity of MNP-sPANI is only $1.76 \times 10^{-3}$ S/cm, approximately 1,850 times lower. This comparison shows the potential impact of the new brush PANI on applications in electronics.

A question directly related to the huge difference of electro-optical activities is how the dopant ions (proton in this case) are confined in the bPANI layer. The MNP-sPANI and MNP-bPANI share similar sizes and shell thickness (63 nm vs 68 nm by DLS measurement, shell thickness ~15 nm), thus the performance difference is unlikely due to the nanoparticle size effect. To probe this question, we first imaged MNP-sPANI and MNP-bPANI before and after buffer washing to rule out the possibility that the disappearance of conductivity and NIR absorption of MNP-sPANI is due to dissociation of the PANI layer and the core MNP (peeling off from the surface). As shown in the TEM images (**Fig. 3.3.2e**), the morphology of the particles did not change after washing, indicating the chemical and colloidal stability of MNP-sPANI. Second, at neutral or physiological pH, the dopant proton is accompanied by its counterion sodium dodecyl sulfate (SDS) to maintain charge neutrality. Therefore, we set out to evaluate the release profile of SDS from the PANI shell and its effect on confining protons. We rinsed MNP-sPANI with PBS buffer containing SDS. Surprisingly, even at neutral pH, the change of NIR absorption is insignificant (**Fig. 3.3.2f**), in contrast to washing with PBS buffer only (**Fig. 3.3.2b**). This result indicates the effect of counterions (SDS) on helping stabilize protons in the PANI layer. Thus the improved doping stability of MNP-bPANI is likely resulted from stable trapping of the bulky SDS molecules, which in turn help confine protons. To confirm it, we quantitatively assessed SDS release using a colorimetric assay. As shown in **Figure 3.3.2g**, significant SDS leaching is detected when MNP-sPANI is suspended in PBS, but not

MNP-bPANI. Indeed, previous theoretical modeling has suggested that increased polymer grafting density offers lower degree of ion dissociation[176, 177].

### 3.3.3 Evaluation of PANI nanoshells' non-specific binding and cytotoxicity

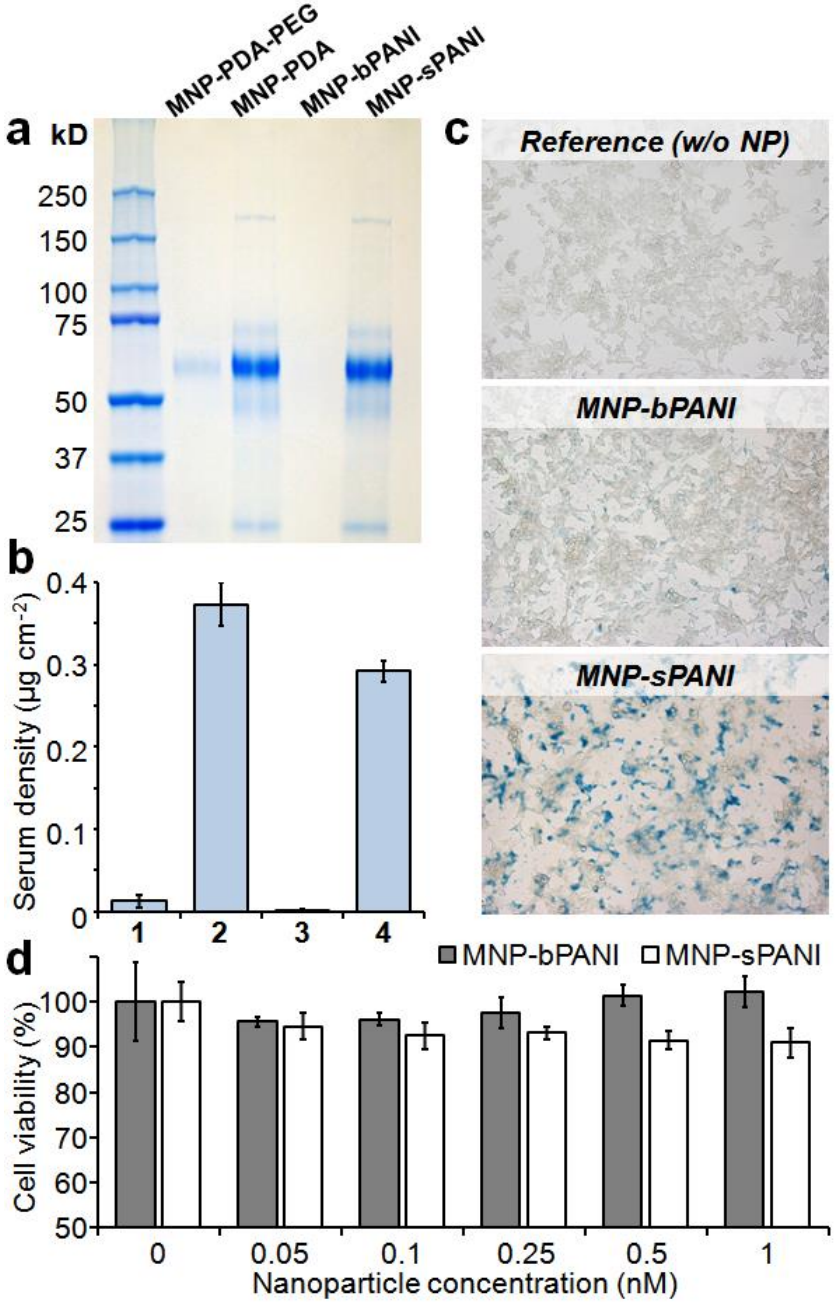

**Figure 3.3.3. PANI nanoshells' non-specific binding and cytotoxicity. (a)** Detection of adsorbed protein on PAGE. MNP-bPANI shows lower protein adsorption than all other groups, even PEG-coated particles. **(b)** Quantification of adsorbed protein using the BCA assay. From left to right, the samples are MNP-PDA-PEG, MNP-PDA, MNP-bPANI, and MNP-sPANI. **(c)** Bright-field images of LNCaP cells untreated, treated with MNP-bPANI or MNP-sPANI. Cells were stained with Prussian blue. **(d)** Dose-dependent cytotoxicity of MNP-bPANI and MNP-sPANI in LNCaP cells.

Besides the intrinsic eletro-optical properties, two additional issues must be investigated before using the new particles in biomedical imaging and therapy. First, we studied whether the PANI nanoshell, which serves as the interface between the nanoparticle and the biological environment, produce significant non-specific binding.

For comparison, we incubated four groups of nanoparticles (MNP-PDA, MNP-sPANI, MNP-bPANI, and MNP-PDA-PEG) in human serum to assess the level of non-specific protein adsorption. Surprisingly, despite the same material, MNP-sPANI and MNP-bPANI show completely different performances in this test. The random spaghetti PANI layer non-specifically captured high level of serum proteins, similar to the PDA coated MNPs. As shown in the polyacrylamide gel electrophoresis (PAGE) image (**Fig. 3.3.3a**), majority of the proteins non-specifically bound to MNP-PDA and MNP-sPANI are in the size range of 50-75 kDa.

In contrast, MNP-bPANI exhibits outstanding non-fouling property, even outperforming the gold-standard surface coating material, PEG. Quantitative bicinchoninic assay (BCA) determining the quanti-ty of proteins stripped from nanoparticle surfaces show that protein adsorption on MNP-bPANI is 13 times lower than that on MNP-PDA-PEG (**Fig. 3.3.3b**).

This remarkable non-fouling property is likely resulted from the com-bination of the balanced cations and anions trapped in the bPANI layer (zeta potential +1.58 mV) and steric repulsion from the densely packed polymer brush. In contrast, sPANI's loose structure does not patch the MNP surface well while featuring excessive positive surface charges (zeta potential +27.3 mV) due to dopant release in physiological environment. Compared to prior efforts to deliberately synthesizing zwitterionic polymers through chemical reactions[178], the zwitterionic pairs in the bPANI layer are physically trapped, making this

technique potentially applicable to other conducting polymers. Similar non-fouling feature was also observed in cells.

As shown in **Figure 3.3.3c**, after incubation of 3h, cell uptake of MNP-bPANI is significantly lower than MNP-sPANI, highlighting its advantage in reducing non-specific binding.

The second issue we probed was the impact of MNP-bPANI on cell viability. Plot of dose-dependent cytotoxicity (**Fig. 3.3.3d**) shows that after 24 hour exposure to cells, MNP-bPANI is essentially non-toxic in the concentration range of 0-1 nM. In comparison, MNP-sPANI shows minor cytotoxicity, likely due to two factors, higher level of cell uptake and SDS release in physiological environment.

### 3.3.4 MNP-bPANI for magnetomotive photoacoustic imaging

To demonstrate the application of magneto-optical MNP-bPANI in molecular imaging, we functionalized the nanoparticle with a small-molecule ligand targeting prostate specific membrane antigen (PSMA), one of the most specific biomarkers expressed in prostate tumor epithelial cells and attractive targets for imaging and therapeutic interventions (e.g., ProstaScints scan)[179]. The targeting ligand 2-[3-(1,3-dicarboxy propyl)-ureido] pentanedioic acid (DUPA) with a reactive azide group (**Fig. 3.3.4a**) was linked to the highly accessible high-density amine groups at the terminal of the bPANI polymer chains.

To test DUPA-mediated cell binding and uptake, LNCaP cells were treated with the nanoparticles for 3 h. As shown in **Figure 3.3.4b**, DUPA functionalized MNP-bPANI nanoparticles were efficiently taken up by the cells (for control see **Fig. 3.3.3c**). The targeting and uptake specificity was further confirmed by co-incubation of the targeted nanoparticles with free DUPA molecules (uptake inhibition through competition).

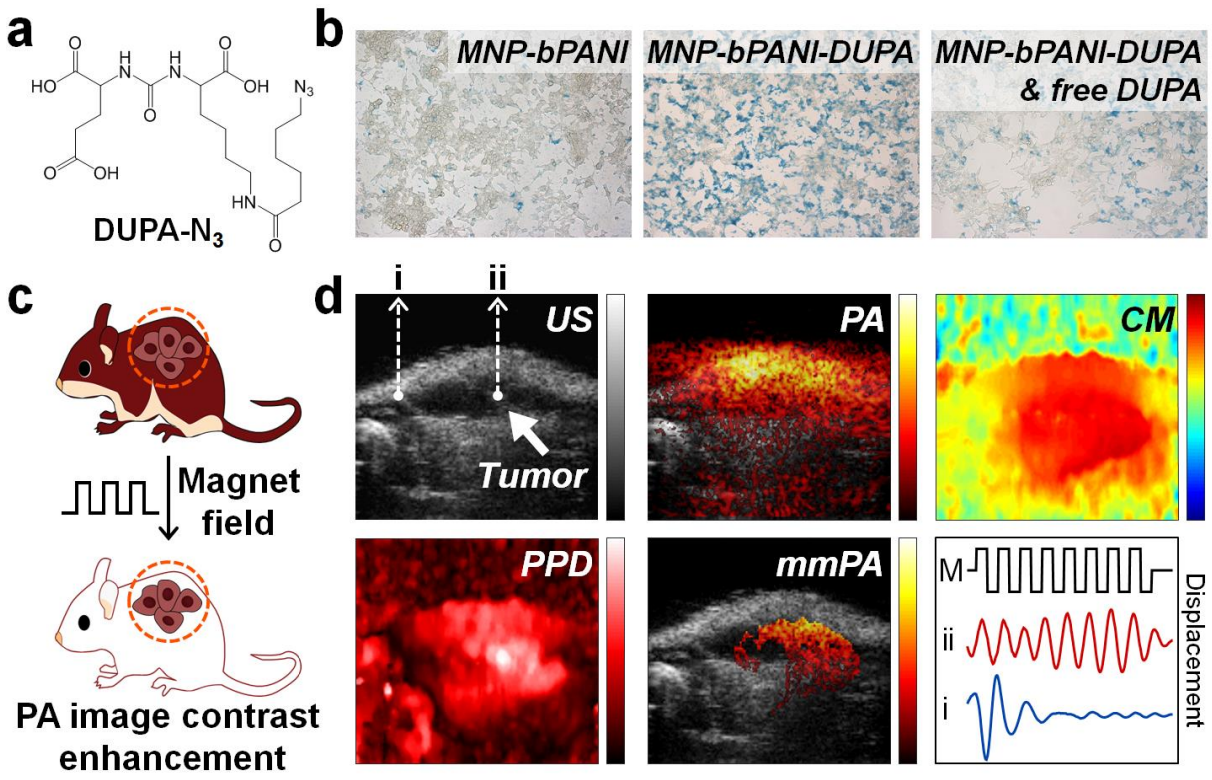


**Figure 3.3.4. MNP-bPANI for PA imaging. (a)** Chemical structure of DUPA with an azide group for conjugation. **(b)** Bright field images of LNCaP cells treated with MNP-bPANI, MNP-bPANI-DUPA, or MNP-bPANI-DUPA together with free DUPA. Cells are stained with Prussian blue. **(c)** Schematic of mmPA imaging contrast enhancement. **(d)** US: ultrasound image over a 35 dB display range; PA: conventional PA image overlaid with US over a 40 dB display range; CM: correlation with magnetic excitation map over a (-1 (blue), 1 (red)) display range utilized to produce PA background suppression using a threshold of 0.7; PPD: peak to peak displacement image over a (0 (dark), 18 (light)) μm display range; mmPA: mmPA image overlaid with US over a 40 dB display range. Displacements over time at two representative regions. Displacement of region ii correlates with the oscillating field, but not region i.

Finally, we explored the use of MNP-bPANI for PA imaging utilizing its magnetic and NIR-absorption properties. PA imaging combines intense pulsed laser irradiation of a contrast agent (typically with absorbance in the NIR spectrum for maximum heat generation) with ultrasound detection of the thermally induced acoustic waves[77]. Recently, we have developed an advanced PA imaging technology, magnetomotive photoacoustic imaging (mmPA) that is capable of enhancing imaging contrast by 2-3 orders of magnitude (**Fig. 3.3.4c**)[40]. A critical component of this powerful technology is a contrast agent with coupled magnetic property and NIR absorption. During real-time PA data acquisition post contrast

agent administration, an oscillating magnetic field is applied. The magneto-NIR absorbing dual functional nanoprobes move as a result of their strong magnetization, creating a moving source within a PA image. Non-magnetic PA sources do not move coherently with the applied field during this entire interval. Consequently, coherent motion processing of a PA image sequence can identify sources related to the coupled nanoparticles and reject all back-ground signals, whether from diffuse or localized sources. This intelligent combination of nanostructures and the signal processing technique significantly enhances imaging contrast, rendering ultrasensitive *in vivo* PA imaging possible.

Having confirmed MNP-bPANI's biological targeting and electro-optical properties, we proceeded to apply it to *in vivo* mmPA tumor imaging. A small-animal tumor model was established by injecting LNCaP prostate tumor cells subcutaneously in mice. After the tumor reached ~150 $mm^3$, MNP-bPANI-DUPA was administered via intratumoral injection. The prostate tumor was detectable in the PA image (**Fig. 3.3.4d**). However, the tumor site cannot be distinguished from background tissues (especially the laser illumination spot on the skin) under conventional PA imaging. Applying an oscillating magnetic field (10 Hz), a correlation map was created to present the synchronized motions between every pixel in the images and the magnetic fields. Next, a map of peak-to-peak displacement was created to show the motion amplitude of the pixels. Notably, the mmPA image (PA image masked by the correlation map) shows a clearly delineated area corresponding to the tumor lying beneath the skin, because it moves coherently with the oscillating magnetic field.

### 3.3.5 Summary

In summary, we have developed a technology to synthesize conducting polymers with high resistance to de-doping and well-maintained eletro-optical properties in physiological environments. In contrast to prior attempts based on chemical modification of monomers (complicated procedure with limited success), we achieved stable doping by engineering a dense brush polymer layer that is capable of trapping dopants with high affinity. Experimentally, the key to successful grafting the polymer brush on MNP surface is the intermediate PDA layer, taking advantage of its high reactivity to aminated molecules. Using PANI as an example, we show that its conductivity at neutral pH is three orders of magnitude higher than

conventional PANI with random polymer network, approaching the value of bulk materials which is unprecedented for PANI nanostructures. Similarly, bPANI's NIR absorption is two orders of magnitude higher than that of sPANI, yielding an excellent NIR nanoprobe for photothermal imaging and therapy. A further surprising finding of the stably doped bPANI is its anti-fouling capability, even outperforming the gold-standard coating material, PEG. Combining the electrical, optical, and interfacial properties of the stably doped conducting polymers, we envision this simple and general approach will inspire a broad spectrum of applications in electronics, bioimaging, sensing, coating, and smart textile.

## 3.4 FUNCTIONAL PHOTOACOUSTIC IMAGING OF GASTRIC ACID SECRETION USING PH-RESPONSIVE POLYANILINE NANOPROBES

Gastrointestinal disorders affect approximately 70 million individuals and cause more than 236,000 deaths annually in the United States alone[73]. Gastric acid secretion is a critical function in digestion and assimilation, and gastric acid secretory disability is involved in many gastrointestinal diseases, such as Zollinger-Ellison Syndrome, pernicious anemia, chronic gastritis, atrophic gastritis, and gastric carcinoma[180]. Therefore, real-time monitoring pH in the stomach can offer major benefits in both diagnosis and treatments of these diseases.

Unfortunately, functional imaging of the stomach and real-time measuring gastric acid secretory ability are difficult due to the lack of a simple, accurate, and non-invasive approach[75]. Currently, a number of direct and indirect pH measurement strategies exist, with gastrointestinal intubation (insert a plastic tube through the nose or mouth down into the stomach) and radio telemetry capsule (patient swallows a pH-sensing capsule) being the most popular for continuous direct assessment of gastric pH conditions[76, 181-184]. However, these tests suffer from complications, poor patient tolerance, and in particular inappropriateness for infant patients (e.g., hyperacidity, achlorhydria, and gastroesophageal reflux disease or GERD). Therefore, innovations in safe and non-invasive imaging technologies enabling functional imaging of the stomach are urgently needed for accurate diagnosis and effective treatment of gastrointestinal diseases.

Photoacoustic (PA) imaging has the potential to address this problem because it is a non-ionizing, non-invasive, and low cost imaging modality, combining the rich chemistry and spectral tunability of optical contrast agents, and the spatial resolution of ultrasound detection deep within tissue[77]. Indeed, PA-based imaging and detection has been demonstrated in various disease models, including intestinal diseases[78].

During PA imaging, light-absorbing dye molecules, polymers, or nanoparticles (mostly absorbing in the near-infrared (NIR) region to maximize light penetration depth and heat generation) are often used to provide imaging contrast. For example, based on PA imaging, organic dyes (indocyanine green and other small NIR molecules) have been utilized for tumor imaging and diagnosis, whereas inorganic

nanoparticles (Au nanorod and Au nanoshell) have also been applied for brain vasculature imaging and other bio-imaging applications[40, 79, 185-188]. Similarly, conductive polymers have been proposed as a better alternative because of their excellent absorption property similar to Au nanostructures and their improved photostability over the metallic nanostructure counterpart[189].

Using polyaniline (PANI), one of the first discovered conductive polymers, as an example, it has a concentrated absorption peak centered around 800 nm, ideal for photothermal-based imaging and therapy. However, this strength in spectral property has not translated into wide-spread uses in biological systems because a common problem of conductive polymers is their instability at neutral pH. In acidic environment, protonated polyaniline (doped) is highly conductive and has a strong NIR absorption peak; but in neutral or basic environment, polyaniline is deprotontated (dedoped) and consequently losses its conductivity and NIR absorption. This problem limits its use in most biological imaging applications, but can be useful for functional imaging of the stomach, where the pH is as low as 1-2 for human.

Here, we report the utilization of this seemingly major drawback (pH-sensitivity) of conductive polymers for gastric acid secretory assessment in combination with PA imaging. Converting this disadvantage to an advantage in imaging can be potentially extended to other pH-sensitive polymers and dye molecules, and can help solve the suffering and side effects of gastrointestinal intubation in hyperacidity, achlorhydria, and GERD patients (in particular infants and elderly).

### 3.4.1 Design of MNP-PANI (mPANI) nanoprobes for gastric acid secretion measurement

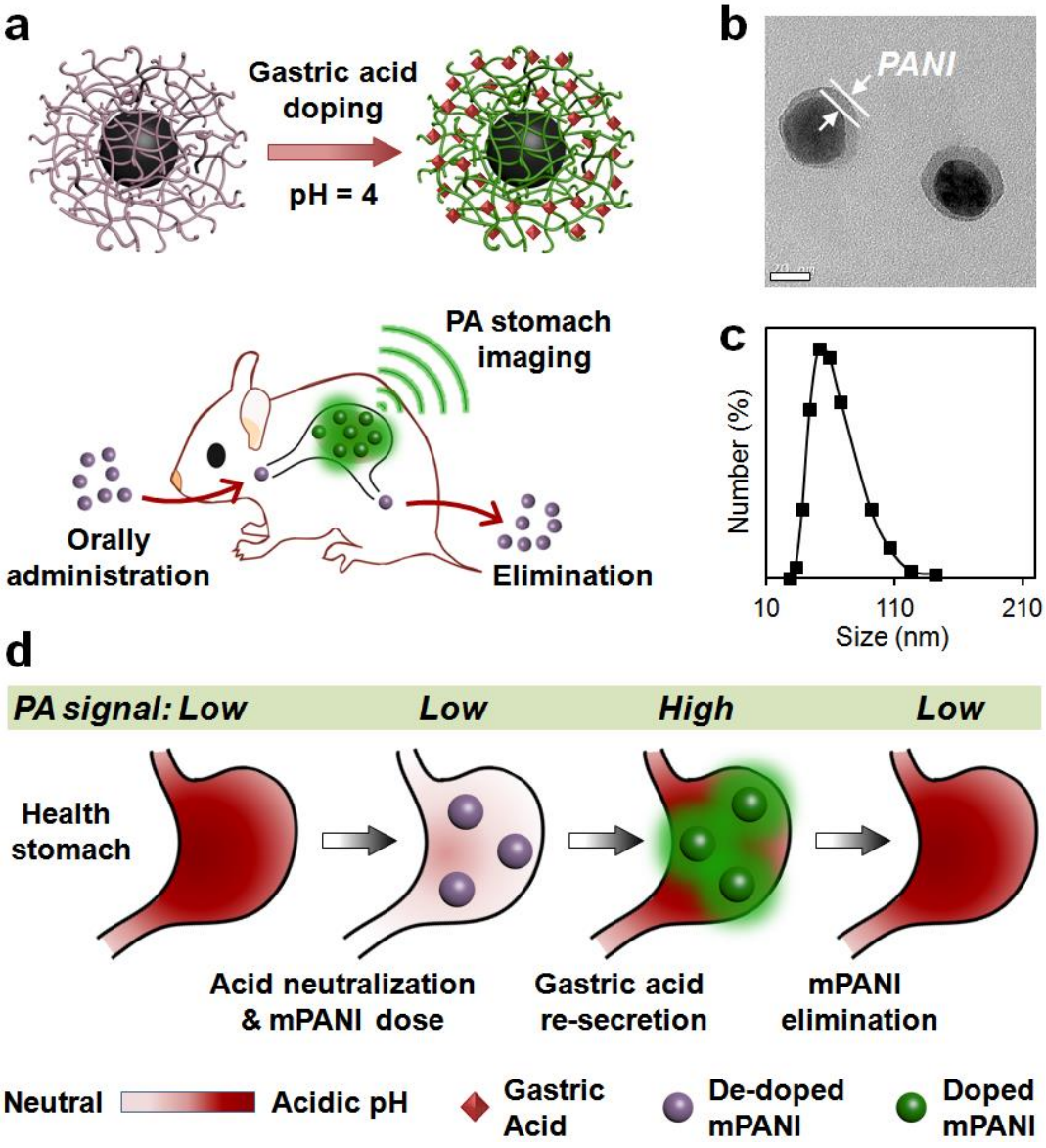


**Figure 3.4.1. Design of MNP-PANI (mPANI) nanoprobes for gastric acid secretion measurement.** **(a)** Schematic illustrating the doping process of PANI coated MNPs via gastric acid. NIR absorbance of orally administered de-doped MNP-PANI increases due to acid doping of the conductive polymer inside mouse stomach. The signal enhancement is detected through PA imaging. **(b)** TEM showing successful coating of PANI nanoshells on MNPs. Scale bar, 20 nm. **(c)** MNP-PANI nanoparticles' hydrodynamic size of 56.0 ± 6.1 nm. **(d)** Diagram illustrating the protocol of the gastric acid secretory assessment.

To simultaneously achieve rapid and sensitive pH responses during gastric acid secretion, a layer of PANI was coated onto iron oxide nanoparticle as a PA contrast agent for oral administration (**Figure 3.4.1**). The thin layer of PANI allows fast proton diffusion and consequently fast responses to pH fluctuation; whereas the magnetic nanoparticle (MNP) core serves as a structural template for uniform PANI coating, a sacrificial oxidant for aniline polymerization, and potentially a contrast agent for magnetic resonance imaging.

To confirm formation of the core-shell nanostructure, transmission electron microscopy (TEM) and dynamic light scattering (DLS) were used to measure the nanoparticle sizes. **Figure 3.4.1b** shows a PANI shell layer of approximately 15 nm around the MNP core (36.5 ± 2.7 nm in diameter). As a result, the overall size of the core-shell nanoparticle is 50.6 ± 7.9 nm. The hydrodynamic size of the particle in aqueous solution was further characterized using DLS. As shown in **Figure 3.4.1c**, the hydrodynamic diameter of the core-shell nanoparticle is 56.0 ± 6.1 nm, slightly larger than the value measured by TEM, likely due to the electrical double layer on nanoparticle surface. It has been shown that particles of this size are sufficiently large to avoid passive diffusion through the gastric mucosal layer[78].

To apply the pH-sensitive nanoparticles and PA imaging to gastric acid secretion assessment, experiments were designed based on current clinical practice of stomach function testing[190]. As shown in **Figure 3.4.1d**, MNP-PANI nanoparticles suspended in sodium bicarbonate solution (pH 8) are administered in mice orally. The sodium bicarbonate solution leads to pH rise inside stomach from acidic to basic, and this alkali challenge subsequently triggers gastric acid secretion via parietal cells.[13] For normal stomach function, gastric acid secretion will gradually reduce the gastric pH to normal (pH < 4 for human) in approximately 30 min (for human), whereas abnormal acid secretion could take significantly longer or shorter time to restore the original pH in stomach.

This entire process can be monitored by PA imaging non-invasively, because the MNP-PANI nanoparticles' pH sensitivity (initially de-doped with no or weak NIR absorption due to sodium bicarbonate solution's high pH and later re-doped by protonation with strong NIR absorption when the gastric pH

return to the normal value). Towards the end of the imaging, the PA signal decays as the MNP-PANI exits the acidic stomach, and eventually exits the body in feces.

### 3.4.2 Evaluation of simulated gastric acid doping of MNP-PANI (mPANI)

Before applying this technology to animal models, two key factors critical to the technology application must be confirmed: (i) does the thin PANI shell provide instant responses to pH changes through PA imaging; and (ii) is the nanoshell sufficiently stable against intense irradiation by pulsed laser during PA imaging and the extremely low pH in the stomach?

To probe the pH responsiveness, the MNP-PANI particles were suspended in buffers with different pH values. **Figure 3.4.2a** shows that the particles had low NIR extinction (largely due to scattering rather than absorption that matters for PA imaging) at pH 8. However, when these de-doped nanoparticles were transferred into simulated gastric fluid (pH 1, SigmaAldrich), they were rapidly doped and exhibited strong concentrated NIR extinction in less than 2s (the fastest we could handle the sample and take an absorption measurement), and the absorption did not further increase with longer incubation time, indicating instant proton doping throughout the nanometer-thick PANI layer.

Quantitative measurements of PANI's extinction at 800 nm vs pH values show a sharp increase between pH 2 and 6. At pH 4, the extinction (absorption + scattering) is 7.5-fold stronger than the signal at pH 8 (**Figure 3.4.2b**). Similar effect was also observed through PA measurements. As shown in **Figure 3.4.2c**, the PA signal intensity (800 nm excitation) at pH 4 increases by 8.7 times compared to the value at pH 8, reflecting the difference in the absorption component of extinction. As shown in the combined ultrasound (US) and PA images (**Figure 3.4.2d**), MNP-PANI embedded in phantoms of various pH can be clearly seen though US in the whole pH range, but only become clearly visible at acidic pH for PA imaging.

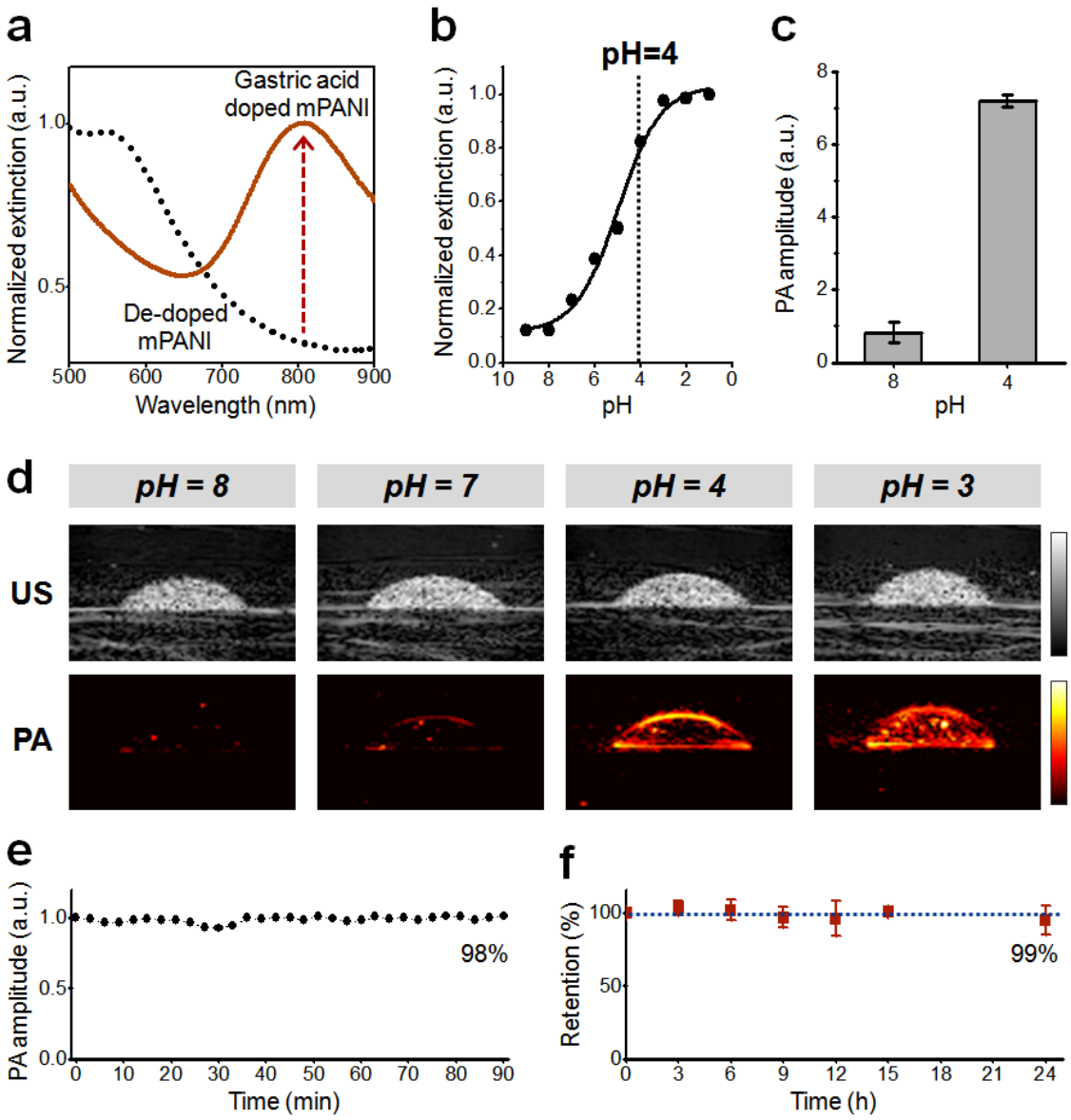


**Figure 3.4.2. Simulated gastric acid doping of MNP-PANI (mPANI). (a)** Extinction spectra of de-doped MNP-PANI (black dotted) and doped with simulated gastric fluid (red solid). **(b & c)** Normalized extinction at 800 nm of MNP-PANI under various pH. Its NIR absorption stays at background level at basic and neutral pH, but increases dramatically toward low pH. The PA signal intensity at pH 4 increases 8.7 folds compared to it at pH 8. **(d)** US and PA images of MNP-PANI embedded phantoms (hemisphere shape) under various pH conditions. **(e)** Normalized PA signal amplitude of gastric acid doped MNP-PANI under pulsed laser irradiation with a laser fluence of 13.7 mJ $cm^{-2}$. **(f)** Retention of MNP-PANI dialyzed in simulated gastric fluid at 37 °C for 24 hours. No appreciable loss of optical extinction was detected.

Next, we investigated the particle stability against intense laser irradiation and low pH. **Figure 3.4.2e** shows that with intense pulsed laser excitation (800 nm, 13.7 mJ $cm^{-2}$), PANI exhibits excellent stability. No PA signal attenuation was observed even after 90 min, significantly more stable than Au nanorods and nanoshells, making long-term imaging and tracking possible.

To assess whether the MNP-PANI nnaoparticles can withstand the harsh condition inside stomach[191], they were dialyzed in simulated gastric fluid. Remarkable, no appreciable loss of optical extinction was detected (**Fig. 3.4.2f**), demonstrating the stability and suitability MNP-PANI as an orally administered contrast agent.

### 3.4.3 MNP-PANI for functional photoacoustic imaging of gastric acid secretion in mouse models

With the MNP-PANI nanoparticles' pH responsiveness and stability confirmed, we proceeded to apply them for functional photoacoustic imaging of gastric acid secretion in mouse models.

First, we explored whether the mouse gastric pH is sufficiently low to enable PANI proton doping, since the mouse stomach pH is generally higher than human. De-doped MNP-PANI (suspended in 150 µl D.I. water) was administered to healthy mice via gavage. A custom-built single-element scanning system was used for acquiring PA images from the scanning area (**Fig. 3.4.3a**).

As shown in **Figure 3.4.3b**, PA imaging revealed the significant signal enhancement before and after MNP-PANI administration. Without MNP-PANI, no contrast was observed from the stomach compared to other organs. In the presence of MNP-PANI, however, a 7.0 fold signal enhancement was observed in the stomach area, whereas the signals from other organs remain unchanged (**Fig. 3.4.3c**), confirming that mouse stomach is sufficiently acidic and is a suitable animal model.

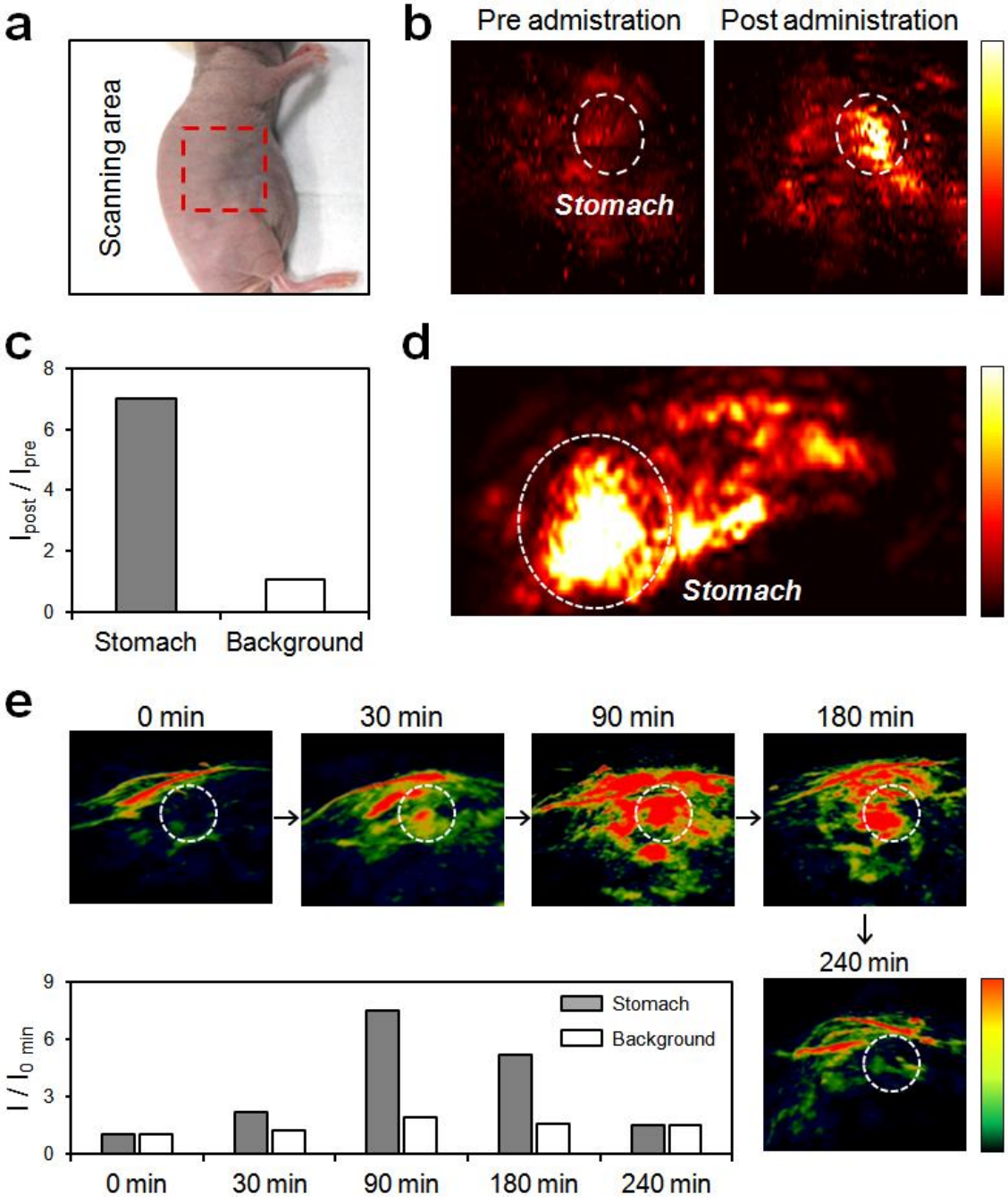


**Figure 3.4.3. MNP-PANI for PA stomach imaging and gastric acid secretory assessment. (a)** The scanning area of mice in PA imaging. **(b)** PA images of the mouse before and after gavage of 0.15 ml de-doped MNP-PANI in water. Circle shows the stomach position. (c) PA intensity enhancement calculation before and after agent administration. Signal is the stomach is enhanced by 7.0 times, but other tissues remain unchanged. **(d)** PA imaging of mice with open abdomen cavity, confirming that the PA signal enhancement is specific to the stomach. **(e)** Gastric acid secretory assessment. PA signal intensity enhancement over time (normalized by signal before particle administration).

To double-check whether the increased signal specifically came from the stomach, mice were sacrificed and imaged again with open abdominal cavity (**Fig. 3.4.3d**).

Indeed, strong PA signals were only observed in the stomach and other organs do not show high PA signals due to the lack of efficient NIR absorbers. To access gastric acid secretion in vivo, MNP-PANI nanoparticles were suspended in sodium bicarbonate solution (150 µl) and administered to healthy mouse via gavage.

An Endra Nexus imaging system was utilized for acquiring data and generating PA images of the scanning area. As shown in the transverse slice in **Figure 3.4.3e**, a series of PA images were acquired at the same location before and after nanoparticle administration at various time points. Quantitative signal intensity analysis was applied to the stomach and surrounding tissue background.

Compared to administering MNP-PANI alone, PA signal enhancement in the stomach area was not observed immediately within first 30 min because neutralization of the alkali challenge takes time. Due to gastric acid re-secretion inside the healthy mouse stomach, the PA signal intensity continuously rose and reached the highest value at around 90 min. Quantitatively, the PA signal enhancement is 7.2 fold, matching the value of administering MNP-PANI without the sodium bicarbonate.

We did not have a mouse model with acid secretion diseases such as achlorhydria and hyperacidity, but we expect that pH restoration process (pH value and time) in these disease models would be much different. It is also worth mentioning that it would take less time for gastric acid re-secretion in human tests. Four hours post nanoparticle administration, the gastric PA signal dropped back to the pre-administration level, indicating complete elimination of the nanoparticles. The particle residence time *in vivo* likely are controlled by the stomach emptying rate as well as nanoparticle interactions with the gastric mucosa[192, 193].

### 3.4.4 Evaluation of its MNP-PANI's potential toxicity effect

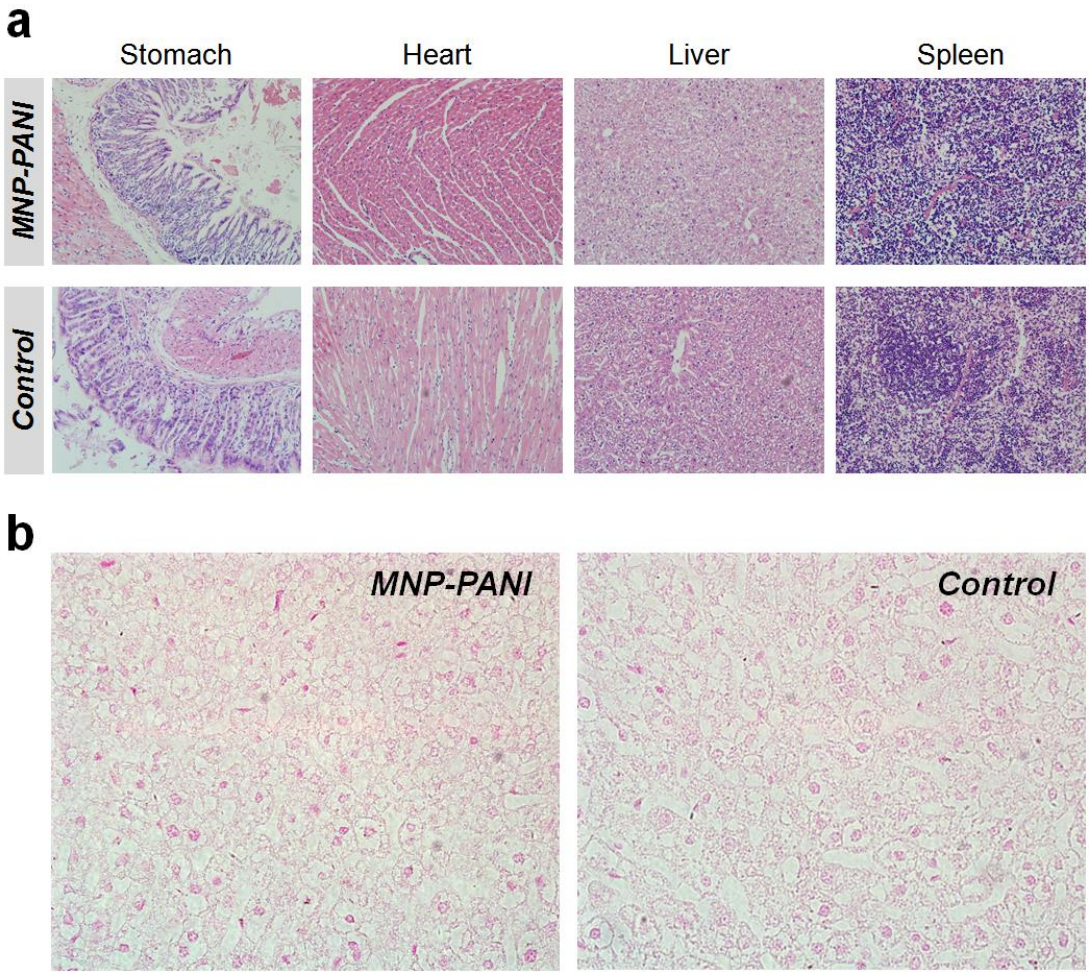


**Figure 3.4.4. Histology assessment of MNP-PANI's potential toxicity after orally administration. (a)** Haematoxylin and eosin stained tissue sections (stomach, heart, liver and spleen) of mice after orally administration of MNP-PANI nanoparticles suspended in sodium bicarbonate solution in comparison with tissues from untreated mice. Gastric pits and glands appear intact without inflammation. **(b)** Iron staining of the tissue sections from liver. No particles are detected compared to the control from untreated mice.

Besides MNP-PANI's performance in acid secretion assessment, we also evaluated its potential toxicity effect. Histology examination of tissues from mice sacrificed 12 hours post nanoparticle administration shows no noticeable inflammatory responses or cell damages in the stomach and other major organs (**Fig. 3.4.4a**). Iron staining of the liver tissue was also conducted, but virtually no nanoparticles were detected, confirming the *in vivo* PA imaging results that nanoparticles are completely eliminated (at least

below PA and microscopy detection limits, **Fig. 3.4.4b**). Note that lack of iron staining is not due to complete dissolving of the iron oxide nanoparticle core. We have observed that even at pH 1, the core etching of MNP-PANI is a very slow process and it takes many days to dissolve the core particle (data not shown).

### 3.4.5 Summary

In summary, we have developed a pH responsive MNP-PANI nanoprobe, and applied it as a PA contract agent for non-invasive functional stomach imaging of gastric acid secretion. In contrast to prior efforts to overcome PANI's doping instability issue, we convert its drawback in pH sensitivity to a unique strength to address an important clinical problem. The structural, spectral, and chemical properties of the core-shell nanoparticles were systematically characterized, and a gastric acid secretory testing protocol simulating current clinical practice was developed for live mouse imaging. These nanometer-sized particles are sufficiently large to avoid passive diffusion through the gastrointestinal mucosa membranes, yet the PANI nanoshell is thin for fast proton diffusion and penetration. Complete nanoparticle elimination after imaging and the absence of systematic toxicity allows potential application of this technology in human, particularly for elderly and infants, to help reduce suffering caused by gastrointestinal intubation. We expect this strategy to be readily extended to other pH sensitive polymers and dye molecules (converting a disadvantage into strength) for functional stomach imaging.

# CHAPTER 4: STIMULATING TOOLS FOR DISEASE INTERVENTION

## 4.1 NANOVESICLES FOR CELL STIMULATION

Untangling the intricacies of biological systems holds a key to comprehension of the fundamentals of life, achieving command over health and disease, and gaining insight into design of novel bio-inspired artificial systems.

Yet, biological systems elude our complete understanding and control, in part due to lack of means for interaction with individual cells within complex cellular networks. For example, optogenetics is capable of controlling cell signaling via precise activation of genetically-modified photosensitive ion channels with light[80, 81], but its translation is hampered by shallow depth of light penetration into tissues and the requirement for gene transfection. Similarly, microelectrodes have been successfully used for stimulation of voltage-gated ion channels[85], but proven exceedingly invasive for *in vivo* use.

Therefore, we posed a question - would it be possible to achieve similar level of cell stimulation precision with a non-invasive remotely activated artificial interface, while overcoming the above-stated limitations? And, more intriguingly, would a newly-established hybrid biological-artificial system exhibit augmented functionality, replacing a pre-existing system with deteriorated or sub-optimal performance?

To start addressing these questions we have applied our extensive expertise in bio-nanotechnology[166] toward engineering of novel ultrasound (US)-responsive nanoparticle-based voltage generators, and propose to develop this nanoacoustic technology into a fully-functional artificial interface for ultrasound-triggered non-invasive deep-tissue *in vivo* cell stimulation (**Fig. 4.1.1**).

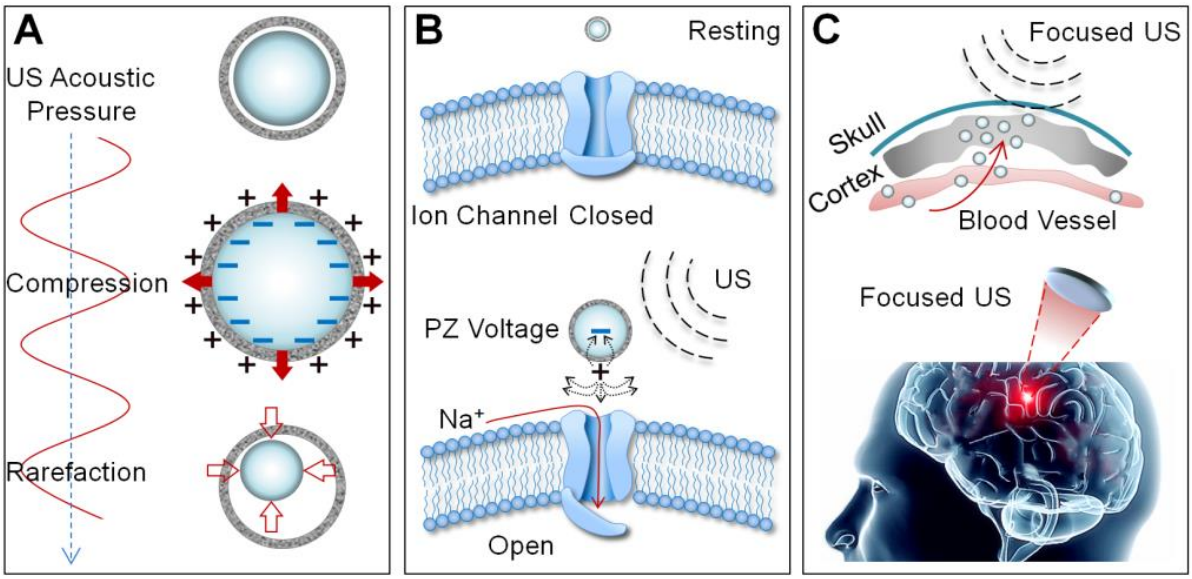


**Figure 4.1.1. Illustration of ultrasound-triggered non-invasive deep-tissue *in vivo* cell stimulation.** **(a)** Charge generation by piezoelectric nano-vesicles under US acoustic wave stimuli. **(b)** US-triggered ion channel electrostimulation at cell membrane. **(c)** Enhanced nano-vesicle delivery, non-invasive brain stimulation and real-time imaging by focused US.

The core of the nanoacoustic technology will be built around novel acoustic-responsive piezoelectric (PZ) nano-vesicles. Being suitable for systemic targeted delivery to specific biological sites, nano-vesicles will form a dynamic acoustic-cell interface and serve as transducers between the non-invasive focused US acoustic stimulation and cell activation. Based on our preliminary work, we propose that gas entrapped inside a nano-vesicle would expand upon acoustic wave propagation, stretching the PZ vesicle wall. Stretching of PZ material yields charge separation and generates electric field, which, when placed next to cell surface, might result in opening of voltage-gated ion channels and cell signaling activation. Therefore, we expect to achieve efficient *in vivo* bioactuation with acoustic waves, while taking advantage of enhanced nano-vesicle delivery and real-time imaging via focused US.

## 4.1.1 Preparation of Piezoelectric (PZ) nano-vesicles

Novel PZ nano-vesicles were fabricated using $BaTiO_3$, an efficient PZ compound. The 200 nm vesicles contained a 50 nm wall and 150 nm inner voids. The vesicle morphology was imaged by TEM, HRTEM,

SEM and STEM. The crystal structure and element profile of these vesicles match the material properties of $BaTiO_3$. **Figure 4.1.2a** shows the TEM images of typical $BaTiO_3$ nano-vehicles with 50 nm walls and 150 nm inner voids. HRTEM shows the corresponding portions of the nanoparticle in TEM image. The distance of 4.03 Å of lattice fringes is indexed to the (001) plane of $BaTiO_3$ with tetragonal phase. The element mapping of single vesicle shows the correct elements distribution. Thus, the PZ nano-vesicles were achieved.

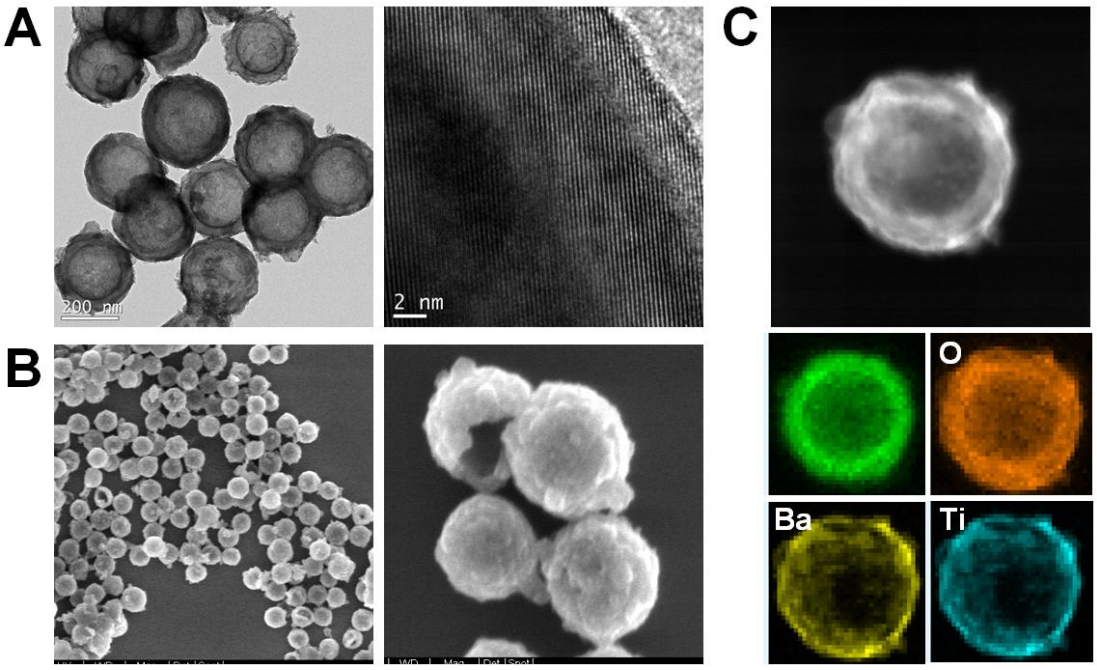


**Figure 4.1.2. Characterization of nano-vesicles. (a)** TEM and HRTEM images of nano-vesicles. **(b)** SEM images of nano-vehicles. **(c)** STEM and element mapping of single nano-vehicle.

## 4.1.2 Evaluation the ultrasound response of gas doped nano-vesicles

The inner voids were further doped with hydrophobic gas. Gas was efficiently trapped inside vesicles through drying and re-dispersion of vesicles into buffer with lipid polyethylene glycol. Remarkably, the gas vesicles feature outstanding stability that gas leakage was not observed even under high hydrostatic pressure (900 KPa, 1 atm). Furthermore, upon focused US stimulation **(Fig. 4.1.2)**, substantial second-

and third-harmonic backscatter generation from nano-vesicles was observed, confirming gas trapping ability and potential US imaging-guided cell modulation.

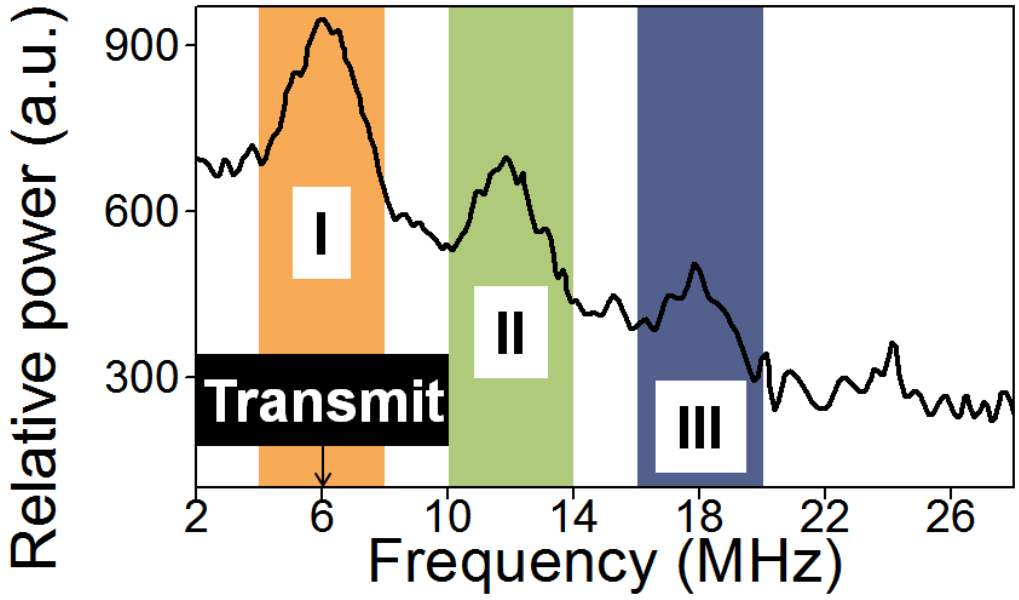


**Figure 4.1.3. Power spectrum of signal backscattered from nano-vesicles in response to 6 MHz transmitted ultrasound pulses.** Orange (I), green (II), and blue (III) shaded areas correspond to frequency bands of harmonic backscatter.

### 4.1.3 Characterization of Piezoelectric (PZ) properties of nano-vesicles

To be noted, we characterized the PZ properties of nano-vesicles, including local polarization switching behavior and PZ coefficient via high sensitive piezoresponse force microscopy. **Figure 4.1.3** shows the local PZ displacement-voltage loop and PZ phase hysteresis on surface the single vesicle. Piezoresponse force microscopy tip was fixed on the vesicle surface and a DC voltage (-10 V to 10 V) was applied during recording piezoresponse signals. **Figure 4.1.3a** shows the typical butterfly loop of ferroelectric $BaTiO_3$. Thus, electrical field of at least 700 mV is expected within 10 nm from vesicle surface based on estimation, which exceeds typical depolarization potential (~10 mV) required to activate resting ion channels. Therefore, we believe the nano-vesicles will generate sufficient electric field to activate cell signaling. Alternative PZ materials and nano-vesicle sizes will be explored should stronger PZ response be required.

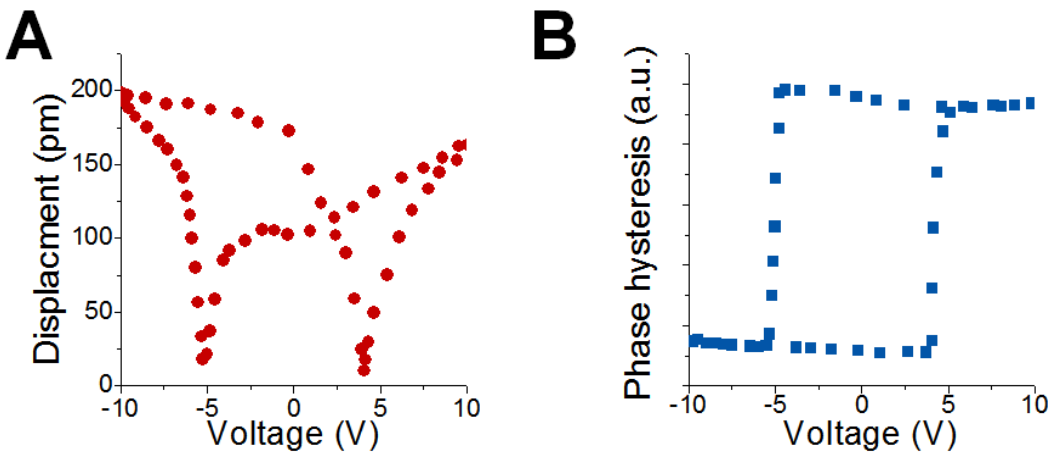


**Figure 4.1.4. Characterization of piezoelectric properties of nano-vesicles. (a)** Local piezoelectric displacement-voltage and **(b)** PZ phase hysteresis profiles on single vesicle surface.

### 4.1.4 *In vitro* cell stimulation

Our results demonstrate that nano-vesicles stimulation by ultrasound is sufficient to illicit activation of a voltage-gated calcium channel in HEK 293 cells. **Figure 4.1.5** shows HEK293 cells transfected with Cav2.1 and incubated with nano-vesicles (300 nm). Upon exposure to ultrasound (600 mV, 7.5 MHz, 10 s), the cells became highly fluorescent due to calcium channel opening (increased $Ca^{2+}$ concentration leads to fluorescence enhancement of intracellular calcium-sensitive dye.

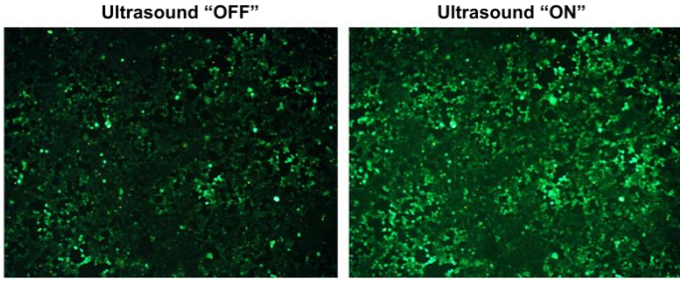


**Figure 4.1.5. $Ca^{2+}$ channel modulation with nano-vesicles.** Cells were treated with nano-vesicles. Fluorescence imaging of $Ca^{2+}$-sensitive dye shows nano-vesicles results in significant fluorescence enhancement upon ultrasound excitation, indicating fast and efficient ion channel modulation.

### 4.1.5 Summary

Novel acoustic-responsive PZ nano-vesicles developed by us will enable, for the first time, to directly perturb individual cells or groups of cells within complex living systems in a non-invasive manner with high spatial and temporal precision. This approach is unique in that it transforms deeply-penetrating acoustic waves into a localized electrical signal, thus turning a widely used non-invasive imaging and therapeutic US technology into a remote actuator of cellular signaling. Nanoparticle design, in turn, synergistically combines the strong acoustic response of nano-bubbles and voltage-generation property of PZ materials to achieve such signal transformation and form an artificial interface for US-triggered cell modulation. Without the requirement of gene transfection, this technology shows great clinical translation potentials.

The breadth of capabilities achieved with nanoacoustic technology will allow exploration of new scientific frontiers in characterization of biological systems, gaining command over cellular signaling, and translation of the results to engineered systems that can potentially solve the national needs. Fully developed and evaluated nanoacoustic technology promises to yield better therapies for such diseases as cancers, Parkinson's, Alzheimer's and drug resistant hypertension[194-196]. This technology will also provide tools for scientists to in situ observe the correlation of neuronal firing with specific brain functions and might be utilized for charge-dependent drug delivery, cardiomyocyte stem cell electromechanical therapy, and non-invasive methods for surgery or puncture[197, 198].

# CHAPTER 5: SUMMARY AND FUTURE DIRECTIONS

In summary, we developed a series of molecular tools for both the scientific discoveries and clinical advancements. This dissertation elaborates on three molecular tools' applications - disease diagnosis, imaging and therapy - towards the healthcare revolution.

First of all, in terms of disease diagnosis, we developed the EASE technique, which can be directly incorporated into the current biology and clinical infrastructure for immediate impact.

The easiness and flexibility of EASE, and its compatibility with the common bioassays (no special reagents or devices needed) have allowed us to show remarkable sensitivity improvements for all the tested assays. We applied EASE to ELISA-based detection of HIV infection in patient blood samples. Our results show that the EASE-enabled ELISA outperforms the standard ELISA by >1,000 times in sensitivity, which translates into detection of 2-3 viruses per 100 µl of blood. We envision that no or only minor developments are needed for broad technology adoption and application, such as early detection of viruses and bacteria without culture, counting disease biomarkers of low abundance, and monitoring treatment responses. Future work will employ new detection assay development, assay condition optimization, and real clinical applications.

Besides the diagnosis sensitivity, we have developed a technically straightforward, yet universally applicable, methodology for eliminating an omnipresent mass transfer limitation in on-surface assays. Highly efficient fluidic exchange and molecular mixing achieved by repeated surface draining and replenishing overcome the fundamental limitations of conventional methods and offer a substantial enhancement in assay kinetics, which makes multi-step or multi-cycle high-content molecular analysis practically useful. We anticipate this method to be incorporated within existing on-surface assays and become an enabling component of novel ultra-rapid technologies for high-content scientific analysis and fast clinical diagnostics. Further optimization of staining conditions is also required for obtaining ultrafast detection. Also, we will transfer this technology to basic and clinical research (e.g., cell transfection, and

fast detection of time-sensitive diseases such as infectious and cardiovascular diseases) and industrial fields (e.g., catalysis on particle surface).

Secondly, in terms of molecular imaging, we have developed a new class of magneto-optical dual functional particles that are compact and uniform in size, NIR light absorbing, and scalable in synthesis. Compared to the conventional gold nanostructure-based NIR absorbers, the MNP/conducting polymer hybrid nanoparticles are significantly more stable against laser irradiation, which is critical for imaging applications involving high-intensity lasers. In parallel, we have also developed a new generation of mmPA technology featuring two key innovations in motion detection, time coherence of displacement with cyclic magnetic excitation and ultrasound-based speckle tracking. In contrast to the first generation mmPA based on the absolute amplitude of magnetic-induced motion, the new system is capable of distinguishing contrast agent movement from physiological motions. Combined, the new imaging probe and cmmPA technology enable the first demonstration of mmPA in live animals, a key step toward ultrasensitive molecular imaging and clinical translation.

Achieving objectives of *in vivo* particle active-binding and detection primarily involve further optimization of nanoparticle targeting property. Improved bio-conjugation is expected to translate directly into improved *in vivo* targeting specificity and sensitivity of tumor detection. Preliminary work in this direction has demonstrated the utility of all proposed methods. Future work will employ careful characterization of each conjugation step to monitor and control reaction progress. Different targeting ligand, such as antibodies, peptides, aptamers, and small-molecule antagonists, will be test for *in vitro* and *in vivo* targeting screening. Spectrophotometry, fluorimetry, and DLS measurements along with functional tests on live cells will be used for this purpose. In particular, successful conjugation should result in increase of nanoparticle hydrodynamic size and shift the population size distribution curve to larger values in DLS data. Furthermore, magnetic nanoparticle staining system enables *in vitro* monitoring of particle binding and uptaking efficiency. Strong NIR absorption exhibited by multifunctional nanoparticles should enable sensitive detection of particle distribution in animal bodies through PA and further efficient therapy.

Last but certainly not least, in terms of disease therapy, we designed a nano-vesicle cell stimulation system. And we prepared and characterized the PZ nano-vesicles. Future work will employ evaluation both *in vitro* and *in vivo* cell stimulation performance of these nano-vesicles. In details, electrostimulation potential of PZ nano-vesicles will be evaluated on voltage-dependent calcium channel ($Ca_v2.1$) as a model, which is a sensitive voltage response ion channel, not respond to either thermal or mechanical triggering. $Ca_v2.1$ proteins will be transfect into neuronal cells without other interfering channels, such as thermal and mechanical responsive channels. Cells without transfection will serve as controls. Nano-vesicles will be functionalized with anti-$Ca_v2.1$ antibody for targeting the $Ca_v2.1$ channels. If weak binding affinity or endocytosis of nano-vesicles is observed, alternative targeting peptides as well as increased vesicle size and surface coating will be explored. Patch-champ will be used to characterize the membrane potential perturbation by nano-vesicles upon exposure to 10 mW/cm² focused US (US safe level is 90 mW/cm²) through monitoring activation of voltage-gated ion channels. Besides of dyes, we will extend this observation to optimize activity monitoring using the genetically encoded calcium indicator GCaMP6m that will translate to our slice and *in vivo* experiments. Note that although the key distinction of our technology over optogenetics is that it does not require genetic transfection. We have chosen to use a genetically encoded calcium indicator for technology development and validation because it is the most efficient means to directly translate *in vitro* observations to our slice and *in vivo* experiments, largely due to the fact that calcium-sensitive dyes are less reliable *in vivo.* To achieve this, HEK 293 cells will be transfected with expression plasmids for Cav2.1 and GCaMP6m. The cell ion channel behaviors will be monitored on a fluorescence microscope in real-time using calcium-sensitive GCaMP6 fluorescence. Data will be analyzed offline using the ImageJ software. Optimal concentration will be determined for bath application of p-bubbles that yield maximal activation (total number of cells showing a response and peak response amplitude) without introducing significant cell death (<5%). The experiment will be tested within at least three different cell samples, and repeated at least three times at different areas on cell plates. We expect to achieve fast on-off ion channel switching upon cyclic acoustic triggering. Voltage-sensitive dye (VSD) imaging will be utilized for monitoring the electrical activity of large populations of neurons *in vivo* with high temporal resolution. High-speed camera will be employed to measure VSD-illuminated electrical activity changes in neurons on the millisecond timescale and with micro-scale spatial resolution.

Alternatively, neuron physiological state will be monitored by simultaneous electroencephalogram recording and extracellular electrode array within the craniotomy. Further, we will assess the utility of our technology as a non-invasive interface for brain control in mice and monkeys for brain function investigation and for neurological disease therapy.

In conclusion, we envision that development and practical implementation of more and more advanced molecular tools will offer exciting opportunities in molecular diagnostics, drug discovery, systems biology, signaling pathway analysis, and gene expression investigations, exploring applications in a wide range of research needs and offering a powerful pathway for advancing both biomedical research and clinical practice.

# Literature Cited


1. Howes, P.D., Chandrawati, R. & Stevens, M.M. Colloidal nanoparticles as advanced biological sensors. *Science* **346**, 1247390 (2014).

2. Chan, W.C. & Nie, S. Quantum dot bioconjugates for ultrasensitive nonisotopic detection. *Science* **281**, 2016-2018 (1998).

3. Kelley, S.O. et al. Advancing the speed, sensitivity and accuracy of biomolecular detection using multi-length-scale engineering. *Nature nanotechnology* **9**, 969-980 (2014).

4. Nam, J.-M., Thaxton, C.S. & Mirkin, C.A. Nanoparticle-based bio-bar codes for the ultrasensitive detection of proteins. *science* **301**, 1884-1886 (2003).

5. Kosaka, P. et al. Detection of cancer biomarkers in serum using a hybrid mechanical and optoplasmonic nanosensor. *Nature nanotechnology* **9**, 1047-1053 (2014).

6. Rodríguez-Lorenzo, L., De La Rica, R., Álvarez-Puebla, R.A., Liz-Marzán, L.M. & Stevens, M.M. Plasmonic nanosensors with inverse sensitivity by means of enzyme-guided crystal growth. *Nature materials* **11**, 604-607 (2012).

7. He, L., Özdemir, Ş.K., Zhu, J., Kim, W. & Yang, L. Detecting single viruses and nanoparticles using whispering gallery microlasers. *Nature nanotechnology* **6**, 428-432 (2011).

8. Thomas, R.K. et al. Sensitive mutation detection in heterogeneous cancer specimens by massively parallel picoliter reactor sequencing. *Nature medicine* **12**, 852-855 (2006).

9. Zheng, G., Patolsky, F., Cui, Y., Wang, W.U. & Lieber, C.M. Multiplexed electrical detection of cancer markers with nanowire sensor arrays. *Nature biotechnology* **23**, 1294-1301 (2005).

10. Wu, G. et al. Bioassay of prostate-specific antigen (PSA) using microcantilevers. *Nature biotechnology* **19**, 856-860 (2001).

11. Schallmeiner, E. et al. Sensitive protein detection via triple-binder proximity ligation assays. *Nature methods* **4**, 135-137 (2007).

12. Watanabe, R. et al. Arrayed lipid bilayer chambers allow single-molecule analysis of membrane transporter activity. *Nature communications* **5** (2014).

13. Ma, W. et al. Attomolar DNA detection with chiral nanorod assemblies. *Nature communications* **4** (2013).

14. Haun, J.B., Devaraj, N.K., Hilderbrand, S.A., Lee, H. & Weissleder, R. Bioorthogonal chemistry amplifies nanoparticle binding and enhances the sensitivity of cell detection. *Nature nanotechnology* **5**, 660-665 (2010).

15. Vollmer, F. & Arnold, S. Whispering-gallery-mode biosensing: label-free detection down to single molecules. *Nature methods* **5**, 591-596 (2008).

16. Li, M., Tang, H.X. & Roukes, M.L. Ultra-sensitive NEMS-based cantilevers for sensing, scanned probe and very high-frequency applications. *Nature nanotechnology* **2**, 114-120 (2007).

17. Cooper, M.A. et al. Direct and sensitive detection of a human virus by rupture event scanning. *Nature biotechnology* **19**, 833-837 (2001).

18. Rissin, D.M. et al. Single-molecule enzyme-linked immunosorbent assay detects serum proteins at subfemtomolar concentrations. *Nature biotechnology* **28**, 595-599 (2010).

19. Burst bubbles. *Nature* **526**, 609-610 (2015).

20. Mitchell, P. A perspective on protein microarrays. *Nature biotechnology* **20**, 225-229 (2002).

21. Cao, Y.C., Jin, R. & Mirkin, C.A. Nanoparticles with Raman spectroscopic fingerprints for DNA and RNA detection. *Science* **297**, 1536-1540 (2002).

22. Cao, Y.C., Jin, R., Nam, J.-M., Thaxton, C.S. & Mirkin, C.A. Raman dye-labeled nanoparticle probes for proteins. *Journal of the American Chemical Society* **125**, 14676-14677 (2003).

23. Liu, Z. et al. Multiplexed five-color molecular imaging of cancer cells and tumor tissues with carbon nanotube Raman tags in the near-infrared. *Nano research* **3**, 222-233 (2010).

24. Chan, Y.-H. et al. Hybrid semiconducting polymer dot–quantum dot with narrow-band emission, near-infrared fluorescence, and high brightness. *Journal of the American Chemical Society* **134**, 7309-7312 (2012).

25. Wu, C. et al. Bioconjugation of ultrabright semiconducting polymer dots for specific cellular targeting. *Journal of the American Chemical Society* **132**, 15410-15417 (2010).

26. Yezhelyev, M.V. et al. In situ molecular profiling of breast cancer biomarkers with multicolor quantum dots. *Advanced Materials* **19**, 3146-3151 (2007).

27. Xing, Y. et al. Bioconjugated quantum dots for multiplexed and quantitative immunohistochemistry. *Nature protocols* **2**, 1152-1165 (2007).

28. Zrazhevskiy, P. & Gao, X. Quantum dot imaging platform for single-cell molecular profiling. *Nature communications* **4**, 1619 (2013).

29. Angelo, M. et al. Multiplexed ion beam imaging of human breast tumors. *Nature medicine* **20**, 436-442 (2014).

30. Giesen, C. et al. Highly multiplexed imaging of tumor tissues with subcellular resolution by mass cytometry. *Nature methods* **11**, 417-422 (2014).

31. Siegel, R., Ma, J., Zou, Z. & Jemal, A. Cancer statistics, 2014. *CA: a cancer journal for clinicians* **64**, 9-29 (2014).

32. Weissleder, R. A clearer vision for in vivo imaging. *Nature biotechnology* **19**, 316-316 (2001).

33. Zrazhevskiy, P. & Gao, X. Multifunctional quantum dots for personalized medicine. *Nano today* **4**, 414-428 (2009).

34. Zrazhevskiy, P., Sena, M. & Gao, X. Designing multifunctional quantum dots for bioimaging, detection, and drug delivery. *Chemical Society Reviews* **39**, 4326-4354 (2010).

35. Feng, G., Ding, D. & Liu, B. Fluorescence bioimaging with conjugated polyelectrolytes. *Nanoscale* **4**, 6150-6165 (2012).

36. Pu, K.Y. & Liu, B. Fluorescent conjugated polyelectrolytes for bioimaging. *Advanced Functional Materials* **21**, 3408-3423 (2011).

37. Choi, H.S. et al. Renal clearance of quantum dots. *Nature biotechnology* **25**, 1165-1170 (2007).

38. Nel, A., Xia, T., Mädler, L. & Li, N. Toxic potential of materials at the nanolevel. *science* **311**, 622-627 (2006).

39. Zhao, Q. et al. Aggregation-induced red-NIR emission organic nanoparticles as effective and photostable fluorescent probes for bioimaging. *Journal of Materials Chemistry* **22**, 15128-15135 (2012).

40. Jin, Y., Jia, C., Huang, S.-W., O'Donnell, M. & Gao, X. Multifunctional nanoparticles as coupled contrast agents. *Nature communications* **1**, 41 (2010).

41. Duan, X., Liu, L., Feng, F. & Wang, S. Cationic conjugated polymers for optical detection of DNA methylation, lesions, and single nucleotide polymorphisms. *Accounts of chemical research* **43**, 260-270 (2009).

42. Thomas, S.W., Joly, G.D. & Swager, T.M. Chemical sensors based on amplifying fluorescent conjugated polymers. *Chemical reviews* **107**, 1339-1386 (2007).

43. Burroughes, J. et al. Light-emitting diodes based on conjugated polymers. *nature* **347**, 539-541 (1990).

44. Ding, D. et al. Conjugated polyelectrolyte–cisplatin complex nanoparticles for simultaneous in vivo imaging and drug tracking. *Nanoscale* **3**, 1997-2002 (2011).

45. Friend, R. et al. Electroluminescence in conjugated polymers. *Nature* **397**, 121-128 (1999).

46. Moon, J.H., Mendez, E., Kim, Y. & Kaur, A. Conjugated polymer nanoparticles for small interfering RNA delivery. *Chemical Communications* **47**, 8370-8372 (2011).

47. Pecher, J., Huber, J., Winterhalder, M., Zumbusch, A. & Mecking, S. Tailor-made conjugated polymer nanoparticles for multicolor and multiphoton cell imaging. *Biomacromolecules* **11**, 2776-2780 (2010).

48. Rehmann, N. et al. Advanced Device Architecture for Highly Efficient Organic Light-Emitting Diodes with an Orange-Emitting Crosslinkable Iridium (III) Complex. *Advanced Materials* **20**, 129-133 (2008).

49. Wu, C., Bull, B., Szymanski, C., Christensen, K. & McNeill, J. Multicolor conjugated polymer dots for biological fluorescence imaging. *ACS nano* **2**, 2415-2423 (2008).

50. Wu, C., Szymanski, C., Cain, Z. & McNeill, J. Conjugated polymer dots for multiphoton fluorescence imaging. *Journal of the American Chemical Society* **129**, 12904-12905 (2007).

51. Zhu, C., Yang, Q., Lv, F., Liu, L. & Wang, S. Conjugated Polymer-Coated Bacteria for Multimodal Intracellular and Extracellular Anticancer Activity. *Advanced Materials* **25**, 1203-1208 (2013).

52. Liu, B. & Bazan, G.C. Homogeneous fluorescence-based DNA detection with water-soluble conjugated polymers. *Chemistry of materials* **16**, 4467-4476 (2004).

53. Duarte, A., Pu, K.-Y., Liu, B. & Bazan, G.C. Recent advances in conjugated polyelectrolytes for emerging optoelectronic applications. *Chemistry of Materials* **23**, 501-515 (2010).

54. Li, K. & Liu, B. Polymer encapsulated conjugated polymer nanoparticles for fluorescence bioimaging. *Journal of Materials Chemistry* **22**, 1257-1264 (2012).

55. Wu, C. & Chiu, D.T. Highly fluorescent semiconducting polymer dots for biology and medicine. *Angewandte Chemie International Edition* **52**, 3086-3109 (2013).

56. Wegner, G. Polymers with Metal-Like Conductivity—A Review of their Synthesis, Structure and Properties. *Angewandte Chemie International Edition* **20**, 361-381 (1981).

57. Patil, A., Heeger, A. & Wudl, F. Optical properties of conducting polymers. *Chemical Reviews* **88**, 183-200 (1988).

58. Drury, C., Mutsaers, C., Hart, C., Matters, M. & De Leeuw, D. Low-cost all-polymer integrated circuits. *Applied Physics Letters* **73**, 108-110 (1998).

59. Lim, J.H. & Mirkin, C.A. Electrostatically Driven Dip-Pen Nanolithography of Conducting Polymers. *Advanced Materials* **14**, 1474-1477 (2002).

60. Janata, J. & Josowicz, M. Conducting polymers in electronic chemical sensors. *Nature materials* **2**, 19-24 (2003).

61. Tran, H.D., Li, D. & Kaner, R.B. One-Dimensional Conducting Polymer Nanostructures: Bulk Synthesis and Applications. *Advanced Materials* **21**, 1487-1499 (2009).

62. Li, C., Bai, H. & Shi, G. Conducting polymer nanomaterials: electrosynthesis and applications. *Chemical Society Reviews* **38**, 2397-2409 (2009).

63. Pan, L. et al. Hierarchical nanostructured conducting polymer hydrogel with high electrochemical activity. *Proceedings of the National Academy of Sciences* **109**, 9287-9292 (2012).

64. Silva, R., Voiry, D., Chhowalla, M. & Asefa, T. Efficient metal-free electrocatalysts for oxygen reduction: polyaniline-derived N-and O-doped mesoporous carbons. *Journal of the American Chemical Society* **135**, 7823-7826 (2013).

65. Li, J. et al. Emerging applications of conjugated polymers in molecular imaging. *Physical Chemistry Chemical Physics* **15**, 17006-17015 (2013).

66. Li, J. et al. Magneto-optical nanoparticles for cyclic magnetomotive photoacoustic imaging. *ACS nano* **9**, 1964-1976 (2015).

67. Yang, J. et al. Convertible Organic Nanoparticles for Near-Infrared Photothermal Ablation of Cancer Cells. *Angewandte Chemie* **123**, 461-464 (2011).

68. Zhou, J. et al. NIR photothermal therapy using polyaniline nanoparticles. *Biomaterials* **34**, 9584-9592 (2013).

69. Cheng, L., Wang, C., Feng, L., Yang, K. & Liu, Z. Functional nanomaterials for phototherapies of cancer. *Chem. Rev* **114**, 10869-10939 (2014).

70. Chen, S.-A. & Hwang, G.-W. Synthesis of water-soluble self-acid-doped polyaniline. *Journal of the American Chemical Society* **116**, 7939-7940 (1994).

71. Ma, Y. et al. In situ fabrication of a water-soluble, self-doped polyaniline nanocomposite: the unique role of DNA functionalized single-walled carbon nanotubes. *Journal of the American Chemical Society* **128**, 12064-12065 (2006).

72. McVerry, B.T. et al. Fabrication of low-fouling ultrafiltration membranes using a hydrophilic, self-doping polyaniline additive. *Chemistry of Materials* **25**, 3597-3602 (2013).

73. Peery, A.F. et al. Burden of gastrointestinal disease in the United States: 2012 update. *Gastroenterology* **143**, 1179-1187. e1173 (2012).

74. Kwiecien, S. et al. The role of reactive oxygen species and capsaicin-sensitive sensory nerves in the pathomechanism of gastric ulcers induced by stress. *Journal of Physiology and pharmacology* **54**, 423-437 (2003).

75. Ghosh, T., Lewis, D.I., Axon, A. & Everett, S. methods of measuring gastric acid secretion. *Alimentary pharmacology & therapeutics* **33**, 768-781 (2011).

76. Johnston, D. & Jepson, K. Use of pentagastrin in a test of gastric acid secretion. *The Lancet* **290**, 585-588 (1967).

77. Wang, L.V. & Hu, S. Photoacoustic tomography: in vivo imaging from organelles to organs. *Science* **335**, 1458-1462 (2012).

78. Zhang, Y. et al. Non-invasive multimodal functional imaging of the intestine with frozen micellar naphthalocyanines. *Nature nanotechnology* **9**, 631-638 (2014).

79. Wang, Y. et al. Photoacoustic tomography of a nanoshell contrast agent in the in vivo rat brain. *Nano Letters* **4**, 1689-1692 (2004).

80. Deisseroth, K. Optogenetics. *Nature methods* **8**, 26-29 (2011).

81. Boyden, E.S., Zhang, F., Bamberg, E., Nagel, G. & Deisseroth, K. Millisecond-timescale, genetically targeted optical control of neural activity. *Nature neuroscience* **8**, 1263-1268 (2005).

82. Adamantidis, A.R., Zhang, F., Aravanis, A.M., Deisseroth, K. & De Lecea, L. Neural substrates of awakening probed with optogenetic control of hypocretin neurons. *Nature* **450**, 420-424 (2007).

83. Petreanu, L., Huber, D., Sobczyk, A. & Svoboda, K. Channelrhodopsin-2–assisted circuit mapping of long-range callosal projections. *Nature neuroscience* **10**, 663-668 (2007).

84. Gradinaru, V. et al. Molecular and cellular approaches for diversifying and extending optogenetics. *Cell* **141**, 154-165 (2010).

85. Nguyen, J.-P., Nizard, J., Keravel, Y. & Lefaucheur, J.-P. Invasive brain stimulation for the treatment of neuropathic pain. *Nature Reviews Neurology* **7**, 699-709 (2011).

86. Lee, H., Dellatore, S.M., Miller, W.M. & Messersmith, P.B. Mussel-inspired surface chemistry for multifunctional coatings. *science* **318**, 426-430 (2007).

87. Lee, H., Rho, J. & Messersmith, P.B. Facile conjugation of biomolecules onto surfaces via mussel adhesive protein inspired coatings. *Advanced Materials* **21**, 431-434 (2009).

88. Söderhäll, K. & Cerenius, L. Role of the prophenoloxidase-activating system in invertebrate immunity. *Current opinion in immunology* **10**, 23-28 (1998).

89. Cerenius, L. & Söderhäll, K. The prophenoloxidase-activating system in invertebrates. *Immunological reviews* **198**, 116-126 (2004).

90. Weber, R. et al. Threshold of detection of Cryptosporidium oocysts in human stool specimens: evidence for low sensitivity of current diagnostic methods. *Journal of Clinical Microbiology* **29**, 1323-1327 (1991).

91. Mahler, M., Ngo, J.T., Schulte-Pelkum, J., Luettich, T. & Fritzler, M.J. Limited reliability of the indirect immunofluorescence technique for the detection of anti-Rib-P antibodies. *Arthritis research & therapy* **10**, R131 (2008).

92. Medintz, I.L., Uyeda, H.T., Goldman, E.R. & Mattoussi, H. Quantum dot bioconjugates for imaging, labelling and sensing. *Nature materials* **4**, 435-446 (2005).

93. Zrazhevskiy, P. et al. Cross-Platform DNA Encoding for Single-Cell Imaging of Gene Expression. *Angewandte Chemie International Edition* **55**, 8975-8978 (2016).

94. Battersby, B.J., Lawrie, G.A. & Trau, M. Optical encoding of microbeads for gene screening: alternatives to microarrays. *Drug Discovery Today* **6**, 19-26 (2001).

95. Braeckmans, K., De Smedt, S.C., Leblans, M., Pauwels, R. & Demeester, J. Encoding microcarriers: present and future technologies. *Nature Reviews Drug Discovery* **1**, 447-456 (2002).

96. Nolan, J.P. & Sklar, L.A. Suspension array technology: evolution of the flat-array paradigm. *TRENDS in Biotechnology* **20**, 9-12 (2002).

97. Fulton, R.J., McDade, R.L., Smith, P.L., Kienker, L.J. & Kettman, J.R. Advanced multiplexed analysis with the FlowMetrixTM system. *Clinical chemistry* **43**, 1749-1756 (1997).

98. Dunbar, S.A. Applications of Luminex® xMAP™ technology for rapid, high-throughput multiplexed nucleic acid detection. *Clinica chimica acta* **363**, 71-82 (2006).

99. Chan, W.C. et al. Luminescent quantum dots for multiplexed biological detection and imaging. *Current opinion in biotechnology* **13**, 40-46 (2002).

100. Han, M., Gao, X., Su, J.Z. & Nie, S. Quantum-dot-tagged microbeads for multiplexed optical coding of biomolecules. *Nature biotechnology* **19**, 631-635 (2001).

101. Klein, D., Hurley, L.B., Merrill, D. & Quesenberry Jr, C.P. Review of medical encounters in the 5 years before a diagnosis of HIV-1 infection: implications for early detection. *JAIDS Journal of Acquired Immune Deficiency Syndromes* **32**, 143-152 (2003).

102. Fu, E. et al. Enhanced sensitivity of lateral flow tests using a two-dimensional paper network format. *Analytical chemistry* **83**, 7941-7946 (2011).

103. Palella, F.J. et al. Survival benefit of initiating antiretroviral therapy in HIV-infected persons in different CD4+ cell strata. *Annals of internal medicine* **138**, 620-626 (2003).

104. Holodniy, M. et al. Relationship between antiretroviral prescribing patterns and treatment guidelines in treatment-naive HIV-1-infected US veterans (1992-2004). *JAIDS Journal of Acquired Immune Deficiency Syndromes* **44**, 20-29 (2007).

105. Marks, G., Crepaz, N. & Janssen, R.S. Estimating sexual transmission of HIV from persons aware and unaware that they are infected with the virus in the USA. *Aids* **20**, 1447-1450 (2006).

106. Miles, S.A. et al. Rapid serologic testing with immune-complex-dissociated HIV p24 antigen for early detection of HIV infection in neonates. *New England Journal of Medicine* **328**, 297-302 (1993).

107. Nishanian, P., Huskins, K.R., Stehn, S., Detels, R. & Fahey, J.L. A simple method for improved assay demonstrates that HIV p24 antigen is present as immune complexes in most sera from HIV-infected individuals. *Journal of Infectious Diseases* **162**, 21-28 (1990).

108. Marozsan, A.J. et al. Relationships between infectious titer, capsid protein levels, and reverse transcriptase activities of diverse human immunodeficiency virus type 1 isolates. *Journal of virology* **78**, 11130-11141 (2004).

109. Bale, T.L. & Vale, W.W. CRF and CRF receptors: role in stress responsivity and other behaviors. *Annu. Rev. Pharmacol. Toxicol.* **44**, 525-557 (2004).

110. Zorrilla, E.P., Logrip, M.L. & Koob, G.F. Corticotropin releasing factor: a key role in the neurobiology of addiction. *Frontiers in neuroendocrinology* **35**, 234-244 (2014).

111. Van Pett, K. et al. Distribution of mRNAs encoding CRF receptors in brain and pituitary of rat and mouse. *Journal of Comparative Neurology* **428**, 191-212 (2000).

112. Weathington, J.M. & Cooke, B.M. Corticotropin-releasing factor receptor binding in the amygdala changes across puberty in a sex-specific manner. *Endocrinology* **153**, 5701-5705 (2012).

113. Waldorf, K.M.A. et al. Fetal brain lesions after subcutaneous inoculation of Zika virus in a pregnant nonhuman primate. *Nature medicine* **22**, 1256-1259 (2016).

114. Keir, M.E., Butte, M.J., Freeman, G.J. & Sharpe, A.H. PD-1 and its ligands in tolerance and immunity. *Annu. Rev. Immunol.* **26**, 677-704 (2008).

115. Brahmer, J.R. et al. Phase I study of single-agent anti–programmed death-1 (MDX-1106) in refractory solid tumors: safety, clinical activity, pharmacodynamics, and immunologic correlates. *Journal of clinical oncology* **28**, 3167-3175 (2010).

116. Hamid, O. et al. Safety and tumor responses with lambrolizumab (anti–PD-1) in melanoma. *N Engl J Med* **2013**, 134-144 (2013).

117. Garon, E.B. et al. Pembrolizumab for the treatment of non–small-cell lung cancer. *New England Journal of Medicine* **372**, 2018-2028 (2015).

118. Rizvi, N.A. et al. Activity and safety of nivolumab, an anti-PD-1 immune checkpoint inhibitor, for patients with advanced, refractory squamous non-small-cell lung cancer (CheckMate 063): a phase 2, single-arm trial. *The Lancet Oncology* **16**, 257-265 (2015).

119. Nghiem, P.T. et al. PD-1 blockade with pembrolizumab in advanced Merkel-cell carcinoma. *New England Journal of Medicine* **374**, 2542-2552 (2016).

120. Wang, X., Teng, F., Kong, L. & Yu, J. PD-L1 expression in human cancers and its association with clinical outcomes. *OncoTargets and therapy* **9**, 5023 (2016).

121. Liu, Y., Ai, K. & Lu, L. Polydopamine and its derivative materials: synthesis and promising applications in energy, environmental, and biomedical fields. *Chemical reviews* **114**, 5057-5115 (2014).

122. Li, J. et al. Stably doped conducting polymer nanoshells by surface initiated polymerization. *Nano letters* **15**, 8217-8222 (2015).

123. Canziani, G.A., Klakamp, S. & Myszka, D.G. Kinetic screening of antibodies from crude hybridoma samples using Biacore. *Analytical biochemistry* **325**, 301-307 (2004).

124. Pappaert, K., Van Hummelen, P., Vanderhoeven, J., Baron, G. & Desmet, G. Diffusion–reaction modelling of DNA hybridization kinetics on biochips. *Chemical Engineering Science* **58**, 4921-4930 (2003).

125. Stenberg, M. & Nygren, H. Kinetics of antigen-antibody reactions at solid-liquid interfaces. *Journal of Immunological Methods* **113**, 3-15 (1988).

126. Gerdes, M.J. et al. Highly multiplexed single-cell analysis of formalin-fixed, paraffin-embedded cancer tissue. *Proceedings of the National Academy of Sciences* **110**, 11982-11987 (2013).

127. Micheva, K.D. & Smith, S.J. Array tomography: a new tool for imaging the molecular architecture and ultrastructure of neural circuits. *Neuron* **55**, 25-36 (2007).

128. Schubert, W. et al. Analyzing proteome topology and function by automated multidimensional fluorescence microscopy. *Nature biotechnology* **24**, 1270-1278 (2006).

129. Stack, E.C., Wang, C., Roman, K.A. & Hoyt, C.C. Multiplexed immunohistochemistry, imaging, and quantitation: a review, with an assessment of Tyramide signal amplification, multispectral imaging and multiplex analysis. *Methods* **70**, 46-58 (2014).

130. Ng, A.H., Uddayasankar, U. & Wheeler, A.R. Immunoassays in microfluidic systems. *Analytical and bioanalytical chemistry* **397**, 991-1007 (2010).

131. Glaser, R.W. Antigen-antibody binding and mass transport by convection and diffusion to a surface: a two-dimensional computer model of binding and dissociation kinetics. *Analytical biochemistry* **213**, 152-161 (1993).

132. Karlsson, R., Roos, H., Fägerstam, L. & Persson, B. Kinetic and concentration analysis using BIA technology. *Methods* **6**, 99-110 (1994).

133. Yoon, S.K., Fichtl, G.W. & Kenis, P.J. Active control of the depletion boundary layers in microfluidic electrochemical reactors. *Lab on a Chip* **6**, 1516-1524 (2006).

134. Liu, J., Williams, B.A., Gwirtz, R.M., Wold, B.J. & Quake, S. Enhanced signals and fast nucleic acid hybridization by microfluidic chaotic mixing. *Angewandte Chemie* **118**, 3700-3705 (2006).

135. Erickson, D., Liu, X., Krull, U. & Li, D. Electrokinetically controlled DNA hybridization microfluidic chip enabling rapid target analysis. *Analytical Chemistry* **76**, 7269-7277 (2004).

136. Morozov, V.N., Groves, S., Turell, M.J. & Bailey, C. Three minutes-long electrophoretically assisted zeptomolar microfluidic immunoassay with magnetic-beads detection. *Journal of the American Chemical Society* **129**, 12628-12629 (2007).

137. Cheek, B.J., Steel, A.B., Torres, M.P., Yu, Y.-Y. & Yang, H. Chemiluminescence detection for hybridization assays on the flow-thru chip, a three-dimensional microchannel biochip. *Analytical Chemistry* **73**, 5777-5783 (2001).

138. Ciftlik, A.T., Lehr, H.-A. & Gijs, M.A. Microfluidic processor allows rapid HER2 immunohistochemistry of breast carcinomas and significantly reduces ambiguous (2+) read-outs. *Proceedings of the National Academy of Sciences* **110**, 5363-5368 (2013).

139. Hatta, H., Tsuneyama, K., Kondo, T. & Takano, Y. Development of an ultrasound-emitting device for performing rapid immunostaining procedures. *Journal of Histochemistry & Cytochemistry* **58**, 421-428 (2010).

140. Long, D.J. & Buggs, C. Microwave oven-based technique for immunofluorescent staining of paraffin-embedded tissues. *Journal of molecular histology* **39**, 1-4 (2008).

141. Chang, K.H. et al. Novel 16-minute technique for evaluating melanoma resection margins during Mohs surgery. *Journal of the American Academy of Dermatology* **64**, 107-112 (2011).

142. Hulme, E.C. & Trevethick, M.A. Ligand binding assays at equilibrium: validation and interpretation. *British journal of pharmacology* **161**, 1219-1237 (2010).

143. Liu, J. et al. Molecular mapping of tumor heterogeneity on clinical tissue specimens with multiplexed quantum dots. *ACS nano* **4**, 2755-2765 (2010).

144. Zrazhevskiy, P., True, L.D. & Gao, X. Multicolor multicycle molecular profiling with quantum dots for single-cell analysis. *Nature protocols* **8**, 1852-1869 (2013).

145. Friedenberger, M., Bode, M., Krusche, A. & Schubert, W. Fluorescence detection of protein clusters in individual cells and tissue sections by using toponome imaging system: sample preparation and measuring procedures. *Nature protocols* **2**, 2285-2294 (2007).

146. Gal, A.A. & Cagle, P.T. The 100-year anniversary of the description of the frozen section procedure. *Jama* **294**, 3135-3137 (2005).

147. Diekema, D.J. & Pfaller, M.A. Rapid detection of antibiotic-resistant organism carriage for infection prevention. *Clinical infectious diseases* **56**, 1614-1620 (2013).

148. Caliendo, A.M. et al. Better tests, better care: improved diagnostics for infectious diseases. *Clinical Infectious Diseases* **57**, S139-S170 (2013).

149. Luo, D. & Saltzman, W.M. Enhancement of transfection by physical concentration of DNA at the cell surface. *Nature biotechnology* **18**, 893-895 (2000).

150. Mehrmohammadi, M. et al. Pulsed magneto-motive ultrasound imaging to detect intracellular accumulation of magnetic nanoparticles. *Nanotechnology* **22**, 415105 (2011).

151. Zhu, C.-L., Chou, S.-W., He, S.-F., Liao, W.-N. & Chen, C.-C. Synthesis of core/shell metal oxide/polyaniline nanocomposites and hollow polyaniline capsules. *Nanotechnology* **18**, 275604 (2007).

152. Lu, X., Mao, H. & Zhang, W. Fabrication of core-shell Fe3O4/polypyrrole and hollow polypyrrole microspheres. *Polymer Composites* **30**, 847-854 (2009).

153. Jiang, W., Kim, B.Y., Rutka, J.T. & Chan, W.C. Nanoparticle-mediated cellular response is size-dependent. *Nature nanotechnology* **3**, 145-150 (2008).

154. Cabral, H. et al. Accumulation of sub-100 nm polymeric micelles in poorly permeable tumours depends on size. *Nature nanotechnology* **6**, 815-823 (2011).

155. Wang, C. et al. Iron oxide@ polypyrrole nanoparticles as a multifunctional drug carrier for remotely controlled cancer therapy with synergistic antitumor effect. *ACS nano* **7**, 6782-6795 (2013).

156. Dey, A., De, A. & De, S. Electrical transport and dielectric relaxation in Fe3O4–polypyrrole hybrid nanocomposites. *Journal of Physics: Condensed Matter* **17**, 5895 (2005).

157. Brezoi, D.-V. & Ion, R.-M. Phase evolution induced by polypyrrole in iron oxide–polypyrrole nanocomposite. *Sensors and Actuators B: Chemical* **109**, 171-175 (2005).

158. Chen, A., Wang, H., Zhao, B. & Li, X. The preparation of polypyrrole–Fe3O4 nanocomposites by the use of common ion effect. *Synthetic Metals* **139**, 411-415 (2003).

159. Wuang, S.C., Neoh, K.G., Kang, E.-T., Pack, D.W. & Leckband, D.E. Synthesis and functionalization of polypyrrole-Fe 3 O 4 nanoparticles for applications in biomedicine. *Journal of Materials Chemistry* **17**, 3354-3362 (2007).

160. Zhang, H., Zhong, X., Xu, J.-J. & Chen, H.-Y. Fe3O4/polypyrrole/Au nanocomposites with core/shell/shell structure: synthesis, characterization, and their electrochemical properties. *Langmuir* **24**, 13748-13752 (2008).

161. Zhang, Z. et al. Highly conductive polypyrrole/γ-Fe2O3 nanospheres with good magnetic properties obtained through an improved chemical one-step method. *Macromolecules* **44**, 4610-4615 (2011).

162. Sun, Z., Geng, Y., Li, J., Jing, X. & Wang, F. Chemical polymerization of aniline with hydrogen peroxide as oxidant. *Synthetic metals* **84**, 99-100 (1997).

163. Sun, H. et al. Measuring the unusually slow ionic diffusion in polyaniline via study of yolk-shell nanostructures. *Journal of the American Chemical Society* **134**, 11243-11250 (2012).

164. Gill, M. et al. A study of the kinetics of polymerization of aniline using proton NMR spectroscopy. *Synthetic metals* **93**, 227-233 (1998).

165. Kudoh, Y. Properties of polypyrrole prepared by chemical polymerization using aqueous solution containing Fe 2 (SO 4) 3 and anionic surfactant. *Synthetic metals* **79**, 17-22 (1996).

166. Gao, X., Cui, Y., Levenson, R.M., Chung, L.W. & Nie, S. In vivo cancer targeting and imaging with semiconductor quantum dots. *Nature biotechnology* **22**, 969 (2004).

167. Manceau, M. et al. Photochemical stability of π-conjugated polymers for polymer solar cells: a rule of thumb. *Journal of Materials Chemistry* **21**, 4132-4141 (2011).

168. O'Donnell, M., Skovoroda, A.R., Shapo, B.M. & Emelianov, S.Y. Internal displacement and strain imaging using ultrasonic speckle tracking. *IEEE transactions on ultrasonics, ferroelectrics, and frequency control* **41**, 314-325 (1994).

169. Qu, M. et al. Magneto-photo-acoustic imaging. *Biomedical optics express* **2**, 385-396 (2011).

170. Meyskens, F.L., Thomson, S.P. & Moon, T.E. Quantitation of the number of cells within tumor colonies in semisolid medium and their growth as oblate spheroids. *Cancer research* **44**, 271-277 (1984).

171. Xing, S. et al. Highly controlled core/shell structures: tunable conductive polymer shells on gold nanoparticles and nanochains. *Journal of Materials Chemistry* **19**, 3286-3291 (2009).

172. Fu, G., Zhao, J., Sun, Y., Kang, E. & Neoh, K. Conductive hollow nanospheres of polyaniline via surface-initiated atom transfer radical polymerization of 4-vinylaniline and oxidative graft copolymerization of aniline. *Macromolecules* **40**, 2271-2275 (2007).

173. Wu, T., Zhang, Y., Wang, X. & Liu, S. Fabrication of hybrid silica nanoparticles densely grafted with thermoresponsive poly (N-isopropylacrylamide) brushes of controlled thickness via surface-initiated atom transfer radical polymerization. *Chemistry of Materials* **20**, 101-109 (2007).

174. Dong, H. et al. One-pot synthesis of robust core/shell gold nanoparticles. *Journal of the American Chemical Society* **130**, 12852-12853 (2008).

175. Zhao, B. & Zhu, L. Mixed polymer brush-grafted particles: a new class of environmentally responsive nanostructured materials. *Macromolecules* **42**, 9369-9383 (2009).

176. Lyatskaya, Y.V., Leermakers, F., Fleer, G., Zhulina, E. & Birshtein, T. Analytical self-consistent-field model of weak polyacid brushes. *Macromolecules* **28**, 3562-3569 (1995).

177. Zhulina, E., Birshtein, T. & Borisov, O. Theory of ionizable polymer brushes. *Macromolecules* **28**, 1491-1499 (1995).

178. Cao, Z. & Jiang, S. Super-hydrophilic zwitterionic poly (carboxybetaine) and amphiphilic non-ionic poly (ethylene glycol) for stealth nanoparticles. *Nano Today* **7**, 404-413 (2012).

179. Feneley, M. et al. Imaging with prostate-specific membrane antigen (PSMA) in prostate cancer. *Prostate cancer and prostatic diseases* **3**, 47 (2000).

180. Kwiecien, S. & Konturek, S. GASTRIC ANALYSIS WITH FRACTIONAL TEST MEALS (ETHANOL. *Journal of physiology and pharmacology* **54**, 69-82 (2003).

181. A. van Herwaarden, M.S., AJPM Smout, M 24-h recording of intragastric pH: technical aspects and clinical relevance. *Scandinavian Journal of Gastroenterology* **34**, 9-16 (1999).

182. Chang, J.H. et al. A novel placement method of the Bravo wireless pH monitoring capsule for measuring intragastric pH. *Digestive diseases and sciences* **54**, 578-585 (2009).

183. Baxter, A. et al. Evaluation of applied potential tomography as a new non-invasive gastric secretion test. *Gut* **29**, 1730-1735 (1988).

184. Passaro, D., Hurwitz, A., Triadafilopoulos, G. & Parsonnet, J. A modification of the quininium resin test for assessing gastric acidity. *Alimentary pharmacology & therapeutics* **16**, 875-880 (2002).

185. Fan, Q. et al. Perylene-Diimide-Based Nanoparticles as Highly Efficient Photoacoustic Agents for Deep Brain Tumor Imaging in Living Mice. *Advanced Materials* **27**, 843-847 (2015).

186. Dinish, U. et al. Single molecule with dual function on nanogold: biofunctionalized construct for in vivo photoacoustic imaging and SERS biosensing. *Advanced Functional Materials* **25**, 2316-2325 (2015).

187. Bayer, C.L., Luke, G.P. & Emelianov, S.Y. Photoacoustic imaging for medical diagnostics. *Acoustics today* **8**, 15 (2012).

188. Lu, W. et al. Photoacoustic imaging of living mouse brain vasculature using hollow gold nanospheres. *Biomaterials* **31**, 2617-2626 (2010).

189. Liu, G., Gao, J., Ai, H. & Chen, X. Applications and potential toxicity of magnetic iron oxide nanoparticles. *Small* **9**, 1533-1545 (2013).

190. Yarbrough, D.R., McAlhany, J.C., Cooper, N. & Weidner, M.G. Evaluation of the Heidelberg pH capsule: Method of tubeless gastric analysis. *The American Journal of Surgery* **117**, 185-192 (1969).

191. Carino, G.P. & Mathiowitz, E. Oral insulin delivery. *Advanced drug delivery reviews* **35**, 249-257 (1999).

192. Ma, Y. et al. The in vivo fate of nanoparticles and nanoparticle-loaded microcapsules after oral administration in mice: evaluation of their potential for colon-specific delivery. *European Journal of Pharmaceutics and Biopharmaceutics* **94**, 393-403 (2015).

193. Sarparanta, M.P. et al. The mucoadhesive and gastroretentive properties of hydrophobin-coated porous silicon nanoparticle oral drug delivery systems. *Biomaterials* **33**, 3353-3362 (2012).

194. Deuschl, G. et al. A randomized trial of deep-brain stimulation for Parkinson's disease. *New England Journal of Medicine* **355**, 896-908 (2006).

195. Limousin, P. et al. Electrical stimulation of the subthalamic nucleus in advanced Parkinson's disease. *New England Journal of Medicine* **339**, 1105-1111 (1998).

196. Illig, K.A. et al. An implantable carotid sinus stimulator for drug-resistant hypertension: surgical technique and short-term outcome from the multicenter phase II Rheos feasibility trial. *Journal of vascular surgery* **44**, 1213-1218. e1211 (2006).

197. Shiba, Y. et al. Human ES-cell-derived cardiomyocytes electrically couple and suppress arrhythmias in injured hearts. *Nature* **489**, 322-325 (2012).

198. Jagannathan, J. et al. High-intensity focused ultrasound surgery of the brain: part 1—a historical perspective with modern applications. *Neurosurgery* **64**, 201-211 (2009).